Design, Dynamics and Control of a Fast Two-Wheeled Quasiholonomic Robot

by

Alessio Salerno

Department of Mechanical Engineering
McGill University, Montreal

March 2006

A thesis submitted to McGill University
in partial fulfilment of the requirements of the degree of
Doctor of Philosophy

Your file Votre référence
ISBN: 978-0-494-27834-5
Our file Notre référence
ISBN: 978-0-494-27834-5

Abstract

The control of wheeled mobile robots is particularly challenging because of the presence of nonholonomic constraints. Modern two-wheeled mobile robot control is further complicated by the presence of one unstable equilibrium point, which requires a continuous stabilization of the intermediate body by means of sensors. In order to simplify the control of these systems, Quasimoro, a novel two-wheeled mobile robot, is proposed. The control of Quasimoro is simplified by means of its mechanical design. The robot is designed for quasiholonomy, a property that simplifies the control of nonoholonomic systems. To further simplify the control, the robot is designed so as to have a stable equilibrium point.

A nonholonomic robotic mechanical system that can be rendered quasiholonomic by control is termed, in this thesis, quasiholonomic. This is the case of Quasimoro.

This work proposes a model-based design methodology for wheeled mobile robots, intended to decrease the development costs, under which the prototype is built only when the system requirements are fully met. Following this methodology, the proposed robot is then designed and prototyped.

The conceptual design of the robot is undertaken by means of a detailed analysis of the most suitable drive systems and their layout. The mathematical model of the robot is formulated in the framework of the Lagrange formalism, by resorting to the concept of holonomy matrix, while the controllability analysis is conducted using modern tools from geometric control.

The embodiment design entails the simulation of three virtual prototypes aimed at further simplifying the robot control. To this end, a robot drive system, based on the use of a timing belt transmission and a bicycle wheel, is designed, calibrated and tested. Due to Quasimoro's drive system, the stabilization of the intermediate body, a well-known challenge in two-wheeled mobile robot control, is achieved without the use

of additional mechanical stabilizers—such as casters—or of sensors—such as gyros.

The intended application of the proposed robot is the augmentation of wheelchair users, a field that tremendously benefits from the cost-effectiveness and control simplification of the system at hand. For purposes of validation, a full-scale proof-of-concept prototype of the robot is realized. Moreover, the robot functionality is demonstrated by means of motion control experiments.

Résumé

La présence de contraintes non-holonomes complique la commande de robots mobiles à roues. De plus, la commande des robots modernes à deux roues est compliquée par la présence d'un point d'équilibre instable, ce qui exige la stabilisation du corps intermédiaire au moyen de capteurs. Dans le but de simplifier la commande de tels systèmes, Quasimoro, un robot à deux roues et muni d'une architecture mécanique nouvelle, est proposé. Son architecture particulière le rend quasiholonome, ce qui simplifie sa commande. Cette commande est d'autant plus simple puisque le robot est conçu de façon à posséder un état d'équilibre stable.

Le système mécanique non-holonome du robot, qui peut fonctionner comme système quasiholonome grâce aux algorithmes de commande, est appelé dans cette thèse quasi-holonome.

Cette thèse présente une méthodologie de conception de robots mobiles à roues qui s'appuie sur la modélisation. Celle-ci a pour but la réduction des coûts de développement. Le prototype de ce robot n'est realisé que lorsque le système est en pleine conformité avec le cahier des charges.

La conception de la morphologie a été entamée par une analyse détaillée des systèmes d'actionnement possibles et de leur réalisation. Le formalisme de Lagrange, s'appuyant sur la matrice d'holonomie, est utilisé pour modéliser le robot. De plus, une analyse de commandabilité se basant sur les outils modernes de commande géométrique est inclue.

Trois prototypes virtuels du robot ont été réalisés dans le but de simplifier au maximum la commande du robot. À cet effect, un système comprenant des courroies d'entraînement et des roues de bicyclette a été conçu, étalonné, puis testé. Grâce à ce dernier, la stabilisation du corps intermédiaire, problème courant dans le domaine de la commande des robots mobiles à deux roues, est accomplie sans stabilisateur

mécanique supplémentaire—tel que des roulettes—ni capteur—tel qu'un gyroscope.

Une des applications possibles du robot conçu est l'assistance aux usagers de fauteuils roulants, activité pour laquelle le rapport efficacité/prix et la commande simplifiée du système sont des avantages majeurs. À des fins de validation, un prototype du robot à l'échelle réelle a été réalisé et ses performances ont été testées.

Acknowledgements

First, I would like to express my deep gratitude and sincere thanks to my research supervisor, Professor Jorge Angeles, for his invaluable guidance, encouragement, and support. Without his continuous help and support this thesis could not have been completed. I am also indebted to him for the financial support he provided through the Research Grant A4532 of the Natural Sciences and Engineering Research Council of Canada (NSERC), which was instrumental when this work started. Moreover, I would like to thank Prof. Angeles for his scrupulous and critical reading of all the technical documents I have written during the course of my Ph.D. studies at McGill; this manuscript has been no exception. I have learned a lot from all his comments, remarks, and suggestions. I would also like to thank him for the financial support extended for the prototyping and experimental work through the FQRNT, *Le Fonds Québécois de la Recherche sur la Nature et les Technologies*, under Equipment Grant F11500-G204754, and the NSERC Design Engineering Chair "Design for Extreme Environments."

The financial support of the two-year Werner Graupe International Fellowship and of the two-year "Hydro-Quebec" McGill Major Fellowship is also gratefully acknowledged.

The translation of the thesis abstract into French was done by Dr. Stéphane Caro and Philippe Cardou. I would like to thank Stéphane and Philippe for their great help.

Further, I wish to express my wholehearted thanks to all the colleagues I met at McGill—particularly, Drs. Greg Aloupis, Khalid Al-Widyan, Stéphane Caro, Chao Chen, Dany Dionne, Sunil L. Kukreja, Alexei Morozov, Svetlana Ostrovskaya, Ioannis Rekleitis, Shahid Mohammed Shaikh, Miguel Torres-Torriti, besides Shawn Arseneau, Gianni Campion, Philippe Cardou, Melita Hadzagic, Waseem Ahmad Khan, Casey Marcel Lambert, Flavia Majlis, Danielle Nasrallah, Ioannis Poulakakis, Christopher Prahacs, Georgios Rekleitis, James Andrew Smith, Luiza Solomon and Perouz Taslakian—for all the wonderful discussions and the great time we have had over the years.

I am also pleased to acknowledge the help and support of Irène Cartier, of the Department of Mechanical Engineering, as well as that of the Centre for Intelligent Machines (CIM) staff: Jan Binder, Daniel Chouinard, Cynthia Davidson, and Marlene Gray.

I would also like to express my gratitude to *a*) Hugo Levasseur, of Concordia University; *b*) Rafael Perlin, of Ardi Consultants Enr.; *c*) Nicola De Palma, Antonio Micozzi and Roy Westgate, of the Machine Tool Laboratory of the Department of Mechanical Engineering; *d*) Mario Iacobaccio and Georges Tewfik, of the Instrument Laboratory of the Department of Mechanical Engineering; *e*) General Metal Works (GMW) Ltd., Lachine, QC; and *f*) Bob Thomson, of the Electronics Workshop of the Department of Electrical and Computer Engineering.

My parents and my brother also deserve my most sincere thanks for their encouragement and their unwavering belief in me.

Finally, I would like to express my deepest gratitude to my wife Laura, to whom I dedicate this thesis, for her great patience, support, and all the sacrifices she has made.

Claim of Originality

The ideas expressed in this thesis, to the best of the author's knowledge, are original[1]. The contributions of this thesis are listed below:

- A proof that the quasiholonomy property simplifies the computed-torque control of nonholonomic systems.
- A proof on the local accessibility and small-time local controllability properties of two-wheeled quasiholonomic mobile robots.
- The design, calibration and testing of a novel drive system, capable of stabilizing the intermediate body of two-wheeled mobile robots, without the use of additional mechanical stabilizers, e.g. casters, or sensors, e.g. gyros.
- The design, implementation and experimental testing of the prototype of a quasiholonomic robotic system.
- A novel cost-effective and simple-to-control robot for wheelchair user augmentation.
- The demonstration of robot functionality by means of open-loop control experiments.

[1]Some of the results reported in this thesis have been partly published in (Salerno et al., 2002; Salerno and Angeles, 2003a;b; 2004b; Salerno et al., 2004a; Salerno and Angeles, 2004a; Salerno et al., 2004b).

List of Abbreviations

2-WMR	Two-Wheeled Mobile Robot
AD	Analog-to-Digital
ADD	Automatic Drink Distributor
AP	Assistant-Propelled
EP	Electrically-Propelled
CPU	Central Processing Unit
CTC	Computed-Torque Control
DA	Digital-to-Analog
DIO	Digital Input/Output
dof	Degrees of Freedom
ESCWA	Economic and Social Commission for Western Asia
FAO	Food and Agriculture Organization
IB	Intermediate Body
IFC	Inductive Filter Card
KRCC	Kalman Rank Condition for Controllability
LA	Locally Accessible
LARC	Lie-Algebra Rank Condition
MC	Mass Centre
NH	Nonholonomic
PA	Power Amplifier
PC	Personal Computer
PG	Planetary Gearhead
PH	Payload Holder
PL	Partial Linearization
PWM	Pulse-Width Modulation
QH	Quasiholonomic
RB	Regenerative Braking
RDS	Robot Drive System
RHA	Robotics for Human Augmentation
RHL	Robot Home Location
RVP	Robot Virtual Prototype
STLC	Small-Time Locally Controllable
TS	Transmission System
WHO	World Health Organization
WMR	Wheeled Mobile Robot
WU	Wheelchair User

Contents

Quelli che si innamorano della pratica senza la scienza sono come il nocchiero che monta sulla nave senza il timone o la bussola, e non ha mai certezza su dove si vada.

—Leonardo da Vinci (1452–1519)[2]

[2] *Those who love practice without theory are like the sailor who boards a ship without rudder and compass, and never knows where he may go*—Translation of the author.

Chapter 1

Introduction

1.1 Motivation

The motivation behind this thesis is manifold, and stemming from the need to: *i*) design, implement and experimentally test a quasiholonomic (QH) robot; *ii*) develop and put in practice a model-based design methodology for wheeled mobile robots (WMRs); *iii*) contribute to the field of robotics for wheelchair-user augmentation; *iv*) investigate the feasibility of two-wheeled mobile robots (2-WMRs); *v*) demonstrate that quasiholonomy eases the control of nonholonomic (NH) systems; and *vi*) develop a novel robotic platform for testing motion control strategies for QH systems.

Another motivation of this work stems from the field of educational robotics, where detailed guidelines on how to design and implement WMRs are still lacking.

1.2 Mobile Robotics for Wheelchair User Augmentation

The World Health Organization (WHO) (1976) defines *impairment* as "any loss or abnormality of psychological, or anatomical structure or function"; *disability* as "any restriction or lack (resulting from an impairment) of ability to perform an activity in the manner within the range considered normal for a human being."

Moreover, 600-million subjects are affected by an impairment or a disability, with 80% living in developing countries (FAO, 2001).

The United Nations' FAO estimates that about 10% of the population in various countries may be considered disabled. However, there is a great variation in the incidence of disabilities in the statistics from different countries. These differences may be caused by different criteria for reporting, degrees of industrialization, rate of traffic accidents and participations in wars, for example (Kuang et al., 1997).

More specifically, in Canada and the United States (US) there are 53.1-million disabled persons: *i*) an estimated 19.4% percent of nonistitutionalized US civilians, totalling 48.9 million people, have a disability (Kraus et al., 1996); and *ii*) in 1991 there were an estimated 4.2-million Canadians with disabilities, representing 16% of the total population (Canadian Centre for Justice, 2001).

With reference to people affected by leg disabilities we have the following conditions: *i*) disability may exist at birth (e.g. cerebral palsy and dwarfism); *ii*) disability may be caused by a disease (e.g. arthritis, diabetes, multiple sclerosis, muscular dystrophy, and polio); and *iii*) disability may be the result of trauma or accident (e.g. spinal cord injury, amputation, and stroke).

The *assistive technology device*[1] that people with a severe leg disability use the most is the wheelchair. For example, *i*) in 1991 in Canada there were 124.000 wheelchair users (WUs), a number that has been predicted to grow by 62% by 2015 (Statistics Canada, 1991); and *ii*) according to a recent survey, in the US there are 1.4-million WUs (Kraus et al., 1996).

Robotics for human augmentation (RHA) provides considerable opportunities to improve the quality of life for the physically disabled. This branch of robotics integrates humans and robots in the same task, requiring certain safety aspects and special attention to human-machine interfaces. *Therefore, more attention must be paid to the user requirements, as the user is a part of the process in the execution of various tasks* (Bolmsjö et al., 1995). Various types of robots for human augmenta-

[1]According to Cook and Hussey a widely used definition of "assistive technology device" is provided by the U.S. Congress (1988): "any item, piece of equipment, or product system whether acquired off the shelf, modified or customized, that is used to increase, maintain, or improve functional capabilities of individuals with disabilities."

tion have been built so far (Hoppenot and Cole, 2001): *i*) workstation-based systems, i.e. a table-mounted robot arm which works in an environment where the positions of different objects are known by the system; *ii*) stand-alone manipulator systems, in which the object position is not known; *iii*) wheelchair-mounted manipulators; and *iv*) mobile robots such as: WALKY (Neveryd and Bolmsjö, 1995), Health Care Robot (Fiorini et al., 1997), URMAD (Guglielmelli et al., 1994), MOVAID (Giuffrida et al., 1998), and ARPH (Hoppenot et al., 2001).

1.3 Wheeled Mobile Robots

Mobile robots can freely navigate and manoeuvre in virtually any environment. The most popular mobile robots are of the wheeled or rolling type (Fisette et al., 2000; Dudek and Jenkin, 2000; Paquin and Cohen, 2004; Pathak et al., 2005). WMRs are well suited for operation on relatively smooth, flat, rigid floors; WMRs are widely used, for they are known to provide smooth motion.

1.3.1 Control Challenges

The real-time control of WMRs entails many theoretical and practical problems (Campion et al., 1996; Oriolo et al., 1998), which make motion-planning and control algorithms, developed for robot manipulators, inapplicable (Campion et al., 1996). This is due to the presence of NH, i.e. non-integrable, kinematic constraints which characterize WMRs. This means that, despite being able to reach an arbitrary position and orientation on the plane of rolling, WMRs with conventional wheels cannot move under arbitrary angular and translational velocities simultaneously.

Applications imposing high speeds, high loads, or even both, require the use of the dynamics model in the control of WMRs (Shekkar, 1997; Hong et al., 1999). However, the high computational complexity of control strategies based on the dynamics model, such as computed-torque control (CTC)(Paul, 1972; Markiewicz, 1973), is usually an issue in the real-time control of robots (Hollerbach and Sahar, 1984; Leahy et al., 1986; Khosla, 1987). The CTC of WMRs is further complicated by the presence of NH constraints.

1.3.2 Design Challenges

Nonholonomy affects also WMR design. As a matter of fact, WMRs with standard conventional wheels are not omnidirectional, i.e. they cannot move under arbitrary angular and translational velocities simultaneously. As a means of coping with this problem, some ingenious wheels for mobile robots have been developed, e.g., offset steered driving wheels, omnidirectional wheels, and spherical wheels. However, even omnidirectional WMRs feature kinematic constraints that are, in general, NH and therefore, no reduction in their configuration space is possible (Salerno et al., 2002).

1.3.3 Quasiholonomy

A new class of robots, namely QH WMRs, was first reported in 1998 in a review paper of NH mechanical systems (Ostrovskaya and Angeles, 1998). QH WMRs are NH mechanical systems that are so dubbed because their mathematical models bear striking similarities with those of their holonomic counterparts. These robots are governed by simple mathematical models that resemble holonomic systems, and hence, QH WMRs can be regarded as lying halfway between holonomic and nonholonomic mechanical systems (Ostrovskaya and Angeles, 1998).

In this thesis, a nonholonomic robotic mechanical system is termed *quasiholonomic* if and only if the system can be rendered quasiholonomic by control. We show in Chapter 4 that Quasimoro can indeed be rendered quasiholonomic by feedback control.

1.3.4 Design Methodology

During the last thirty years, the design of robotic mechanical systems has been a field of intensive study. Several aspects on the design of serial and parallel manipulators are now well documented in the literature (Asada, 1982; Yang and Lee, 1982; Hollerbach, 1985; Holzbock, 1986; Roth, 1986; Takano et al., 1986; Yoshikawa, 1986; Jacobsen et al., 1988; Jeong et al., 1990; McAree et al., 1991; Gosselin and Angeles, 1991; Angeles et al., 1992; Angeles, 1992; Gosselin, 1992; Ma and Angeles, 1993; Daniali et al., 1994; Ou and Tsai, 1996; Rico Martinéz and Duffy, 1998; Ottaviano and Ceccarelli, 2002; Suthakorn and Chirikjian, 2000; Yang et al., 2001; Dunlop, 2003). In this regard, some monographs on serial manipulator design are available (Critchlow, 1985; Asada and Youcef-Toumi, 1987; Rivin, 1988; Hill, 1997). However, WMR design has not been addressed in sufficient detail in the specialized literature. More specifically, WMR design still relies heavily on intuition and experience following a traditional paradigm (building prototypes until the system requirements are met), only few systematic treatments of WMR design being available (Clement and Villedieu, 1987; Briand et al., 1987; Hagihara et al., 1987; Keafter, 1988; Martin et al., 1987; Silverman et al., 1987; Saha et al., 1993; 1988; Hada and Yuta, 2000; Hirata et al., 2000; Bischoff and Graefe, 2003; Kawakami et al., 2003; Iagnemma et al., 2003; Goris, 2005; Ray et al., 2005).

WMR design is not yet a mature technology; instead, it is still a completely experiential art. No authoritative work on WMR design has been published yet, and such a work is long overdue.

1.4 Two-Wheeled Mobile Robots

During the last decade, at the research, industrial and hobby levels, the effort in developing 2-WMRs, has increased dramatically, mainly for their *mechanical simplicity.* 2-WMRs are characterized by two driving wheels connected to an intermediate[2] body (IB) carrying actuation, transmission, control, and communication sub-systems.

2-WMRs can be divided in three classes, namely

i) robots without any stabilization of the IB;

ii) robots with mechanical stabilization of the IB;

[2]The word "intermediate" refers to the fact of being at the middle place between the wheels.

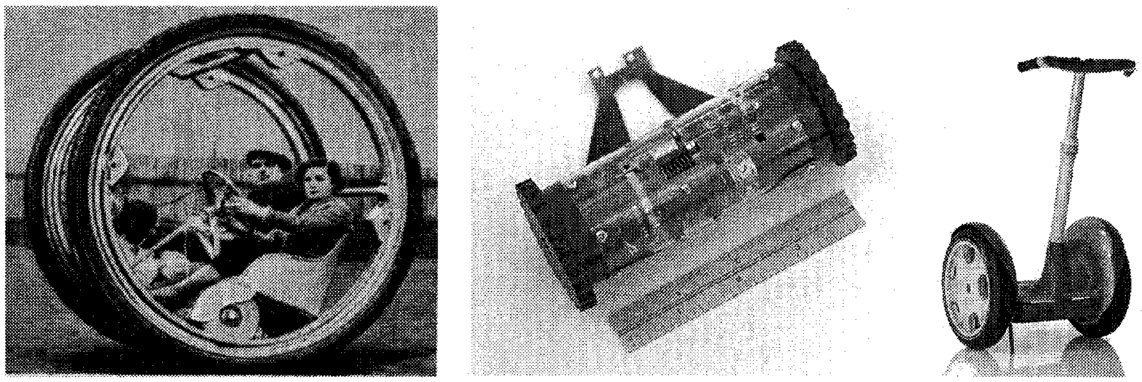

(i) (ii) (iii)

Figure 1.1: Gyrauto, Scout and Segway

iii) robots with electronic stabilization of the IB.

The oldest ancestor of modern 2-WMRs, Gyrauto, belongs to the first class. This is a vehicle designed in 1935, which carried the driver between a pair of large, side-by-side wheels (Fraquelli, 1935), see Fig. 1.1i. Examples of robots belonging to the first class can be found in the following references: (Batavia and Nourbakhsh, 2000; O'Halloran et al., 2004). Having only two points touching the ground, the IB of these robots has the tendency to tip back and forth[3]. To cope with this problem, robot designers have adopted several mechanical solutions which stabilize the IB by using: *a*) a long handle attached to the robot maneuvered by the user herself (Borenstein and Ulrich, 1997); *b*) a caster wheel (ActivMedia Robotics, LLC, 2001; Applied AI Systems, Inc., 2000; iRobot™ Corp., 2002; Robosoft, 2002); and *c*) a sliding supporting point (Drenner et al., 2002; Mächler, 1998; Tsukagoshi et al., 2005), see Fig. 1.1ii. However, there are several important factors to consider when designing a robot of class *ii*). First, the robot weight should be balanced over the supporting points, i.e., driving wheels plus mechanical stabilizer, from front to back; a robot mass centre (MC) too close to the driving wheels eases the tip-over of the IB, while a robot MC too close to the mechanical stabilizer increases traction losses. Second, these robots work fine on a flat surface, but when going up and down inclined surfaces they do not behave as

[3] `http://dc.cen.uiuc.edu/`

well. When going uphill, robot weight shifts back over the stabilizer, thereby causing the driving wheels to lose traction, which leads to slippage; as the slope increases, eventually the robot stops its forward motion altogether and its wheels start turning around a fixed point. Going downhill is perhaps even worse, as the MC of the robot shifts forward and eventually causes the WMR to tip up on its "nose" as the slope increases, see Fig. 1.2.

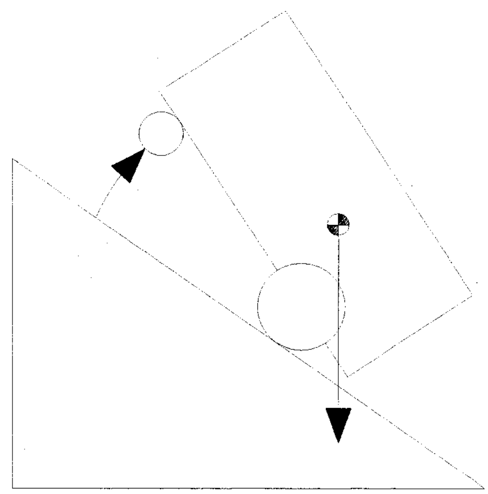

Figure 1.2: Class *ii*) WMR going down hill

To avoid the problems encountered with class *ii*), a few robot designers have developed 2-WMRs with electronic stabilization of the IB. With reference to the latter, the following sensor sub-systems have been used to stabilize the IB: *a*) a rate gyro (Grasser et al., 2002); *b*) five gyros and two tilt-sensors (Segway Inc., 2006), see Fig. 1.1iii; and *c*) a rate gyro and two orthogonal accelerometers[4]. However, the open-loop dynamics of the foregoing robots is unstable at the equilibrium point, which often results in damage to the hardware or leads the system into limit cycles (Slotine and Li, 1991), thereby complicating the robot control.

[4] `http://www.geology.smu.edu/~dpa-www/robo/nbot/index.html`

1.5 Thesis Outline

This thesis hinges on a topic of paramount importance: the design of WMRs. A novel design methodology based on the mathematical model of these systems is proposed. This methodology is exemplified with the design, implementation and experimental tests of Quasimoro (QUASIholonomic MObile RObot), a novel robot for wheelchair-user augmentation. Quasimoro consists of two wheels and an IB carrying the payload, power source, actuators and control hardware.

As mentioned in Section 1.2, various robot prototypes for human augmentation have been reported so far. Even so, in RHA many designs have failed. This can be attributed to some basic limitations, namely, *cost factors* and *control difficulties* (Kuang et al., 1997). As a matter of fact, robots for human augmentation are not even mentioned in the recent statistics concerning the use of assistive technology devices (Kraus et al., 1996). In this thesis we introduce Quasimoro, an *easy-to-control* and *cost-effective* robot for wheelchair-user augmentation.

As we have anticipated in Subsection 1.3.3 quasiholonomy, a novel property that simplifies the mathematical model of WMRs, has been first reported in 1998. While the theoretical framework behind QH WMRs has been laid out (Ostrovskaya, 2001), research on the design and control of QH robotic systems is yet to be reported. To this end Quasimoro, a QH robot, is designed, prototyped and experimentally tested.

As outlined in Section 1.3, even omnidirectional WMRs have kinematic constraints that are, in general, NH, i.e., not integrable and therefore, no reduction in their configuration space is possible. Nevertheless, omnidirectional WMRs can be rendered quasiholonomic as shown in Subsection 3.1.2.

As pointed out in Subsection 1.3.1, the CTC of WMRs is complicated by the high computational complexity. In this regard, in Subsection 3.1.1 we prove that quasiholonomy simplifies the CTC of NH systems.

As mentioned in Section 1.4, the control of 2-WMRs is complicated by their unstable equilibrium point and the need for IB stabilization. Therefore, in order to simplify the control of 2-WMRs a novel robot, Quasimoro, with its MC below the wheel axis, is proposed here. With the same purpose, Quasimoro belongs to a new class of robots that are endowed with the quasiholonomy property (Ostrovskaya and Angeles, 1998), which is achieved by simply placing the MC of the robot on the vertical passing through the midpoint of the segment defined by the wheel centres.

1.6 Model-Based Design Methodology for Wheeled Mobile Robots

As anticipated in Susbsection 1.3.4, in reading the WMR scholarly literature, one usually finds some aspects of robot design. More specifically, most of the times a prototype appears suddenly as a conclusion of the manuscript (This applies mostly to works whose main focus is on kinematics, dynamics, control or programming of robots.) Some works on WMR design can be found in the literature—see Subsection 1.3.4—but these works usually give a description of the prototype or the testbed without providing the reader with a clear and detailed design methodology on how to go from concept to full-scale prototype. Filling the gap between theory and practice contributes to both research and education in robotics. Research benefits in terms of development cost and time to completion. Education benefits as well: students can relate to a real robot much better than to a piece of software; a working robot program will be much more than just a logic solution coded in software (Bräul, 2003).

A summary of the model-based design methodology proposed here is given in Fig. 1.3. This methodology strongly reduces the development costs by reducing the amount of physical prototypes needed to meet the system requirements.

The sub-processes of this methodology are reported in the balance of the section.

1.6.1 Conceptual Design

This key stage of the design process involves many issues, in the realm of WMRs, namely,

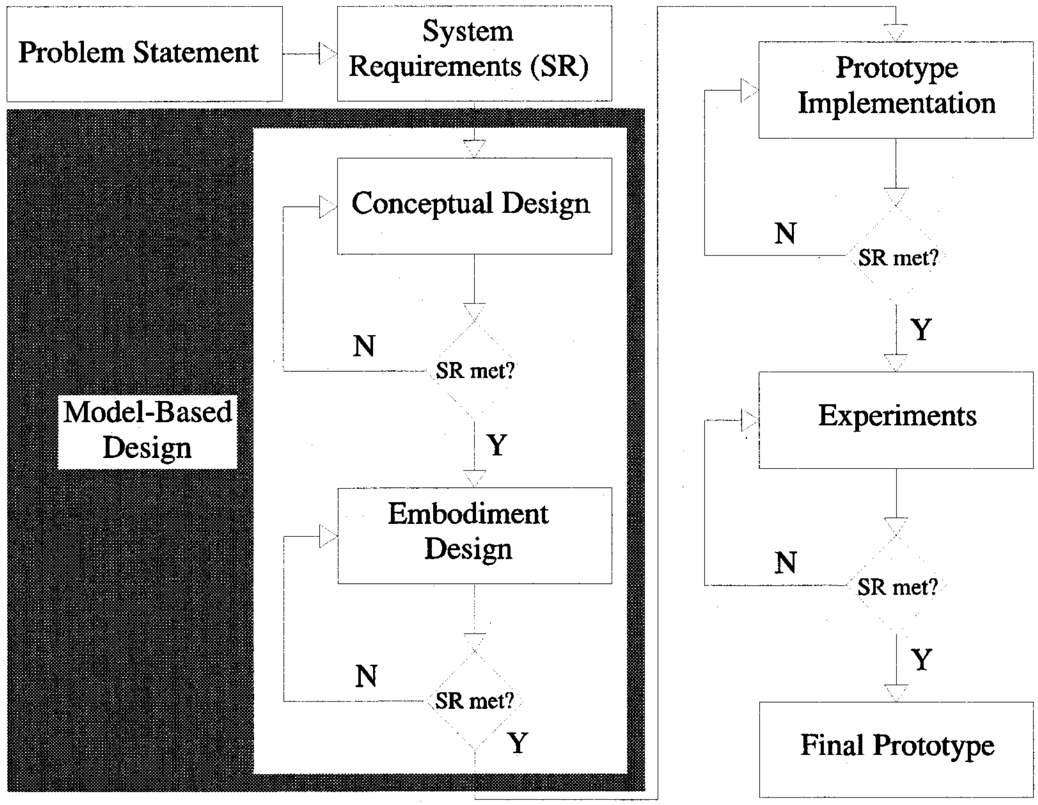

Figure 1.3: Model-based methodology for WMR design

- Locomotion system selection (number of driving wheels, caster wheels, etc.).
- Power supply, motor, transmission system (TS), power amplifier (PA), sensor, control unit, data-acquisition sub-system, communication sub-system and robot user control unit type selection.
- General layout of robot components.
- Mathematical modelling.
- Kinematic and dynamics analyses.
- Controllability analysis.
- Robust design aspects.
- Control aspects (feedback vs. open-loop, linear/nonlinear, etc.).

- Robot dynamics preliminary results.

1.6.2 Embodiment Design

This stage involves four activities:

- Dimensioning of power supply, motor, TS, PA, sensor, control unit, data acquisition sub-system, communication sub-system and robot user control unit.
- Power switch design.
- Robot chassis and drive system design.
- Custom-made component design.

1.6.3 Detail Design

In the realm of WMR design, this stage relies on the mathematical model of the system and of the individual sub-systems:

- Analysis of robot drive system dynamics.
- Regenerative-braking (RB) analysis.
- Final analysis of robot dynamics prior to manufacturing.

1.6.4 Prototype Implementation

The activities of this stage include:

- Providing for protection against short-circuit.
- PA calibration.
- Providing for wiring and cabling.
- Selection of robot electrical grounding system.
- Robot drive system calibration.

- Robot programming.
- Robot assembly.

1.6.5 Experiments

Once the prototype is complete, a series of tests follow:

- Power test.
- Test-bench experiments.
- Wireless communication.
- Motion control experiments (down-hill motion, no-load/full-load motion, obstacle-avoidance test).
- Primitive of motion experiments (rectilinear motion, rotation in place, etc.).

Chapter 2

Conceptual Design

Two areas contributing to the development of assistive technology devices can be cited: *i*) smart home technology, also known as domotics[1]; and *ii*) robotics for human augmentation (RHA). We believe that the synergy stemming from the foregoing areas will contribute to effectively help the disabled in conducting tasks related to intellectual, daily living and spare-time activities.

2.1 Problem Statement

As stated in Chapter 1, when designing a robot for human augmentation, as in service robotics, particular attention must be paid to the user and her/his requirements. However, a robot for human augmentation, different from a home-based service robot for *general-purpose use*, is designed as a solution to *specific problems*. The tasks of RHA are defined by the impairments of the disabled user.

For a wheelchair user (WU) capable of moving the upper limbs, it is: *i*) difficult to manoeuvre a wheelchair while balancing plates of food; and *ii*) extremely annoying to move around every time that she/he needs an item, e.g. a flask of medication or a book. Therefore, a mobile robot should be designed and manufactured for the foregoing WU, who no longer would have to struggle to accomplish a task by moving

[1]The term originated in France, where the first "domotique" results were reported. Domotique, or domotics in English, is a contraction from the Latin word "domus"(= house) and informatics (Girardin, 1994).

User	wheelchair user
Environment	especially designed living quarters
Payload	books, medication, food & drinks

Table 2.1: General design specs

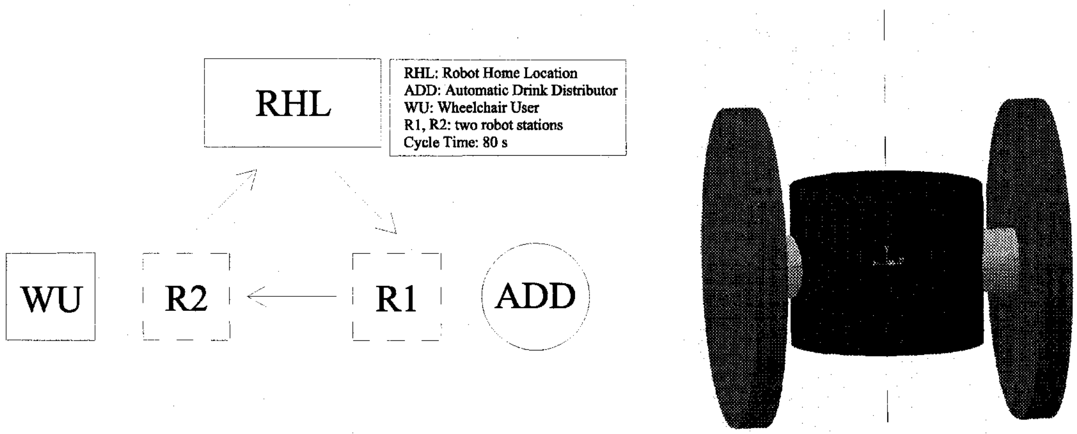

(a) (b)

Figure 2.1: (a) Strawman task (b) Catia^{TM}-generated concept

around. She/he can simply have a robot carry out her/his tasks by either pushing a button or giving oral commands. Also, a mobile robot would rebuild confidence and self-esteem lost in the depths of the illness (Kuang et al., 1997). The design specifications arising from the foregoing reasoning are synthesized in Table 2.1.

2.1.1 Strawman Task

In order to define the design guidelines of a robotic mechanical system, a clear picture of its application is needed. Therefore, a strawman task is formulated as outlined in Fig. 2.1a. More specifically, the task is accomplished by means of three operations: *i*) the robot moves from the home location to the automatic drink distributor (ADD) where the robot collects a drink; *ii*) then, the robot moves to location R2 and delivers the drink to the WU; and *iii*) the robot returns to its home location, thus completing the task. In order to compute the cycle time we assume that the robot moves in a room of standard dimensions (Environment Department, 2001). Quite importantly, we assume that the living quarters are provided with ramps for smooth negotiation of

Wheelchair Type	**Height** [m]	**Depth** [m]	**Width** [m]
Self-propelled	0.845–1.045	0.840–1.170	0.500–0.640
AP/EP	0.930–1.090	0.840–1.445	0.520–0.650

Table 2.2: Wheelchair overall dimensions (Salerno and Angeles, 2003b)

different levels, as needed by wheelchairs, and as mandated by legislation. This brings about the following functional requirement: the robot should be able to negotiate ramps with the most pronounced slopes.

User Definition

The end-user is a paraplegic WU. Moreover, the robot dimensioning has to guarantee a comfortable access of the user to the payload. To do this, the robot has to comply with different types and dimensions of wheelchairs. In order not to restrict the robot application we consider the underlined values of Table 2.2, which includes every wheelchair type, namely, self-propelled, assistant-propelled (AP), and electrically-propelled (EP).

The architecture and the dimensions of a wheelchair affect the user reachability zone. From the analysis of the reaching zones of a paraplegic WU we can obtain specifications on the height H of the robot. More specifically, for a comfortable forward access to the payload, we have $0.90\,\mathrm{m} \leq H \leq 1.20\,\mathrm{m}$, while for a comfortable side access to the payload, we need $0.45\,\mathrm{m} \leq H \leq 1.90\,\mathrm{m}$. However, to guarantee a comfortable side access and not to frighten the user with a bulky device, the robot should be as high as an armchair, i.e. (ESCWA, 2003)

$$H \in [0.58,\ 0.69] \quad [\mathrm{m}]. \tag{2.1}$$

Environment Definition

The robot operates in an environment respecting the paraplegic WU standard housing where (Environment Department, 2001): *a*) ramps with a slope greater than 5% and steps are avoided by resorting to level thresholds achieved by the use of gentle slopes and smooth landscaping; and *b*) corridors and passageways respect specific

Item	Weight [N]
books, magazines, newspaper etc.	20
food and drinks	30
miscellaneous (medications, eye-glasses, telephone, etc.)	20
nominal maximum payload weight	70

Table 2.3: Computation of the maximum payload weight

proportions. Moreover, the environment is characterized by *i*) non-slip surfaces; and *ii*) platform lifts (intended to give WUs access to mezzanine levels, raised or lowered floor areas) used for moving between floors or up half floors.

Payload Specifications

The payload is located on a food tray of overall dimensions, $0.385\,\mathrm{m} \times 0.310\,\mathrm{m} \times 0.020\,\mathrm{m}$, with uniform thickness of 0.005 [m] and weighing 5 N. The nominal maximum payload weight is of 70 N, as recorded in Table 2.3. The maximum payload described in Table 2.3 is equivalent to a 70 N parallelepiped of homogeneous material having dimensions of $0.375\,\mathrm{m} \times 0.300\,\mathrm{m} \times 0.220\,\mathrm{m}$.

2.2 Locomotion System Selection

In the realm of RHA, many designs have failed. This can be attributed to some basic limitations, namely, cost factors and control difficulties (Kuang et al., 1997). Therefore, the robot at hand has to meet additional requirements to the dimensional and functional specifications stemming from the strawman task of Section 2.1.1. That is, the system should be: *i*) cost-effective; and *ii*) easy to control.

A two-driving wheel architecture is selected for its mechanical simplicity[2]. Wheels are generally most useful in terrain where obstacles are not taller than 40% of the wheel height. Wheeled robots are capable of much higher speeds than legged and tracked robotic systems, and are thus used indoors.

[2]An even simpler system is a mono-wheeled robot. However, this architecture is disregarded because of its unstable equilibrium point.

In this light, Quasimoro, the robot proposed in this thesis, comprises three main bodies: two wheels and the IB carrying the payload, as indicated in Fig. 2.1b. This architecture makes Quasimoro capable of turning in place without colliding with a person or an object nearby.

2.3 Design Challenges and Robot Main Tasks

Due to Quasimoro's unique architecture the choice and the location of the components, such as motors, speed reducers, and control unit is not straightforward. In fact, the challenge lies in designing the robot in such a way that it is possible to stabilize the payload, which tends to rotate about the wheel axle, as the wheels are actuated.

The robot is designed so as to: *i*) dampen the oscillations of the IB without the use of an additional mechanical device that comes in contact with the ground, or of an electronic stabilization system; *ii*) have a stable equilibrium point; *iii*) ensure static and dynamic stability under payload variations; and *iv*) be underactuated.

Quasimoro's main tasks are: *i*) positioning and orienting the payload, supported by the IB, on a flat surface (primary task); and *ii*) suppressing the oscillations of the IB (secondary task.)

2.4 Choice of Actuator Power Supply

The results of Section 3.3[3] show that only two actuators, one per wheel, are needed to control Quasimoro.

Once the number of actuators needed is established, their respective types need to be determined. The types of actuators currently used in robotics can be classified according to their power supply as follows: *i*) pneumatic; *ii*) hydraulic; and *iii*) electric.

Weight and dimensions are crucial factors in WMR design. Hence, Quasimoro

[3] If the results of the controllability analysis had been disappointing, we would have had to resort to another design concept (different wheel layout and/or different number of actuators, for example).

is actuated by electric motors. These motors do not require a power station like a storage tank, in the case of the pneumatic actuators, or a reservoir, in the case of hydraulic actuators. Besides, electric motors have the following advantages (Sciavicco and Siciliano, 2000): *i*) high power conversion efficiency; *ii*) low maintenance; *iii*) low cost; *iv*) low noise level; *v*) better control flexibility; *vi*) immediate start-up; *vii*) independence of basic characteristic from temperature; and *viii*) no pollution on working environment.

In this light, the power source of Quasimoro actuators is a battery. The latter allows also for wireless communication.

2.5 Motor Selection

The types of electric motors commercially available are: *i*) AC induction motors; *ii*) synchronous reluctance-type AC motors; *iii*) stepper motors; *iv*) brushless DC motors; and *v*) commutator-type DC motors. It is noteworthy that DC motors are extensively used in control systems as positioning devices because their speed as well as their torque can be precisely controlled over a wide range (Guru and Hiziroglu, 2001). Moreover, a DC motor is, of course, a logical choice when a DC power source is available, as is the case of Quasimoro. Therefore, AC motors are disregarded.

Quasimoro motors have to be suitable for both open-loop and closed-loop applications. To this end, stepper motors are discarded because they are designed to be used for open-loop applications.

2.5.1 DC Motors

The major drawback of the commutator-type DC motors is brush failures. These devices wear, causing the terminal resistance of the armature to increase significantly, thereby reducing efficiency and maximum torque. This effect contributes to increased heating as well (Klafter et al., 1989). A remedy to the above-mentioned problem is the DC brushless motor.

The DC brushless motor is a three-phase synchronous AC machine with a permanent-magnet rotor whose speed is proportional to the input frequency. The latter, can be, in turn, proportional to a DC input voltage, and with this DC voltage as input, the control characteristics of the motor are similar to a DC motor without brushes, hence the name (Parkin, 1991).

The performance of brushless motors is the same of commutator-type DC motors. However, the former are more expensive because their control devices are more complicated, owing to the motor simple structure (Dote and Kinoshita, 1990). Moreover, with proper motor design, sizing, and control, the maintenance of DC commutator-type motors does not exceed a minimum corresponding to that of the other maintenance procedures (Holzbock, 1986). Furthermore, regenerative braking is more expensive when using brushless motors because of the electronic commutation.

In view of these last considerations, we use DC commutator-type motors for the actuation of Quasimoro.

Permanent-Magnet Motors

There are two types of DC commutator motors: the wound field and the permanent-magnet motors. In our design, the permanent-magnet motor is selected for the following reasons (Gieras and Wing, 1997): *i*) no electrical energy is absorbed by the field excitation system, and thus, there are no excitation losses, which means a substantial increase in the efficiency; *ii*) higher torque per volume than when using electromagnetic excitation; *iii*) the torque-speed characteristics is closer to linear; *iv*) for a given output power, the permanent-magnet motor can be made smaller and lighter than the equivalent wound-field motor; *v*) better dynamic performance than motors with electromagnetic excitation (higher magnetic flux density in the airgap); and *vi*) low maintenance.

Moreover, the extraordinary progress in the ceramic, ferrite and alloy materials is reflected in a moderate cost of modern permanent-magnet motors.

2.6 Power Amplifier

The PA of each of the two DC commutator-type permanent-magnet motors of Quasimoro is a four-quadrant chopper controller. This choice allows to control each motor in the two directions of rotation and to benefit from the regenerative braking. Further, an analog amplifier is preferred to a digital one because of its lower cost and better performance (analog amplifiers can offer better current loop performance than digital amplifiers from a bandwidth and resolution standpoint). Although a brushless-type amplifier can also be used for the Quasimoro motors, brush-type amplifiers are preferred because they are more cost-effective.

2.7 Transmission System

2.7.1 Direct-Drive Systems

Before analyzing the TSs used in robotics, a question should be addressed: is the speed reducer really needed?

Electric motors with their high speed and low torque require a speed reducer, which degrades the actuator performance, introducing backlash, stiction, friction and compliance. All foregoing drawbacks are avoided or reduced in direct-drive motors[4] (Aghili, 1997), which have been implemented by Asada and Youcef-Toumi (1987) using: *i*) DC torque motors; *ii*) brushless DC torque motors; and *iii*) variable-reluctance motors.

However, direct-drive motors have the following drawbacks: *i*) higher sensitivity, as compared to geared motors[5], to both the actuator's torque ripple and to the robot dynamics (Aghili, 1997); *ii*) overheating under continuous-load condition; *iii*) need for a controller designed for the compensation of the nonlinear robot and actuator dynamics; and *iv*) low continuous torque compared to geared motors (Aghili, 1997).

[4]Direct-drive motors are electric motors that feature high torque and low speed without having to use a speed reducer.

[5]A geared motor is a system that consists of an electric motor and a speed reducer.

More specifically, the major drawback of direct-drive motors derives from the complications that have to be introduced in the control system design. The controller for direct-drive motors has to compensate the nonlinearities deriving from the robot and actuator dynamics, not anymore filtered by the speed reducer. Further a direct-drive motor has almost zero damping, and hence, in order to stabilize the system response, we need to increase the damping in the control system design. A higher controller gain will be needed to compensate the deficit of the loop gain, due to the absence of the speed reducer. Finally a stabilization of the motor inductance effect will have to be accounted for, since the electric time constant is not negligible.

A typical electric motor speed is generally greater than the wheel speed of the robot. Hence, a speed reducer needs to be used. Additionally, a speed reducer is also chosen because it simplifies the robot control.

2.7.2 Speed Reducers

Electric motors offer low torque and high speed. However, the motion of the wheels and the IB requires high torque and low speed. Rare-earth magnets in DC motors are a significant improvement, since they offer higher torque and lower speed, but reducers are still needed in applications such as Quasimoro.

The principal requirements for TSs of robots are (Rivin, 1988): *i*) small size; *ii*) low weight and moment of inertia; *iii*) low backlash[6]; *iv*) high stiffness; *v*) accurate and constant transmission ratio; and *vi*) low energy losses and friction for a better response of the control system.

The speed reducers commonly used in robotics are: *i*) simple gear trains; *ii*) planetary gear trains; *iii*) harmonic drives ; and *iv*) planetary cycloidal drives.

[6]Backlash is defined as the clearance between mating teeth measured along the circumference of the pitch circle.

Simple Gear Trains

Simple gear trains usually feature high backlash. Backlash is needed for assembly, and takes place whenever the torque changes sign; under this condition the backlash gap is traversed and the teeth collide with noticeable noise. Backlash increases stresses and wear, and is responsible for undesirable positional errors in the control of the robot (Rivin, 1988). In addition to inducing wear in the mechanical elements of the actuation system, backlash plays an important role in the dynamic response of gear trains. The output response of the driven gear can assume one of two possible values, depending on the time history of the drive gear.

Spur gears are usually employed in the design of simple gear trains in order to reduce the requirements for bearings and housings because of the elimination of axial forces (Rivin, 1988). Moreover, in order to have interchangeable gears the involute profile is often selected (Dudley, 1962). However, involute gears feature relatively large size necessary for the realization of large transmission ratios (Rivin, 1988). To accommodate large transmission ratios we have to decrease the minimum allowable teeth number of the pinion, which is done by introducing design modifications and/or by using a different kind of gear (Rivin, 1988). However, the dimensions of a simple gear train with involute tooth profile will never be as small as those of a planetary gear train having the same transmission ratio. For this reason, Quasimoro TS design does not consider the use of simple gear trains.

Planetary Gear Trains

Planetary gear trains are preferred to simple gear trains because of their small sizes and low inertia, due to: *i*) load distribution; *ii*) high transmission in one stage, which eliminates the need for multi-step transmissions; and *iii*) use of internal mesh gears, which have a higher load-carrying capacity.

The major disadvantage of planetary reducers is the backlash. To cope with this problem, novel devices, such as harmonic drives and planetary cycloidal drives, have been developed in the past. Nevertheless, as shown in the next two paragraphs, we select planetary gear trains for Quasimoro TS design.

Harmonic Drives

Harmonic drives have been developed in 1955 primarily for aerospace applications. These speed reducers employ a non rigid gear called *flexspline.*

The most interesting advantage is the anti-backlash feature. However, many disadvantages characterize the choice of harmonic drives: *i*) **resonance vibration**, for torque ripples produced by non-rigid gear meshing can excite resonance, thereby producing high vibration amplitudes in some operating ranges (Taghirad, 1997); *ii*) **nonlinearity**, for compliance losses in the drive lead to nonlinear behaviour (Taghirad, 1997); and *iii*) **limited input speed**, because of the low fatigue endurance of the flexspline and low torsional stiffness (Rivin, 1988). Therefore, harmonic drives are not good candidates for the implementation of the TS of an easy to control robot like Quasimoro. Due to the flexspline, harmonic drives present hysteresis phenomena and resonance vibrations, which are more difficult to model, and hence, to control, than the nonlinearity introduced by backlash in ordinary planetary gear trains (Tao and Kokotovic, 1996).

Planetary Cycloidal Drives

Cycloidal planetary reducers should combine the positive features of planetary gear trains and harmonic drives (Rivin, 1988). An example of this device is a zero-backlash speed reducer currently under research at McGill University's Centre for Intelligent Machines (CIM): Speed-o-Cam. The latter is based on the layout of pure-rolling indexing cam mechanisms, and hence, eliminates backlash and friction; moreover, it also offers the possibility of high stiffness (González-Palacios and Angeles, 1999). However, Speed-o-Cam is not considered for the Quasimoro because of large dimensions, weight and cost. We also discard other planetary cycloidal drives since they are heavy and are characterized by non-uniformity of the output speed.

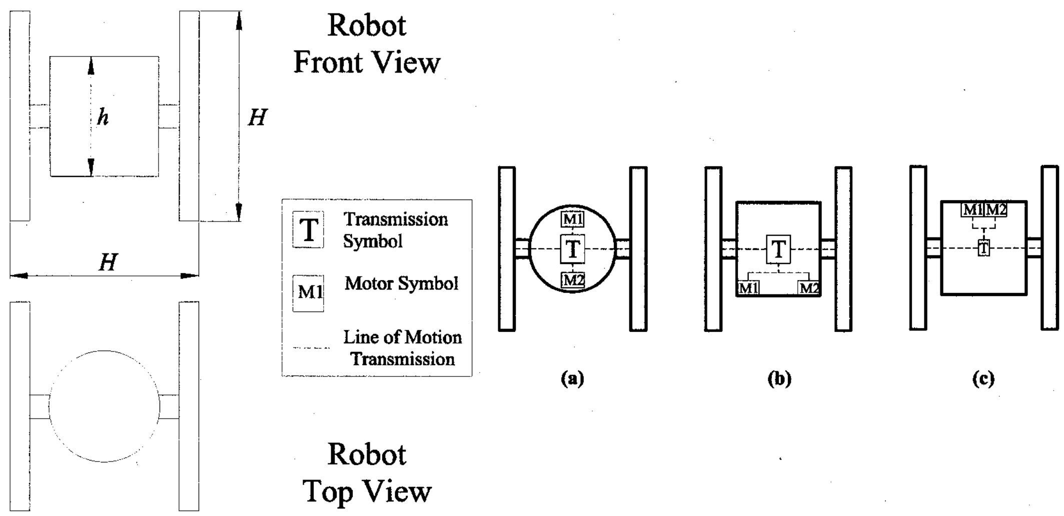

Figure 2.2: Common TS layouts

2.8 Analysis of Motor Layout

The analysis of different layout solutions of the actuation and transmission subsystems is derived in this Section, by referring to the sketches and symbols introduced in Fig. 2.2.

First, we analyze the problem of locating the motors, assuming that they are provided with a common TS. The motors and the TS can be positioned in three different ways: *i*) motors and TS are at the same height, so as to counterbalance the IB (Fig. 2.2a)[7]; *ii*) the TS is above the motors (Fig. 2.2b); *iii*) the motors are above the TS (Fig. 2.2c); The best solution is the second, since it is the most suited for accomplishing the task of stabilizing the robot when it is at rest, by lowering its MC.

Now, considering two separated TSs for the two wheel motors, we have the set of layouts of Fig. 2.3. The best layout is (a), because the other two give rise to a too high value of L, thus preventing the robot to swiftly navigate through narrow spaces. The solution of Fig. 2.3a is preferred, at this design stage, in order to avoid precession of the two motors generated by the oscillations of the IB with respect to the axis of the

[7]The motor symbol includes the planetary gearhead.

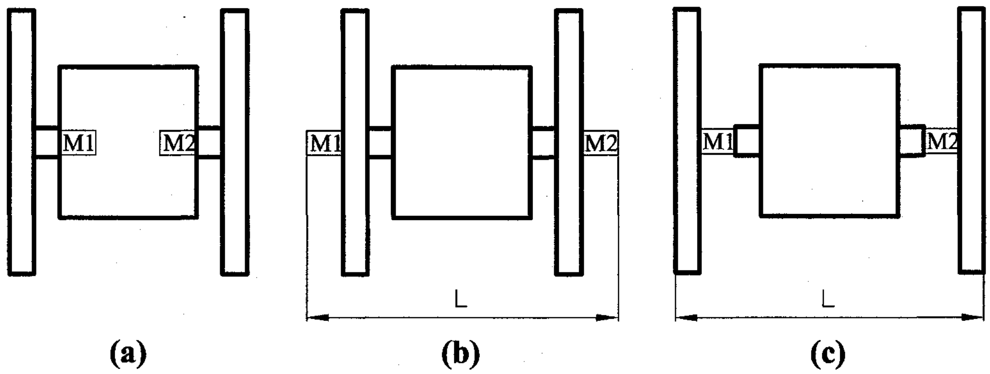

Figure 2.3: System layouts with decoupled TS

wheels. However, as explained in Chapter 4, the layout of Fig. 2.2b will be selected from an embodiment design standpoint.

2.9 Robot Specifications

Robot overall dimensions respect the following design constraints.

Width The robot is designed to fit residential doorways. The robot being teleoperated, its width is smaller than the 70% of the doorway width, in order to guarantee a safe passage through the doorway.

Length The robot is designed to allow manoeuvring through residential doorways.

Height The robot is designed not to intimidate the user with its size and allow the user a comfortable access to the payload.

In line with the design philosophy "a robot as a solution to specific problems" and adopting the motto "keep it simple", Quasimoro is *not* equipped with a serial manipulator for payload loading. The payload (food, drinks, etc.) is to be loaded on the tray of the robot by home-automatic distributors (food distributor, drink distributor, etc.), which represent a cost-effective result of modern domotics. More specifically, with reference to the strawman task of Section 2.1.1, once the robot reaches station R1, the ADD delivers a bottle of water on the tray.

DP	DVI	DP	DVI
Development Costs:	\$10–15 kCDN	Servicing Time:	3.5–5 h/month
Duty Factor:	16–19.2 h/day	Speed:	0.5–3m/s
Oper. Range:	100–120 m	Acceleration:	0.400–0.533 m/s^2
Oper. Time:	30–45 min/day	Max. Weight:	77.112 kg

Table 2.4: Design parameters (DPs) and design value intervals (DVIs)

In order to allow the user to control the robot and its functions in an intuitive fashion, the user control unit should be a personal computer (PC). The PC has been chosen because of its high pervasiveness. The PC is programmed in such a way to allow the user to choose two different control modes, namely *i) real-time* control; and *ii) pre-programmed* control. In the first control mode, the user controls in real time the robot by means of special keyboard keys. In the second control mode, the user types-in a number using the PC keyboard which commands the robot to fetch a specific item (food, drinks, etc.), associated with a pre-programmed path, e.g., with reference to Fig. 2.1a, the path joining robot home location (RHL), R1 and R2. In order to start the pre-programmed control, the robot has to lie on its home location (RHL in Fig. 2.1a). The RHL is chosen according to the needs of the user, e.g. a location not blocking the user's and visitor's actions. Upon the robot delivery, and every time the user requests it, a technician will provide assistance by pre-programming the desired paths according to the specific needs of the user. The pre-programmed control should be extremely useful for the mobility-challenged.

Quasimoro is also endowed with a wireless fidelity communication subsystem, which gives clear transmission data at the operating range specified in Table 2.4. In this regard, an on-board safety shutdown switch is a desired feature for the robot in the event that the robot communication is lost.

We list in Table 2.4 the robot specifications, which stem mainly from the strawman task of Fig. 2.1a.

2.10 Geometric Dimensioning

In order to ease its control, Quasimoro is designed so as to be endowed with quasi-holonomy property (see Chapter 3), which is achieved by placing the MC of the robot on the vertical passing through the midpoint of the segment defined by the wheel centres—see Section 3.2. Furthermore, Quasimoro is designed to have its MC below the wheel axis in order to feature a stable equilibrium point.

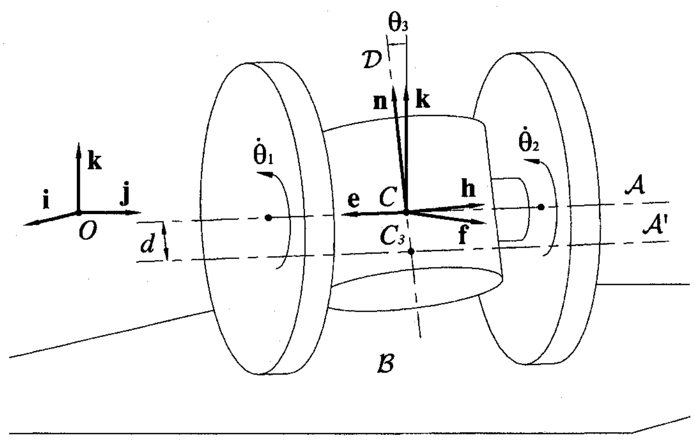

Figure 2.4: Simplified model of Quasimoro

According to the environment definition, see Subsection 2.1.1, the robot undergoes motion on a horizontal planar surface, $\mathcal{B}$. At this stage we neglect gently-sloped landscaping, which will be considered in the embodiment design, see Chapter 4. A simplified model of Quasimoro is shown in Fig. 2.4. The chassis of the IB is represented by a cylinder with the axis of symmetry $\mathcal{D}$ normal to the wheel axis.

Furthermore, we assume that *i*) during motion, the robot wheels are always in contact with $\mathcal{B}$ and under pure-rolling on the latter; and *ii*) the robot is free from dissipative forces.

With reference to Fig. 2.4, $\mathcal{A}$ is the axis passing through the centres of the wheels, while $\mathcal{A}'$ is the axis parallel to $\mathcal{A}$ and passing through the MC C_3 of the robot.

We define three orthonormal triads of vectors: $\{\mathbf{i}, \mathbf{j}, \mathbf{k}\}$, $\{\mathbf{e}, \mathbf{f}, \mathbf{k}\}$ and $\{\mathbf{e}, \mathbf{h}, \mathbf{n}\}$. The first defines an inertial frame attached to the ground with its origin O lying in the horizontal plane of C, the midpoint of the segment between the wheel centres.

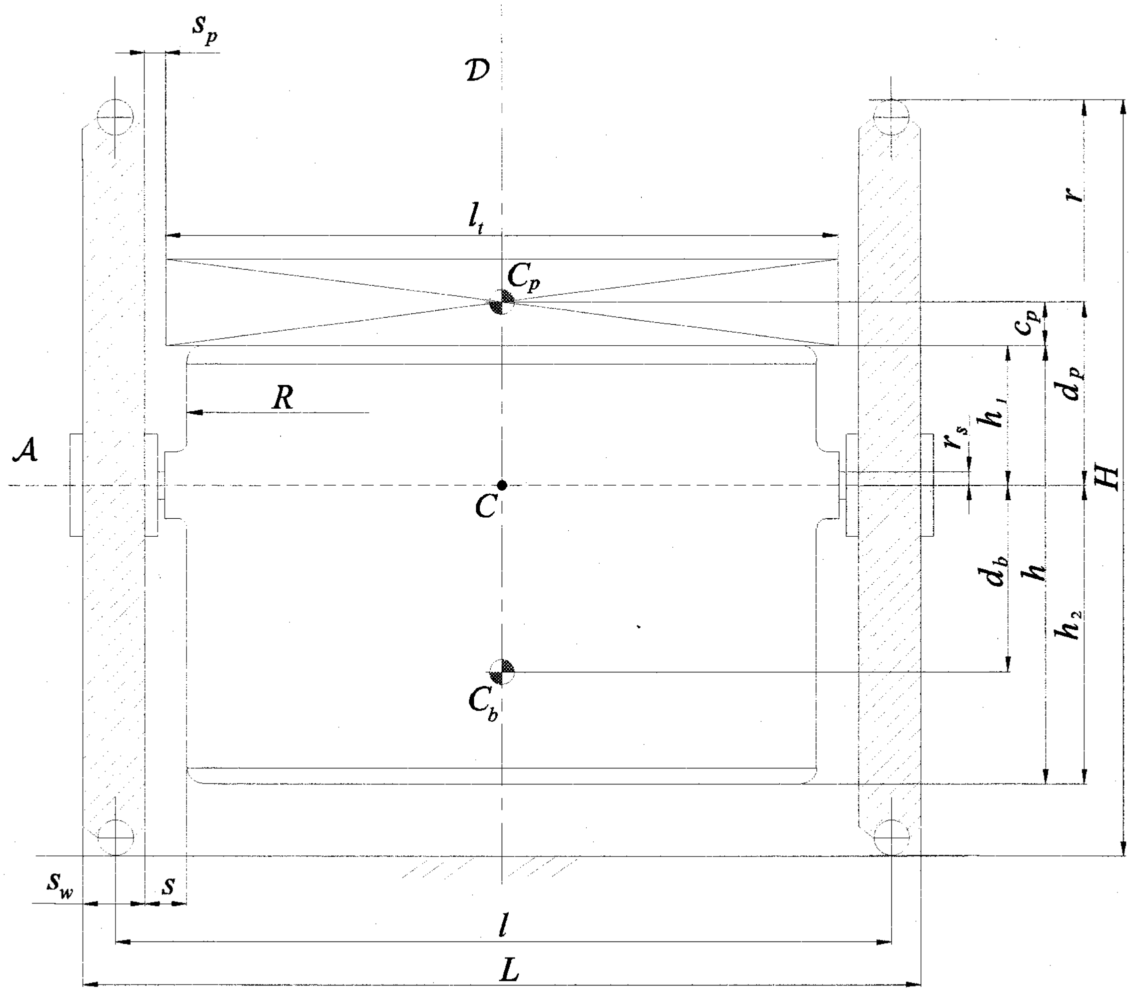

Figure 2.5: Quasimoro geometric parameters

The frame defined by $\{\mathbf{e}, \mathbf{f}, \mathbf{k}\}$ has its origin at C; in particular, $\mathbf{e}$ is parallel to $\mathcal{A}$, while $\mathbf{k}$ is vertical. The frame defined by $\{\mathbf{e}, \mathbf{h}, \mathbf{n}\}$ is attached to the IB and centred at C, while $\mathbf{n}$ lies on the $\mathcal{D}$ axis.

We indicate with θ_1 and θ_2 the angular displacements of the two wheels with respect to vector $\mathbf{k}$. We also define θ_3 as the tilt angle of the IB from the vertical, as indicated in Fig. 2.4.

In Fig. 2.5 we have represented the front view of the robot along with the payload. In order to derive a *conservative* geometric dimensioning, we consider the worst-case condition, namely a 70 N parallelepiped of homogeneous material having dimensions adopted in Subsection 2.1.1.

2.10.1 Design Variables

The overall dimensions of the robot are indicated by $H \times L \times H$. The chassis of the IB is represented by a cylinder, of radius R and height h. The set of *independent* robot architecture parameters is given by $\mathcal{X}_i \equiv \{r, h_1, h_2, R, r_s, d_b, d_p, c_p, s, s_w, s_p, m_w, m_b, m_p, J_{b,1}, J_{b,2}, J_{p,1}, J_{p,2}\}$, where r is the wheel radius, C_b is the MC of the IB, C_p is the MC of the payload, m_w is the mass of each augmented wheel (i.e., the wheel along with the shaft which actuates it), m_b is the mass of the IB and m_p is the mass of the payload. Moreover, $J_{b,1}$ and $J_{b,2}$ are the moments of inertia of the IB about its axis of symmetry $\mathcal{D}$ and about $\mathcal{A}$, respectively, $J_{p,1}$ and $J_{p,2}$ are the moments of inertia of the payload about $\mathcal{D}$ and $\mathcal{A}$, respectively, while h_1, h_2, d_b, d_p, c_P, s, s_w, and s_p are the linear dimensions reported in Fig. 2.5. The set of *dependent* robot architecture parameters is given by $\mathcal{X}_d \equiv \{l, L, H, m_3, J_1, J_2\}$, with the definitions below:

$$
\begin{aligned}
l &\equiv 2R + 2s + s_w, \quad L \equiv 2s_w + 2s + 2R = l + s_w, \quad m_3 \equiv m_b + m_p, \\
J_1 &\equiv J_{b,1} + J_{p,1}, \quad J_2 \equiv J_{b,2} + J_{p,2}, \quad M \equiv 2m_w + m_3, \quad d_p \equiv h_1 + c_p, \\
H &\equiv 2r, \qquad (2.2)
\end{aligned}
$$

with M denoting the overall mass of the robot, m_3 the mass of the augmented IB (i.e., the IB along with the payload), J_1 the moment of inertia of the augmented IB about its axis of symmetry, and J_2 the moment of inertia of the augmented IB about $\mathcal{A}$.

2.10.2 Design Constraints

Quasimoro has to be capable of turning in place while standing on the threshold of a doorway. In Fig. 2.6a, L_d represents the doorway width, while P indicates the intersection of the horizontal plane passing through C and the locus of points of the robot wheel which come into contact with the ground during a complete wheel

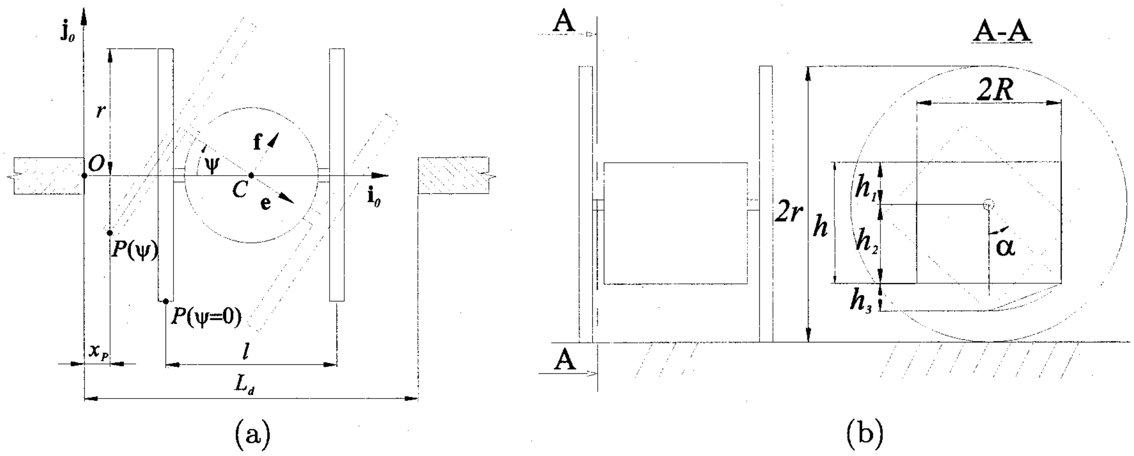

Figure 2.6: (a) door negotiation and (b) analysis of rotation of the IB

rotation. From Fig. 2.6a one can readily derive the constraint

$$r < \frac{1}{2}\left(\frac{L_d}{\sin\psi_0} - \frac{l}{\tan\psi_0}\right) \tag{2.3}$$

by computing the angle $\psi_0 = \arctan(2r/l)$ for which the $\mathbf{i}_0$-component of P, x_P, is a minimum.

Since Quasimoro has to comply with all the existing wheelchairs, formula (2.1) implies that

$$0.580\,\mathrm{m} \le H \le 0.590\,\mathrm{m}, \tag{2.4}$$

i.e., $0.290\,\mathrm{m} \le r \le 0.295\,\mathrm{m}$. In order to avoid damage to delicate components contained in the IB, such as the on-board control unit and payload, Quasimoro design is such that the IB is free to make a complete rotation about $\mathcal{A}$ without hitting the ground, i.e., from Fig. 2.6b,

$$r > \frac{R}{\sin[\arctan(R/h_2)]}. \tag{2.5}$$

Every WU, independent from her height, has to access the payload. Therefore, defining d_p as the distance of the payload MC from the wheel axis, we have: $d_p + r \ge 0.450\,\mathrm{m}$. In this inequality, 0.450 m indicates the value of the highest position of the tip of the user hand when she attempts to reach an object that lies on the floor (ESCWA, 2003).

As anticipated in Section 2.9 Quasimoro width $L \equiv l + s_w$ has to be less than 70% of a doorway width $L_d = 0.800\,\text{m}$. Therefore l has to respect the following inequality

$$l \leq 0.56 - s_w \ [\text{m}]. \tag{2.6}$$

From Fig. 2.5 we can infer that $l > 2R + s_w$, and that

$$l > 0.385 + s_w \ [\text{m}], \tag{2.7}$$

where 0.385 m is the length of the tray.

Indicating with r_{st} the external radius of the motor stator, we obtain $h_1 > r_{st}$. In order to locate C_b below $\mathcal{A}$ and to avoid interference between IB and ground, we impose the constraints $h_1 < h_2 < r$.

After having consulted manufacturer catalogues, it is reasonable to assume that the overall length of a DC motor is 0.180 m, including encoder and planetary gearhead (PG). Hence, the radius R of the cylindrical IB is lower-bounded according to design constraint

$$R > 0.180\,\text{m}. \tag{2.8}$$

In order to have the MC of the robot under full load lying below $\mathcal{A}$, the norm of the mass first moment ($\|\mathbf{q}_c\| = m_b d_b$) of the IB with respect to C is lower-bounded according to design constraint $m_b d_b > m_p d_p$.

2.11 Design Rationale

With reference to Fig. 2.5, R has to be as big as possible in order to facilitate robot maintenance, while l has to be as small as possible in order to ease robot navigation in cluttered or narrow environments.

The ratio $2m/m_b$ plays a key role in the accomplishment of the primary and secondary tasks of Quasimoro, which are associated with robot performance, path-following and functionality, for the former, and IB stabilization, for the latter. As a matter of fact, we have that *i*) designing the wheels much heavier than the IB reduces

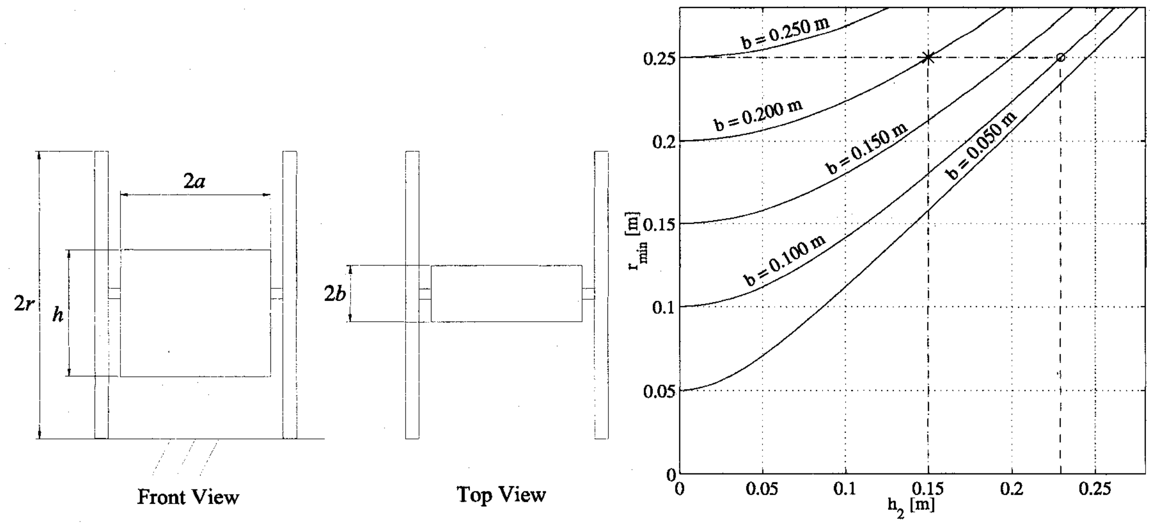

(a) (b)

Figure 2.7: (a) parallelepipedal IB; (b) diagram of the lower bound of r

the effect of the tilt angle oscillations on the robot performance; and *ii*) designing a massive IB reduces the tilt angle oscillations. In order to satisfy the requirements in terms of robot performance and functionality, a trade-off solution between *i*) and *ii*) is obtained using techniques of robust design (Salerno and Angeles, 2003c).

A parallelepiped geometry of the IB, see Fig. 2.7a, is preferred to the cylindrical one that has been initially proposed. The reason for this design choice is given below. First of all, the components fixed on the base of the IB will have a parallelepiped geometry; choosing the parallelepiped geometry leads to a better space-utilization. Second, by virtue of its geometry, the length and width of a parallelepiped can be different.

In Fig. 2.7b we include a plot of the function

$$r_{min}(b, h_2) = \frac{b}{\sin[\arctan(b/h_2)]}, \quad b \equiv R$$

which represents the lower bound of the wheel radius given by the constraint (2.5). From Fig. 2.7b we can infer that h_2 is smaller in the case of a cylindrical IB because $a = b = R$. More specifically, from constraint (2.8) we have: $a = b = R > 0.180\,\text{m} \Rightarrow a = b = R = 0.200\,\text{m}$. In the case of a parallelepipedal IB we have that h_2 is bigger because the constraint (2.8) does not affect the length $2b$ of the IB, but only the width $2a$, namely, $a > 0.180\,\mathrm{m}$, and hence, $a = 0.200\,\mathrm{m}$ for example. By choosing a parallelepipedal IB geometry we have increased h_2 by more than the 50%, from 0.150 m to 0.229 m, for a given wheel radius r of 0.250 m. This introduces a significant benefit to the robot performance by lowering its MC. As a matter of fact, the controllability test fails if the distance d of Fig. 2.4 is zero, see Section 3.3.

Finally, in order to lower the MC of the robot the ratios h_1/h_2 and h_1/r should be as small as possible.

2.12 Robot Proportions

In order to guarantee the user a comfortable access to the payload we need to make the robot as high as possible while respecting the inequality constraint (2.4). Therefore, we choose $H = 0.590\,\mathrm{m}$, whence $r = H/2 = 0.295\,\mathrm{m}$. In this light, one can assume: $s_w = 0.04\,\mathrm{m}$. For the given value of r, l has to be smaller than 0.572 m, according to constraint (2.3). From constraint (2.6), we obtain $l \leq 0.520\,\mathrm{m}$. Moreover, l is lower-bounded by the inequality constraint (2.7), which takes the form: $l > 0.385 + s_w$, whence $l > 0.425\,\mathrm{m}$. Therefore, l is bounded as: $0.425\,\mathrm{m} < l \leq 0.520\,\mathrm{m}$. In order to guarantee a comfortable loading and unloading of the tray, a minimum clearance of 0.055 m between wheels and tray is set. Therefore, $l = 0.480\,\mathrm{m}$. Hence $L = l + s_w = 0.480\,\mathrm{m} + 0.04\,\mathrm{m} = 0.520\,\mathrm{m}$, while the overall dimensions of the robot are given by $0.590\,\mathrm{m} \times 0.520\,\mathrm{m} \times 0.590\,\mathrm{m}$.

Chapter 3

Dynamics and Control

For the purpose of robot design a reasonably accurate model of the system is needed. In this Chapter, a simplified mathematical model of Quasimoro, appropriate for predicting robot behaviour, is described along with a controllability analysis of the system at hand.

3.1 Background on Quasiholonomic Systems

Although the geometric approach (Bloch, 2003; Liu and Li, 2002; Lewis, 2000; Cortés Monforte, 2002) to the study of NH systems has gained more and more interest in the past 30 years, these systems have continued to be investigated from a more *classic* perspective too. In a review of NH systems in the classic framework of analytical mechanics, QH systems were pointed out by Ostrovskaya and Angeles (1998). Such systems are NH systems whose dynamics is described by simple governing equations, formally identical to those of their holonomic counterparts. A QH robot is a NH system whose Coriolis and centrifugal generalized forces stemming from the kinematic constraints disappear. The outcome is that the mathematical model of a QH robot becomes formally identical to that of a holonomic system with the same mobility. Quasiholonomy eases the control, for the mathematical model becomes much simpler than otherwise.

Before introducing QH systems and detailing their advantages, we recall the concepts of *orthogonal complement* and *holonomy matrix*, resorting to the basic terminology of analytical mechanics (Pars, 1979).

One possibility to formulate the dynamics of generally constrained mechanical systems includes two tasks: elimination of the constraint forces and reduction of the dimension of the system; both tasks can be readily implemented by means of an orthogonal complement, as first proposed by Maggi (1901).

Let $\mathbf{q}$ be the n-dimensional vector of generalized coordinates of a mechanical system $\mathcal{M}$ having n *positional degrees of freedom*, subject to $p < n$ kinematic constraints. The latter being linear in the generalized velocities, they can be expressed in the form $\mathbf{A}(\mathbf{q}, t)\dot{\mathbf{q}} = \mathbf{b}(\mathbf{q}, t)$, where the $p \times n$ matrix $\mathbf{A}$ and the p-dimensional vector $\mathbf{b}$ are functions of the generalized coordinates and, possibly, time. Let $\mathbf{u}(t)$ be a $m = n - p$-dimensional vector of *independent generalized-velocities.* Moreover, we let $\mathbf{N}(\mathbf{q})$ be a $n \times m$ matrix mapping vector $\mathbf{u}$ into a vector of *feasible generalized-velocities* $\dot{\mathbf{q}}$. What we mean by feasible is a vector $\dot{\mathbf{q}}$ that obeys the kinematic constraints, i.e., $\dot{\mathbf{q}}(t) = \dot{\mathbf{q}}_0(t) + \mathbf{N}(\mathbf{q})\mathbf{u}(t)$, with $\dot{\mathbf{q}}_0(t)$ being a *particular solution* of the constraint equations. Hence, $\mathbf{N}$ turns out to be an orthogonal complement (Golub and Van Loan, 1996) of $\mathbf{A}$, i.e. $\mathbf{A}\mathbf{N} = \mathbf{O}_{pm}$, where $\mathbf{O}_{pm}$ is the $p \times m$ zero matrix. Using a novel approach, based on the holonomy matrix (Ostrovskaya and Angeles, 1998), the *Lagrange equations* of the *first kind* (Pars, 1979)[1]

$$\frac{d}{dt}\left(\frac{\partial L}{\partial \dot{\mathbf{q}}}\right) - \frac{\partial L}{\partial \mathbf{q}} = \boldsymbol{\phi} + \mathbf{A}^T\boldsymbol{\lambda}\ , \tag{3.1}$$

can be reduced to the *constrained*, i.e., *reduced*, *Lagrange equations*, namely,

$$\frac{d}{dt}\left(\frac{\partial \tilde{L}}{\partial \mathbf{u}}\right) - \mathbf{N}^T\frac{\partial \tilde{L}}{\partial \mathbf{q}} + \mathbf{H}^T\mathbf{p} = \mathbf{N}^T\boldsymbol{\phi}\ , \tag{3.2}$$

where: $\boldsymbol{\lambda}$ is the vector of *Lagrange multipliers*; $\mathbf{p} = \partial L/\partial\dot{\mathbf{q}}$ is the *unconstrained* generalized momentum of the system; $\boldsymbol{\phi}$ is the m-dimensional vector of *unconstrained*

[1]These equations are formulated in terms of dependent generalized-coordinates, which require the introduction of *constraint forces* $\mathbf{A}^T\boldsymbol{\lambda}$; those of the *second kind* are formulated in terms of independent generalized-velocities.

generalized forces; $\mathbf{N}$ is the orthogonal complement defined above; L is the system Lagrangian; $\mathbf{u}$ is the vector of m-independent generalized-velocities of the system; and $\tilde{L} = L|_{\dot{\mathbf{q}} \to \mathbf{u}}$, i.e., $\tilde{L}$ is obtained by substituting the vector of feasible generalized-velocities into L, and is termed the *constrained Lagrangian* of the system. Note that $\tilde{L}$ as well as matrix $\mathbf{N}$ are, in general, functions of all n components of $\mathbf{q}$. The coefficient $\mathbf{H}^T$ of the *unconstrained generalized momentum* $\mathbf{p}$ in (3.2) is the transpose of the *holonomy matrix*, as introduced in (Ostrovskaya and Angeles, 1998), i.e.,

$$\mathbf{H} \equiv \frac{\partial(\mathbf{N}\mathbf{u})}{\partial \mathbf{q}}\mathbf{N} - \dot{\mathbf{N}} \ . \tag{3.3}$$

In this light, we have:

Definition 3.1.1. *A system is* nonholonomic iff $\mathbf{H} \neq \mathbf{O}_{n\times m}$.

Definition 3.1.2. *A system is* quasiholonomic iff $\mathbf{H} \neq \mathbf{O}_{n\times m}$ *and* $\mathbf{H}^T\mathbf{p} = \mathbf{0}_m$.

QH systems can be interpreted as NH systems whose generalized inertia-force terms stemming from the kinematic constraints disappear.

If a system is QH and the vector of independent generalized-velocities $\mathbf{u}$ is chosen so that it is a total time-derivative $\mathbf{u} \equiv \dot{\mathbf{s}}$, then a *simpler* set of Lagrange's equations of the system at hand can be written in the form

$$\frac{d}{dt}\left(\frac{\partial \tilde{L}}{\partial \dot{\mathbf{s}}}\right) - \frac{\partial \tilde{L}}{\partial \mathbf{s}} = \mathbf{N}^T\boldsymbol{\phi} \ , \tag{3.4}$$

which is formally identical to the Lagrange equations of a m-dof holonomic system.

Two essential results are recalled, whose proofs can be found in (Ostrovskaya, 2001) (pp. 40–42)[2]:

Theorem 3.1.1. *Quasiholonomy is invariant with respect to changes of independent generalized-coordinates.*

Theorem 3.1.2. *Quasiholonomy is invariant with respect to changes of independent generalized-velocity vector* $\mathbf{u}$ *if* $\mathbf{u}$ *is a total time-derivative.*

[2] `http://www.cim.mcgill.ca/~rmsl/Angeles_html/publications/ostrovskaya.pdf`

These theorems ensure that a "correct" choice of variables $\mathbf{q}$ or $\mathbf{u} = \dot{\mathbf{s}}$, where $\mathbf{s} \in \mathbb{R}^{m}$, leading to quasiholonomy is not needed. If it is found that the system is QH in one particular set of $\mathbf{q}$ and $\mathbf{u} = \dot{\mathbf{s}}$, then it is so in any other set, provided that the components of $\mathbf{q}$ as well as those of $\mathbf{u}$ are independent, and that they uniquely describe the configuration and the motion of the system, with $\mathbf{u}$ being, additionally, a total time-derivative (Ostrovskaya, 2001).

3.1.1 Advantages of Quasiholonomy

Quasiholonomy brings about several advantages in the control of NH mechanical systems. As proven in the sequel, quasiholonomy simplifies the CTC of NH systems. Therefore, the partial linearization (PL) of NH systems (d'Andrea-Novel et al., 1992; Bloch et al., 1992; De Luca and Oriolo, 1995), is simplified as well.

Let us consider a *catastatic*[3] mechanical system $\mathcal{M}$ subject to p first-order scleronomic NH constraints with n positional degrees of freedom (Ostrovskaya and Angeles, 1998), namely,

$$\mathbf{A}(\mathbf{q})\dot{\mathbf{q}} = \mathbf{0}, \tag{3.5}$$

where $\mathbf{A}$ is the $p \times n$ constraint matrix and $\mathbf{q}$ is the n-dimensional vector of generalized coordinates. In this case the kinetic energy is a quadratic homogeneous function of the generalized velocities (Ostrovskaya and Angeles, 1998) and the constrained Lagrangian takes the form

$$\tilde{L}(\mathbf{q}, \mathbf{u}) = \frac{1}{2}\mathbf{u}^{T}\mathbf{I}(\mathbf{q})\mathbf{u} - V(\mathbf{q}), \tag{3.6}$$

where: $\mathbf{I}(\mathbf{q}) = \mathbf{N}^{T}\mathbf{M}\mathbf{N} > 0$; $\mathbf{M}(\mathbf{q})$ is the *unconstrained generalized inertia matrix*; $\mathbf{N}$ is an orthogonal complement of the constraint matrix $\mathbf{A}$; $\mathbf{u}$ is the m-dimensional vector of independent generalized-velocities; and $V(\mathbf{q})$ is the potential energy. Moreover, the unconstrained generalized momentum takes the form

$$\mathbf{p} = \frac{\partial L(\mathbf{q}, \dot{\mathbf{q}})}{\partial \dot{\mathbf{q}}} = \frac{\partial}{\partial \dot{\mathbf{q}}}\left(\frac{1}{2}\dot{\mathbf{q}}^{T}\mathbf{M}\dot{\mathbf{q}} - V\right) = \mathbf{M}\dot{\mathbf{q}} = \mathbf{M}\mathbf{N}\mathbf{u}, \tag{3.7}$$

[3]In the realm of classical mechanics, a system is called "catastatic" when, upon setting all its generalized velocities to zero, its kinetic energy vanishes; otherwise, the system is termed *acatastatic.*

Using the holonomy matrix approach (Ostrovskaya and Angeles, 1998), the reduced Lagrange equations of $\mathcal{M}$ take the form (3.2). Assuming that the number of external inputs equals the mobility m of the system, and substituting eqs. (3.6) and (3.7) into eq. (3.2), we have

$$\mathbf{I}\dot{\mathbf{u}} + \mathbf{n}(\mathbf{q}, \mathbf{u}) = \mathbf{N}^T\mathbf{S}\boldsymbol{\tau}, \tag{3.8}$$

where $\mathbf{S}$ is a full-rank $n \times m$ matrix mapping the m-dimensional vector of external inputs (De Luca and Oriolo, 1995) $\boldsymbol{\tau}$ into the vector of unconstrained generalized forces and

$$\mathbf{n}(\mathbf{q}, \mathbf{u}) = \dot{\mathbf{I}}\mathbf{u} - \frac{\mathbf{N}^T}{2}\left(\frac{\partial}{\partial \mathbf{q}}(\mathbf{u}^T\mathbf{I}\mathbf{u})\right) + \mathbf{N}^T\frac{\partial V}{\partial \mathbf{q}} + \mathbf{H}^T\mathbf{M}\mathbf{N}\mathbf{u}. \tag{3.9}$$

The $(n+m)$-dimensional *reduced state-space model*, obtained by merging the kinematic model of eq. (3.5) and the dynamics model of eq. (3.8) is given by (De Luca and Oriolo, 1995)

$$\begin{aligned} \dot{\mathbf{q}} &= \mathbf{N}(\mathbf{q})\mathbf{u}, \\ \dot{\mathbf{u}} &= \mathbf{I}^{-1}(\mathbf{q})\mathbf{N}^T(\mathbf{q})\mathbf{S}(\mathbf{q})\boldsymbol{\tau} - \mathbf{I}^{-1}(\mathbf{q})\mathbf{n}(\mathbf{q}, \mathbf{u}). \end{aligned}$$

Introducing the non-restrictive assumption that $\mathbf{N}^T\mathbf{S}$ is of full rank (Campion et al., 1991), we perform a PL of the reduced state-space model via a CTC scheme, thereby obtaining

$$\boldsymbol{\tau} = [\mathbf{N}^T(\mathbf{q})\mathbf{S}(\mathbf{q}))^{-1}(\mathbf{I}(\mathbf{q})\mathbf{a} + \mathbf{n}(\mathbf{q}, \mathbf{u})] \tag{3.10}$$

where $\mathbf{a} \in \mathbb{R}^m$ is a new vector of control inputs, which is obtained by the application of linear control strategies. The system thus resulting is

$$\begin{aligned} \dot{\mathbf{q}} &= \mathbf{N}(\mathbf{q})\mathbf{u}, \\ \dot{\mathbf{u}} &= \mathbf{a}, \end{aligned}$$

where the first n equations represent the kinematic model and the last m equations act as a dynamic extension (De Luca and Oriolo, 1995). Vector $\mathbf{a}$ can be chosen as $\mathbf{a} = -\mathbf{K}_p\mathbf{q} - \mathbf{K}_d\dot{\mathbf{q}} + \mathbf{r}$, where $\mathbf{r} = \ddot{\mathbf{q}}_d + \mathbf{K}_d\dot{\mathbf{q}}_d + \mathbf{K}_p\mathbf{q}_d$, $\mathbf{q}_d$ is the vector of desired generalized coordinates, $\mathbf{K}_d$ and $\mathbf{K}_p$ are two positive definite matrices (Sciavicco and Siciliano, 2000).

Hence, it is possible to cancel dynamic terms via nonlinear feedback assuming that *i*) the dynamics model is exactly known, and *ii*) the complete system state is measurable (De Luca and Oriolo, 1995). Hence, we have,

Claim 3.1.1. *If $\mathcal{M}$ is endowed with the quasiholonomy property, the last term $\mathbf{H}^T\mathbf{MNu}$ of $\mathbf{n}$, as displayed in eq. (3.9), vanishes, thereby reducing the computational complexity of the computed-torque controller described in eq. (3.10).*

Remark 3.1.1. *If, besides being QH, $\mathcal{M}$ is* underactuated, *i.e. $\boldsymbol{\tau}$ is l-dimensional, with $l < m$, then Claim 3.1.1 still holds.*

This remark can be readily proven by noting that if $\mathcal{M}$ is QH and underactuated, then one can still conduct a *partial linearization* (De Luca and Oriolo, 2000) of eq. (3.8). This can be done via a computed-torque control scheme, in order to linearize the l equations of eq. (3.8), in which the components of $\boldsymbol{\tau}$ explicitly appear. If $\mathcal{M}$ is QH, the foregoing computed-torque control scheme will simplify in the same way as eq. (3.10) did, since $\mathbf{H}^T\mathbf{MNu}$ vanishes.

Control

Implementation of CTC schemes requires eq. (3.10) to be computed in real time. This computation is to be performed at sampling times of the order of 1 ms so as to comply with Shannon's Theorem (Åström and Wittenmark, 1997) and ensure that the assumption of operating in the continuous time domain is realistic (Sciavicco and Siciliano, 2000). This may pose severe constraints on the hardware/software architecture of the robot control system (Sciavicco and Siciliano, 2000). To cope with this issue, one can lighten the computations involved in eq. (3.10) by endowing the system with quasiholonomy. It is noteworthy that the computational complexity is strongly reduced in the case of large scale systems. Moreover, one can readily infer that for a QH system: *i*) the implementation of the control scheme (3.10) will return a faster controller, since, in principle, fewer floating-point operations (flops) per second will be required for the computation of the command signal; *ii*) the computational complexity of CTC algorithms will be reduced; *iii*) the implementation of the control scheme (3.10) will return a more accurate controller, since the round-off error will be smaller, the computation of the command signal requiring fewer numerical calculations; and *iv*) if $\mathbf{u}$ is a total time-derivative, standard control strategies for holonomic systems, such as robotic manipulators (Sciavicco and Siciliano, 2000), can be applied to control the virtual holonomic system. In this light, QH systems turn out to be extremely useful when the dynamics model is needed in their control, for example, in applications imposing high speeds, high loads, or both (Shekkar, 1997; Hong et al., 1999).

For a generic WMR composed of a main body and N conventional, off-centered orientable wheels with independently powered steering and rotation axes the term $\mathbf{H}^T\mathbf{MNu}$ takes the following form (Salerno et al., 2002)

$$\mathbf{H}^T\mathbf{MNu} = \frac{1}{l^3}\left(\frac{mr^2}{4} + J_b\right)\sum_{i=1}^{N}\begin{bmatrix}\mathbf{E}^T\dot{\mathbf{p}}_i \\ -b\dot{\mathbf{c}}^T\mathbf{e}_i\end{bmatrix}\boldsymbol{\eta}_i^T\dot{\mathbf{p}}_i\,. \tag{3.11}$$

The number of flops associated with the computation of the coefficient of the foregoing summation is $9M + 1A$, where M indicates a multiplication while A represents an addition. Moreover, for each of the terms of the foregoing sum we record the number of flops in Table 3.1. Moreover, performing the sum of eq. (3.11) entails $3(N-1)A$.

$\mathbf{p}_i$	$\leftarrow$	$\mathbf{c}_i - l\boldsymbol{\xi}_i$	$(2M + 2A)$
$\dot{\mathbf{p}}_i$	$\leftarrow$	$\dot{\mathbf{c}}_i - l(\dot{\psi} + \dot{\psi}_i)\boldsymbol{\eta}_i$	$(4M + 4A)$
$\boldsymbol{\eta}_i^T\dot{\mathbf{p}}_i$			$(2M + 1A)$
$-b\dot{\mathbf{c}}^T\mathbf{e}_i$			$(4M + 1A)$
$\mathbf{E}^T\dot{\mathbf{p}}_i$			$(4M + 2A)$
$\begin{bmatrix}\mathbf{E}^T\dot{\mathbf{p}}_i \\ -b\dot{\mathbf{c}}^T\mathbf{e}_i\end{bmatrix}\boldsymbol{\eta}_i^T\dot{\mathbf{p}}_i$			$3M$
			$(19M + 10A)$

Table 3.1: Number of flops

Therefore, the number N_f of flops associated with the computation of $\mathbf{H}^T\mathbf{MNu}$ is

$$N_f = (19M + 10A)N + 9M + 1A + 3(N-1)A = (19N + 9)M + (13N - 2)A.$$

Hence, the amount of flops saved by virtue of quasiholonomy for this type of robots is $(19N+9)M+(13N-2)A$.

The quasiholonomy property introduces also a few advantages for the numerical analysis of NH systems. Since the nonholonomy term vanishes, the integration of the Lagrange equations is correspondingly faster (fewer flops) and more accurate (reduced round-off error) (Salerno et al., 2002). The reader can convince herself of this by comparing the Lagrange equations of a NH system, described by eq. (3.2), and those of the virtual holonomic system, described by eq. (3.4). From this comparison one can readily infer that the integration of the Lagrange equations of a QH system requires fewer calculations than those of the corresponding NH system.

The main simplification introduced by quasiholonomy in the analysis and control of nonholonomic systems lies in that their dynamics model can be represented using the typical form of Lagrange's equations that is valid for holonomic systems.

3.1.2 Design for Quasiholonomy

From Definition 3.1.2, one can attempt to derive design conditions in order to endow a system with quasiholonomy.

As shown in Section 3.2, Quasimoro achieves quasiholonomy by a combination of design decisions: *i*) the mass centre of the robot is located on the (vertical) plane equidistant from the two wheel mid-planes (design decision) and *ii*) the IB is kept vertical by the robot drive system which dampens the oscillations.

We produce below some general guidelines for robot design for quasiholonomy (Salerno et al., 2002).

If a WMR is omnidirectional, then the nonholonomy term, $\mathbf{H}^T\mathbf{p}$, of the governing equations (3.2) contains neither the mass nor the moment of inertia of its platform. This means that the nonholonomy term can be rendered zero and, therefore, the robot can be rendered QH, provided that the wheels of the robot are designed to be significantly light when compared with the robot chassis. In this case, the inertia properties of the wheel mechanism can be neglected while calculating the kinetic energy of the whole robot; one can then model the robot without considering the nonholonomy term in the governing equations.

If a WMR has axial symmetry, like Quasimoro, then it belongs to the Chaplygin-type of nonholonomic systems (Neimark and Fufaev, 1972). In this case, the quasi-holonomic WMR can be modeled as a virtual holonomic system with its degrees of freedom (dof) m equal to the mobility of the original nonholonomic system and the same Lagrangian as the original system. This means that instead of dealing with a system of m second-order differential equations and p first-order differential equations, one can integrate these two systems separately. Therefore, the control of the whole system can be divided into two parts, namely, (*a*) the dynamic control of system (3.4) and (*b*) the kinematic control of the constraints (Larin, 2000).

3.2 Mathematical Model

Depicted in Fig. 2.4 is a simplified model of Quasimoro. The mathematical model of Quasimoro is formulated in the framework of the Lagrange formalism based on the holonomy matrix (Ostrovskaya, 2001). We make the same assumptions detailed at the beginning of Section 2.10.

Defining[4] l as the distance between the centres of the wheels, r as the wheel radius and $\bar{\mathbf{c}}$ as the two-dimensional position vector of point C in the inertial frame[5], we have the constraints (Salerno and Angeles, 2005)

$$\dot{\bar{\mathbf{c}}} = \mathbf{P}\dot{\boldsymbol{\theta}}_a, \quad \dot{\psi} = \rho(\dot{\theta}_2 - \dot{\theta}_1) \tag{3.12}$$

where $\rho = r/l$, $\boldsymbol{\theta}_a = [\ \theta_1 \quad \theta_2\ ]^T$, $\mathbf{P}(\theta_1, \theta_2) = (r/2)[\ \bar{\mathbf{f}} \quad \bar{\mathbf{f}}\ ]$, ψ is the robot steering angle, i.e., the angle between vectors $\mathbf{i}$ and $\mathbf{e}$[6]. Integrating the second relation in eqs. (3.12) we obtain: $\psi = \rho(\theta_2 - \theta_1)$, where we have assumed $\psi = 0$ when $\theta_1 = \theta_2$. Further, we define $\mathbf{q} = [\ \bar{\mathbf{c}}^T \quad \theta_1 \quad \theta_2 \quad \theta_3\ ]^T$ as the five-dimensional vector of generalized

[4] l should not be confused with the dimension of $\boldsymbol{\tau}$ defined in Remark 3.1.1.

[5] Given $\mathbf{a} \in \mathbb{R}^3$, we indicate with $\bar{\mathbf{a}} \in \mathbb{R}^2$ the representation of $\mathbf{a}$ in the $\{\mathbf{i}, \mathbf{j}\}$ plane, where $\mathbf{i}$ and $\mathbf{j}$ are defined in Section 2.10.

[6] θ_1, θ_2, $\mathbf{e}$, and $\mathbf{f}$ are defined in Section 2.10.

coordinates, where θ_3 is defined in Section 2.10. Defining $\mathbf{1}_k$ as the $k \times k$ identity matrix, the first of eqs. (3.12) can be rewritten as $\mathbf{A}\dot{\mathbf{q}} = \mathbf{0}_2$, where $\mathbf{A} = [\ \mathbf{1}_2 \quad -\mathbf{P} \quad \mathbf{0}_2\ ]$ is the 2×5 constraint matrix. Looking at the number of kinematic constraints and of generalized-velocities, we can conclude that the robot has $m = n - p = 5 - 2 = 3$ independent generalized-velocities. If we define the independent generalized-velocity vector as $\mathbf{u} = [\ \dot{\theta}_1 \quad \dot{\theta}_2 \quad \dot{\theta}_3\ ]^T$, an orthogonal complement of $\mathbf{A}$ is readily derived as

$$\mathbf{N} = \begin{bmatrix} \mathbf{P} & \mathbf{0}_2 \\ \mathbf{1}_2 & \mathbf{0}_2 \\ \mathbf{0}_2^T & 1 \end{bmatrix}.$$

Therefore,

$$\mathbf{Nu} = \begin{bmatrix} (r/2)(\dot{\theta}_1 + \dot{\theta}_2)\bar{\mathbf{f}} \\ \dot{\theta}_1 \\ \dot{\theta}_2 \\ \dot{\theta}_3 \end{bmatrix}.$$

From Fig. 2.4 and the second of eqs. (3.12),

$$\dot{\bar{\mathbf{f}}} = -\dot{\psi}\bar{\mathbf{e}} = \rho(\dot{\theta}_1 - \dot{\theta}_2)\bar{\mathbf{e}} = \rho[\ \bar{\mathbf{e}} \quad -\bar{\mathbf{e}}\ ]\dot{\boldsymbol{\theta}}_a.$$

It is apparent from the above equation that

$$\partial\bar{\mathbf{f}}/\partial\boldsymbol{\theta}_a = \rho[\ \bar{\mathbf{e}} \quad -\bar{\mathbf{e}}\ ]. \tag{3.13}$$

Moreover, $\bar{\mathbf{f}}$ is apparently independent of $\bar{\mathbf{c}}$, and hence,

$$\frac{\partial(\mathbf{Nu})}{\partial\mathbf{q}} = \frac{r}{2}(\dot{\theta}_1 + \dot{\theta}_2)\begin{bmatrix} \mathbf{O}_{2\times2} & \partial\bar{\mathbf{f}}/\partial\boldsymbol{\theta}_a & \mathbf{0}_2 \\ \mathbf{O}_{3\times3} & \mathbf{O}_{3\times2} & \mathbf{0}_3 \end{bmatrix}.$$

Therefore,

$$\frac{\partial(\mathbf{Nu})}{\partial\mathbf{q}}\mathbf{N} = \frac{r}{2}(\dot{\theta}_1 + \dot{\theta}_2)\begin{bmatrix} \partial\bar{\mathbf{f}}/\partial\boldsymbol{\theta}_a & \mathbf{0}_2 \\ \mathbf{O}_{3\times2} & \mathbf{0}_3 \end{bmatrix}$$

and using eq. (3.13),

$$\frac{\partial(\mathbf{Nu})}{\partial\mathbf{q}}\mathbf{N} = \frac{r}{2}\rho(\dot{\theta}_1 + \dot{\theta}_2)\begin{bmatrix} \bar{\mathbf{e}} & -\bar{\mathbf{e}} & \mathbf{0}_2 \\ \mathbf{0}_3 & \mathbf{0}_3 & \mathbf{0}_3 \end{bmatrix}. \tag{3.14}$$

Furthermore,

$$\dot{\mathbf{N}} = \frac{r}{2}\begin{bmatrix} \dot{\bar{\mathbf{f}}} & \dot{\bar{\mathbf{f}}} & \mathbf{0}_2 \\ \mathbf{0}_3 & \mathbf{0}_3 & \mathbf{0}_3 \end{bmatrix} = -\frac{r}{2}\rho(\dot{\theta}_2 - \dot{\theta}_1)\begin{bmatrix} \bar{\mathbf{e}} & \bar{\mathbf{e}} & \mathbf{0}_2 \\ \mathbf{0}_3 & \mathbf{0}_3 & \mathbf{0}_3 \end{bmatrix}. \tag{3.15}$$

Hence, the holonomy matrix can be readily computed as (Salerno and Angeles, 2005):

$$\mathbf{H} = \frac{\partial(\mathbf{Nu})}{\partial \mathbf{q}}\mathbf{N} - \dot{\mathbf{N}} = r\rho \begin{bmatrix} \dot{\theta}_2\bar{\mathbf{e}} & -\dot{\theta}_1\bar{\mathbf{e}} & \mathbf{0}_2 \\ \mathbf{0}_3 & \mathbf{0}_3 & \mathbf{0}_3 \end{bmatrix},$$

i.e. Quasimoro is a nonholonomic robot ($\mathbf{H} \neq \mathbf{O}$) (Salerno and Angeles, 2005), as one should have expected.

The total kinetic energy of the system is given by

$$T = T_{w1} + T_{w2} + T_3, \tag{3.16}$$

where T_{wi} is the kinetic energy of the i augmented wheel, i.e., the wheel along with the shaft which actuates it) while T_3 is the kinetic energy of the intermediate body, which includes the actuation system, the trasmission mechanism, the batteries, and the control unit.

It can be readily shown that the first two terms of the right-hand side of eq. (3.16) take the form

$$T_{w1} + T_{w2} = m_w\|\dot{\bar{\mathbf{c}}}\|^2 + \frac{m_w r^2}{4}(1+\rho^2)(\dot{\theta}_2 - \dot{\theta}_1)^2 + \frac{m_w r^2}{4}(\dot{\theta}_1^2 + \dot{\theta}_2^2),$$

where m_w is the mass of each augmented wheel.

Defining $\bar{\mathbf{c}}_3$ as the two-positional vector of point C_3, the kinetic energy T_3 is given by

$$T_3 = \frac{1}{2}m_3\|\dot{\bar{\mathbf{c}}}_3\|^2 + \frac{1}{2}J_1(\dot{\theta}_2 - \dot{\theta}_1)^2\rho^2\cos\theta_3{}^2 + \frac{1}{2}J_3(\dot{\theta}_2 - \dot{\theta}_1)^2\rho^2\sin\theta_3{}^2 + \frac{1}{2}J_2'\dot{\theta}_3^2,$$

where m_3 is the augmented mass of the IB, i.e., taking into account the payload; J_1 is the moment of inertia of the IB about $\mathcal{D}$; J_2' is the moment of inertia of the IB about $\mathcal{A}'$; J_3 is the moment of inertia of the IB about the axis passing through the unit vector $\mathbf{h}$.

Moreover, we have

$$\dot{\bar{\mathbf{c}}}_3 = \dot{\bar{\mathbf{c}}} + d\dot{\theta}_3\bar{\mathbf{h}} - \rho(\dot{\theta}_2 - \dot{\theta}_1)d\sin\theta_3\bar{\mathbf{e}},$$

where $\mathbf{h}$ is defined in Section 2.10 while d is the distance between C and C_3. Therefore,

$$\begin{aligned} T_3 &= \frac{1}{2}m_3(\dot{\bar{\mathbf{c}}} + d\dot{\theta}_3\bar{\mathbf{h}} - \rho(\dot{\theta}_2 - \dot{\theta}_1)d\sin\theta_3\bar{\mathbf{e}})^2 + \frac{1}{2}J_1(\dot{\theta}_2 - \dot{\theta}_1)^2\rho^2\cos{\theta_3}^2 + \\ &+ \frac{1}{2}J_2(\dot{\theta}_2 - \dot{\theta}_1)^2\rho^2\sin{\theta_3}^2 + \frac{1}{2}J_2'\dot{\theta}_3^2. \end{aligned}$$

Without considering the constant contributions of the augmented wheels, the potential energy of the system is

$$V = -m_3 dg\cos\theta_3,$$

where g is the gravity acceleration. In this light the Lagrangian $L = T - V$ of the system is given by

$$\begin{aligned} L &= m_w\|\dot{\bar{\mathbf{c}}}\|^2 + \frac{m_w r^2}{4}(1+\rho^2)(\dot{\theta}_2 - \dot{\theta}_1)^2 + \frac{m_w r^2}{4}(\dot{\theta}_1^2 + \dot{\theta}_2^2) + \frac{1}{2}J_{2'}\dot{\theta}_3^2 \\ &+ \frac{1}{2}m_3(\dot{\bar{\mathbf{c}}} + d\dot{\theta}_3\bar{\mathbf{h}} - \rho(\dot{\theta}_2 - \dot{\theta}_1)d\sin\theta_3\bar{\mathbf{e}})^2 - m_3 rg + m_3 dg\cos\theta_3 \\ &+ \frac{1}{2}(J_3\sin{\theta_3}^2 + J_1\cos{\theta_3}^2)(\dot{\theta}_2 - \dot{\theta}_1)^2\rho^2. \end{aligned}$$

where $\dot{\theta}_- \equiv \dot{\theta}_2 - \dot{\theta}_1$. Hence, the generalized momentum, obtained upon computing $\partial L/\partial\dot{\mathbf{q}}$ and then substituting $\dot{\mathbf{q}}$ into the latter, takes the form (Salerno and Angeles, 2005):

$$\mathbf{p} = \left.\frac{\partial L}{\partial\dot{\mathbf{q}}}\right|_{\dot{\mathbf{q}}\to\mathbf{u}} = \begin{bmatrix} M\mathbf{P}\dot{\boldsymbol{\theta}}_a + m_3 d(\dot{\theta}_3\bar{\mathbf{h}} - \rho\dot{\theta}_-\sin\theta_3\bar{\mathbf{e}}) \\ 1/2(m_w r^2)\dot{\theta}_1 - (H + m_3\rho^2 d^2\sin^2\theta_3)\dot{\theta}_- \\ 1/2(m_w r^2)\dot{\theta}_2 + (H + m_3\rho^2 d^2\sin^2\theta_3)\dot{\theta}_- \\ K\cos\theta_3\dot{\theta}_+ + J_2\dot{\theta}_3 \end{bmatrix},$$

where $H \equiv 1/2[m_w r^2(1+\rho^2) + 2\rho^2(J_1\cos{\theta_3}^2 + J_3\sin{\theta_3}^2)]$, $J_2 = m_3 d^2 + J_2'$ is the moment of inertia of the IB about $\mathcal{A}$, $M = 2m_w + m_3$ is the overall mass of the robot, $K \equiv m_3 rd/2$, and $\dot{\theta}_+ \equiv \dot{\theta}_1 + \dot{\theta}_2$. The nonholonomy term $\mathbf{H}^T\mathbf{p}$ is given by

$$\mathbf{H}^T\mathbf{p} = m_3 r\rho\dot{\theta}_- d\sin\theta_3 \begin{bmatrix} -\dot{\theta}_2 & \dot{\theta}_1 & 0 \end{bmatrix}, \tag{3.17}$$

which vanishes if any of the conditions below holds:

i) $\theta_3 = 0$ and/or

ii) $\dot{\theta}_1 = \dot{\theta}_2 \Rightarrow \dot{\theta}_- = 0$ and/or *iii)* $\dot{\theta}_1 = 0$ and $\dot{\theta}_2 = 0$.

Condition *i)* is respected when the robot is either stationary or turning about a vertical axis passing through C, and the axis contains C_3. Condition *ii)* is guaranteed when the robot performs a rectilinear motion because in this case the angular velocities of the robot wheels are identical. Condition *iii)* is satisfied when the robot is at rest. In this light the robot is QH in its two fundamental operation modes, namely, (*i*) travelling on a straight course and (*ii*) turning about a vertical axis passing through C. In order to guarantee the robot to be QH in general, the condition $\theta_3 \to 0$ can be imposed by means of control.

Granted, the robot can deviate from quasiholonomy, the purpose of the control scheme being to maintain quasiholonomy. Since quasiholonomy is possible by control, it is fair to call the robot under design *quasiholonomic.*

If we define $\boldsymbol{\tau} = [\ \tau_1 \quad \tau_2\ ]^T$ as the array of torques transmitted to the wheels by the actuators (wheel motors), eq. (3.2) becomes (Salerno and Angeles, 2005)

$$\mathbf{I}(\boldsymbol{\theta})\ddot{\boldsymbol{\theta}} + \mathbf{C}(\boldsymbol{\theta}, \dot{\boldsymbol{\theta}})\dot{\boldsymbol{\theta}} + \mathbf{g}(\boldsymbol{\theta}) = \boldsymbol{\xi}. \tag{3.18}$$

where $\boldsymbol{\xi} \equiv [\ \boldsymbol{\tau}^T \quad 0\ ]^T$, $\boldsymbol{\theta} \equiv [\ \theta_1 \quad \theta_2 \quad \theta_3\ ]^T$ and $\mathbf{g}(\boldsymbol{\theta}) = [0\ 0\ m_3 g(\sin\theta_3)d]^T$ represents the gravity term, while $\mathbf{I}(\boldsymbol{\theta})$ is the generalized inertia matrix, given by

$$\mathbf{I}(\boldsymbol{\theta}) = \begin{bmatrix} B + C^\star(\theta_3) & A - C^\star(\theta_3) & K\cos\theta_3 \\ A - C^\star(\theta_3) & B + C^\star(\theta_3) & K\cos\theta_3 \\ K\cos\theta_3 & K\cos\theta_3 & J_2 \end{bmatrix}$$

with $A \equiv [m_3 r^2 - 2m_w r^2 \rho^2]/4$ and $B \equiv [6m_w r^2 + m_3 r^2 + 2m_w r^2 \rho^2]/4$ and $C^\star(\theta_3) \equiv \rho^2(m_3 d^2 \sin^2\theta_3 + J_1 \cos{\theta_3}^2 + J_3 \sin{\theta_3}^2)$. Furthermore, the 3-dimensional vector of quadratic terms of inertia forces is given by

$$\mathbf{C}(\boldsymbol{\theta}, \dot{\boldsymbol{\theta}})\dot{\boldsymbol{\theta}} = \begin{bmatrix} -(m_3 d/2) r \sin\theta_3 \dot{\theta}_3^2 - G \\ -(m_3 d/2) r \sin\theta_3 \dot{\theta}_3^2 + G \\ -m_3 d\rho^2 \dot{\theta}_-^2 d \sin\theta_3 \cos\theta_3 \end{bmatrix},$$

where

$$G \equiv (m_3 d r \rho^2 \dot{\theta}_2 \dot{\theta}_- \sin\theta_3 + 2m_3 d\rho^2 \dot{\theta}_- d\dot{\theta}_3 \sin\theta_3 \cos\theta_3 + 2\sin\theta_3 \cos\theta_3 \rho^2 \dot{\theta}_- (J_3 - J_1)\dot{\theta}_3).$$

3.3 Controllability Analysis

As anticipated in Section 2.3, the main control tasks of the robot are: *i*) positioning and orienting the payload, supported by the IB, on a flat surface (primary task); and *ii*) suppressing the oscillations of the IB (secondary task). While apparently it is possible to accomplish the primary task using only the wheel motors, accomplishing the secondary task needs an in-depth controllability analysis.

Controllability is a key issue in the design and control of under-actuated robotic mechanical systems, since it allows the roboticist to verify whether the selected number and layout of actuators is sufficient to control the robot.

Quasimoro is under-actuated by design, since it has two control inputs, τ_1 and τ_2, but three independent generalized-velocities, as shown in Section 3.2. The main challenge to face here is the control of the motion of the IB, which will tend to rotate about the wheel axis as the wheels are actuated. We prove below that it is possible to completely control the robot using only the wheel motors, while following a desired path. To this end, we show that every linearization of the robot mathematical model around an equilibrium state verifies the Kalman rank condition for controllability (KRCC) (Chen, 1999). Therefore, Quasimoro is small-time locally controllable (STLC) from every equilibrium state. Moreover, applying the Lie-algebra rank condition (LARC) (De Luca and Oriolo, 1995), we show that Quasimoro is also locally accessible (LA) from any state other than those of equilibrium.

The IB oscillations being kinematically decoupled from the robot motion on $\mathcal{B}$, the IB is free to rotate about the wheel axis by means of ball bearings. Therefore, the kinematic model, described by eqs. (3.12), is not sufficient to completely control the robot without increasing the number of actuators.

The robot configuration is described in the joint space, the state vector thus being defined as

$$\mathbf{x} = [\ \theta_1 \quad \theta_2 \quad \theta_3 \quad \dot{\theta}_1 \quad \dot{\theta}_2 \quad \dot{\theta}_3\ ]^T, \tag{3.19}$$

In this light, the mathematical model of eq. (3.18), can be rewritten in the state-space form (Salerno and Angeles, 2005) $\dot{\mathbf{x}}(t) = \boldsymbol{\kappa}(\mathbf{x}(t), \boldsymbol{\tau}(t))$, with $\boldsymbol{\tau} = [\ \tau_1 \quad \tau_2\ ]^T$, $\boldsymbol{\kappa}(\mathbf{x}, \boldsymbol{\tau}) = \left[\ k_1 \ldots k_6\ \right]^T$, where $k_1 = x_4$, $k_2 = x_5$, $k_3 = x_6$, $k_5 = k_4 - [(\tau_1 + \tau_2 + Q_{50})/C_5]$, $k_6 = [D(\tau_1 + \tau_2) + Q]/C$, and

$$k_4 = \left[\sum_{i=0}^{3} Q_{4i} \cos^i x_3 + D_4(\tau_1 + \tau_2)\right] / C_4.$$

while x_i, for $i = 1, 2 \ldots 6$, is the i-th component of $\mathbf{x}$. Note that the foregoing differential equations are well-defined in the state space, since $C_4 \neq 0$, $C_5 \neq 0$ and $C \neq 0 \ \forall\, x_3$. Appendix A is included to provide further details.

Controllability from Equilibrium States

The set of equilibrium states $\mathcal{X}_e$ of the foregoing model is obtained by setting $\boldsymbol{\kappa}(\mathbf{x}, \boldsymbol{\tau}) = \mathbf{0}_6$, with $\boldsymbol{\tau} = \mathbf{0}_2$ (Nijmeijer and van der Schaft, 1990). Hence,

$$\mathcal{X}_e = \{\mathbf{x} = [\, x_1 \ \ x_2 \ \ x_3 \ \ x_4 \ \ x_5 \ \ x_6 \,]^T \ | x_3 = 0 \text{ or } \pi \ \text{ and } \ x_i = 0 \ \forall\, i \geq 4\}. \tag{3.20}$$

From the structure of the vector field $\boldsymbol{\kappa}(\mathbf{x}, \boldsymbol{\tau})$, it is apparent that every equilibrium state is equivalent to the others for controllability test purposes. Linearizing around a generic equilibrium state $\mathbf{x}_0 = [\ \bar{x}_1 \quad \bar{x}_2 \quad \bar{x}_3 \quad 0 \quad 0 \quad 0\ ]^T$, we obtain $\dot{\mathbf{x}} = \mathbf{A}\mathbf{x} + \mathbf{B}\boldsymbol{\tau}$, with[7]

$$\mathbf{A} = \left.\frac{\partial \boldsymbol{\kappa}}{\partial \mathbf{x}}\right|_{\mathbf{x}=\mathbf{x}_0} = \begin{bmatrix} \mathbf{O}_{32} & \mathbf{0}_3 & \mathbf{1}_3 \\ \mathbf{O}_{32} & \mathbf{a} & \mathbf{O}_{33} \end{bmatrix}, \quad \mathbf{B} = \left.\frac{\partial \boldsymbol{\kappa}}{\partial \boldsymbol{\tau}}\right|_{\mathbf{x}=\mathbf{x}_0} = \begin{bmatrix} \mathbf{0}_3 & \mathbf{0}_3 \\ \mathbf{b}_1 & \mathbf{b}_2 \end{bmatrix},$$

where

$$\mathbf{a} = \begin{bmatrix} -dgm_3K/F \\ -dgm_3K/F \\ \pm(A+B)m_3gd/F \end{bmatrix}, \mathbf{b}_1 = \begin{bmatrix} [\pm(K^2 - J_1\rho^2 J_2 - BJ_2) + TK]/E \\ [\pm(AJ_2 - J_1\rho^2 J_2 - K^2) + TK]/E \\ (\pm K + A + B)/F \end{bmatrix},$$

$$\mathbf{b}_2 = \begin{bmatrix} [\pm(AJ_2 - J_1\rho^2 J_2 - K^2) + TK]/E \\ [\pm(K^2 - J_1\rho^2 J_2 - BJ_2) + TK]/E \\ (\pm K + A + B)/F \end{bmatrix},$$

$+$ $(-)$ applying to the points of stable (unstable) equilibrium; $F = (2K^2 - (A+B)J_2)$; $E = [F(B-A) + 4J_1\rho^2K^2 - 2(A+B)J_2J_1\rho^2]$; and $T = A - 2\rho^2 J_1 - B$. The 6×12 controllability matrix is given by $\mathbf{C} = [\ \mathbf{B} \quad \mathbf{AB} \quad \mathbf{A}^2\mathbf{B} \quad \mathbf{A}^3\mathbf{B} \quad \mathbf{A}^4\mathbf{B} \quad \mathbf{A}^5\mathbf{B}\ ]$. After

[7] $\mathbf{A}$ is not to be confused with the constraint matrix $\mathbf{A}$ of Section 3.2.

rearrangement of its columns, this matrix includes a 6×6 block of zeros and a 6×6 block

$$\mathbf{C}' = \begin{bmatrix} \mathbf{0}_3 & \mathbf{0}_3 & \mathbf{b}_1 & \mathbf{b}_2 & \mathbf{0}_3 & (\mathbf{b}_2)_3\mathbf{a} \\ \mathbf{b}_1 & \mathbf{b}_2 & \mathbf{0}_3 & \mathbf{0}_3 & (\mathbf{b}_2)_3\mathbf{a} & \mathbf{0}_3 \end{bmatrix}$$

where we have indicated with $(\mathbf{b}_2)_3$ the third component of $\mathbf{b}_2$. The controllability condition can now be summarized in terms of the linear independence of the vectors $\mathbf{a}$, $\mathbf{b}_1$ and $\mathbf{b}_2$ plus the condition $(\mathbf{b}_2)_3 \neq 0$. It is thus apparent that the system becomes uncontrollable if its overall mass centre lies on the wheel axis, i.e. $d = 0$ in Fig. 2.4. In summary, $\mathbf{C}'$ is of rank 6 for every equilibrium state, and hence, the linearized system is controllable according to the KRCC.

A well-known theorem in control theory states that if the linearization of a nonlinear system at an equilibrium state is controllable, then the nonlinear system is STLC from the equilibrium state (Nijmeijer and van der Schaft, 1990). Hence,

Proposition 3.3.1. *Quasimoro is STLC from any equilibrium point.*

This proposition was also verified by the application of Sussmann's theorem to a simplified model of the robot, see (Salerno and Angeles, 2003a).

Controllability from Non-Equilibrium States

Although a general sufficient condition for a nonlinear system with drift to be STLC exists, it applies only to equilibrium states (Sussmann, 1987). Therefore, we limit ourselves to analyzing the non-equilibrium states in terms of local accessibility, which is the second-most-used structural characterization of a nonlinear system with regard to the natural form of controllability (De Luca and Oriolo, 1995). To this end, the mathematical model of the robot, described by eq. (3.18), can be rewritten in the affine state-space form

$$\dot{\mathbf{x}}(t) = \mathbf{f}(\mathbf{x}(t)) + \sum_{i=1}^{2} \mathbf{g}_i(\mathbf{x}(t))\tau_i(t), \tag{3.21}$$

with (Salerno and Angeles, 2005)

$$\mathbf{f} = \begin{bmatrix} x_4 \\ x_5 \\ x_6 \\ P_1/S_1 \\ P_2/S_2 \\ P_3/S_3 \end{bmatrix}, \quad \mathbf{g}_1 = \begin{bmatrix} 0 \\ 0 \\ 0 \\ A_1/C_1 \\ A_2/C_2 \\ A_3/C_3 \end{bmatrix}, \quad \text{and} \quad \mathbf{g}_2 = \begin{bmatrix} 0 \\ 0 \\ 0 \\ A_2/C_2 \\ A_1/C_1 \\ A_3/C_3 \end{bmatrix}.$$

with additional details provided in Appendix A.

The *distribution* defined by the vector fields $\mathbf{f}, \mathbf{g}_1$, and $\mathbf{g}_2$ is $\Delta_{\mathcal{A}} = \text{span}\{\mathbf{f}, \mathbf{g}_1, \mathbf{g}_2\}$. We now follow the procedure described in (De Luca and Oriolo, 1995) in order to compute the *involutive closure* of $\Delta_{\mathcal{A}}$, that will be indicated with $\overline{\Delta}_{\mathcal{A}}$. The first step is to compute the dimension of the first distribution Δ_1, defined as $\Delta_1 = \Delta_{\mathcal{A}} = \text{span}\{\mathbf{f}, \mathbf{g}_1, \mathbf{g}_2\}$. By looking at $\mathbf{f}$, $\mathbf{g}_1$, and $\mathbf{g}_2$ we infer that $\dim(\Delta_1) = 3 \; \forall \mathbf{x} \notin \mathcal{X}_e$. The next step consists in computing Δ_2, namely,

$$\Delta_2 = \Delta_1 + [\Delta_1, \Delta_1] = \text{span}\{\mathbf{f}, \mathbf{g}_1, \mathbf{g}_2, [\mathbf{f}, \mathbf{g}_1], [\mathbf{f}, \mathbf{g}_2], [\mathbf{g}_1, \mathbf{g}_2]\},$$

where, in the last simplification, we have applied the skew-commutativity property (Isidori, 1989). Computing the Lie brackets, we obtain that $[\mathbf{g}_1, \mathbf{g}_2] = \mathbf{0}_6$, whence $\Delta_2 = \text{span}\{\mathbf{f}, \mathbf{g}_1, \mathbf{g}_2, [\mathbf{f}, \mathbf{g}_1], [\mathbf{f}, \mathbf{g}_2]\}$ and $\dim(\Delta_2) = 5 \quad \forall \mathbf{x} \notin \mathcal{X}_e$. The distribution $\Delta_3 = \Delta_2 + [\Delta_1, \Delta_2]$ thus reduces to

$$\Delta_3 = \text{span}\{\mathbf{f}, \mathbf{g}_1, \mathbf{g}_2, [\mathbf{f}, \mathbf{g}_1], [\mathbf{f}, \mathbf{g}_2], [\mathbf{g}_1, [\mathbf{f}, \mathbf{g}_1]]\}$$

by applying the skew-commutativity property, the Jacobi identity (Isidori, 1989), and knowing that (*i*) $[\mathbf{g}_1, [\mathbf{f}, \mathbf{g}_1]] = [\mathbf{g}_2, [\mathbf{f}, \mathbf{g}_2]] = [\mathbf{g}_1, [\mathbf{f}, \mathbf{g}_2]] = [\mathbf{g}_2, [\mathbf{f}, \mathbf{g}_1]]$ and (*ii*)

$$[\mathbf{f}, [\mathbf{f}, \mathbf{g}_1]] = [\mathbf{f}, [\mathbf{f}, \mathbf{g}_2]] \in \text{span}\{\mathbf{f}, \mathbf{g}_1, \mathbf{g}_2, [\mathbf{f}, \mathbf{g}_1], [\mathbf{f}, \mathbf{g}_2], [\mathbf{g}_1, [\mathbf{f}, \mathbf{g}_1]]\}.$$

Using computer algebra, we show symbolically—by computing the rank of the matrix formed by the column vectors $\mathbf{f}, \mathbf{g}_1, \mathbf{g}_2, [\mathbf{f}, \mathbf{g}_1], [\mathbf{f}, \mathbf{g}_2]$, $[\mathbf{g}_1, [\mathbf{f}, \mathbf{g}_1]]$ and showing it to be six for *all* states—that $\dim(\Delta_3) = 6 \quad \forall \mathbf{x} \notin \mathcal{X}_e$, i.e.,

$$\overline{\Delta}_{\mathcal{A}} = \Delta_3 = \text{span}\{\mathbf{f}, \mathbf{g}_1, \mathbf{g}_2, [\mathbf{f}, \mathbf{g}_1], [\mathbf{f}, \mathbf{g}_2], [\mathbf{g}_1, [\mathbf{f}, \mathbf{g}_1]]\},$$

whence

Proposition 3.3.2. *Quasimoro is LA from any state different from equilibrium.*

Propositions 3.3.1 and 3.3.2 hold also for $\mathbf{x} = [\ \bar{\mathbf{c}}^T \quad \psi \quad \theta_3 \quad \dot{\bar{\mathbf{c}}}^T \quad \dot{\psi} \quad \dot{\theta}_3\ ]^T$.

3.4 Analysis of Robot Manoeuvres

We simulate the robot kinematic and dynamic behaviours in Matlab 6.5.199709 and Simulink 5.01 (R113SP1) (Cavallo et al., 1996). Primitives of motion of Quasimoro, such as rectilinear motion and rotation in place, are analyzed under the assumptions indicated at the beginning of Section 2.10. No feedback control strategy is considered at this stage: the simulation runs are performed in open-loop (Salerno et al., 2004a).

In every simulation the system is considered initially at rest. It is noteworthy that the simulation runs do not account for either external dissipation such as rolling friction between the wheels and ground, and for internal dissipation, such as friction in the bearings. Moreover, the inputs are represented by torque pulses, actuating the wheels, of duration of 1s applied at $t_0 = 1$s, in order to avoid problems in reading the output plots in the zone close to $t = 0$. Each simulation takes 90 s, but most of all the output plots are reported in the time window that goes from 0 s to 5 s, to better show the transient response.

Three manoeuvres have been implemented: *i*) rectilinear motion, while maintaining constant the orientation angle ψ, and *ii*) pure rotation, with $\theta_3(0) = 0$ rad, about the vertical axis passing through C, i.e. to vary only the orientation angle ψ, and not the position of the reference point C.

3.4.1 Rectilinear motion

In this simulation run, two equal torque pulses of amplitude of 0.3 Nm are applied to the wheels. The output plots are reported in Figs. 3.1a–3.1d.

As we can infer from Figs. 3.1a and 3.1b, θ_1 and θ_2 and their first derivatives are equal, since the load condition is symmetric. Moreover, by looking at Fig. 3.1b we

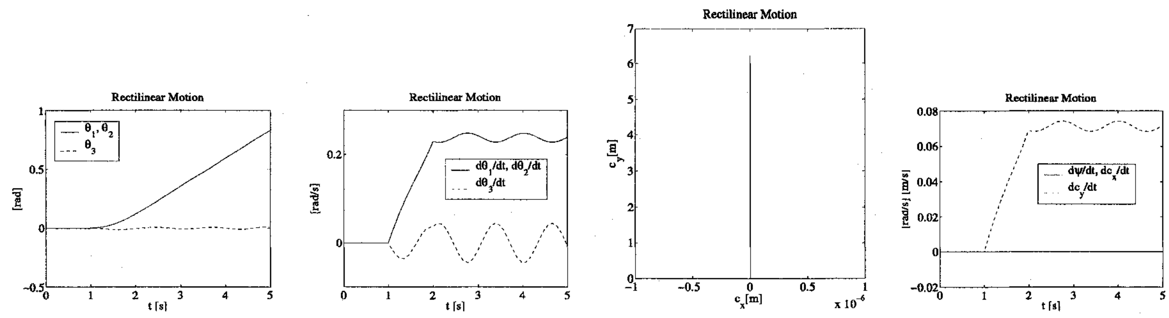

(a) (b) (c) (d)

Figure 3.1: Rectilinear Motion: (a) θ_i vs. t; (b) $\dot{\theta}_i$ vs. t; (c) path followed by point C; (d) $\dot{\psi}$, $\dot{c}_x$, $\dot{c}_y$ vs. t.

can argue that the two periodic signals $\dot{\theta}_1$ and $\dot{\theta}_2$ are both generated by $\dot{\theta}_3$, since each of them has the the same period of the latter.

From Fig. 3.1a, where θ_3 is represented by a periodic signal, we can infer that the oscillation of the intermediate body in the steady state is between $-0.5°$ and $0.5°$; of course, this oscillation needs no stabilization, since its amplitude is not big enough to be considered as a disturbance for the accomplishment of the stabilization task (see Section 1). However, $\theta_3(0)$ might not be zero because of assembly and manufacturing errors; moreover, the actual surface on which the robot moves can be indeed slightly inclined. Hence, it is necessary to stabilize this oscillation.

The rectilinear path is followed with a high accuracy, as indicated in Fig. 3.1c. Of course, the wheels never experience the same torque in reality. Moreover, because the velocity is not constant in the steady state, as displayed in Fig. 3.1d, the number of oscillations of the IB needs to be reduced.

3.4.2 Rotation

Two equal torque pulses of amplitude of 0.3 Nm, opposite in sign, are applied to the wheels. The output plots are displayed in Figs. 3.2a–3.2d.

The path followed by point C, not included here, reduces to a point coincident with the origin of the inertia frame; moreover, the angular velocity is constant in the steady state, as indicated in Fig. 3.2d. Anyway, for what has been already stated in

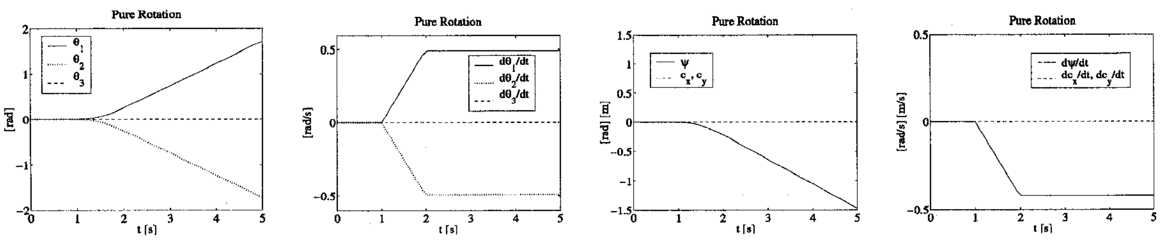

(a) (b) (c) (d)

Figure 3.2: Rotation: (a) θ_i vs. t; (b) $\dot{\theta}_i$ vs. t; (c) ψ, c_x, c_y; (d) $\dot{\psi}$, $\dot{c}_x$, $\dot{c}_y$ vs. t.

the previous Subsection about the errors affecting the construction of the robot, in reality the path followed by point C will not be a point.

For the assigned initial conditions and the type of input, the angle θ_3 and its first and second derivatives will remain equal to zero during the whole simulation, while θ_1, θ_2 and their first derivatives are equal in amplitude and opposite in sign, as indicated in Fig. 3.2a–3.2b.

These simulation runs are crucial for the prediction of the robot behaviour and the design of the system (Salerno and Angeles, 2003c).

Chapter 4

Embodiment and Detail Design

A good design has always played a crucial role for obtaining high-performance robotic mechanical systems (Siciliano and Dario, 2003). At the heart of every robotic system is a set of basic devices (actuation system, robot drive system, etc.). Early robotics researchers sometimes suggested that the design of these devices was not important because the robot control unit could compensate for design limitations. We now know that, in fact, devices such as the robot drive system are of primary importance. *Good* robotic devices can sometimes be controlled by rudimentary controllers, but poor devices generally cannot be adequately controlled by even the most sophisticated controllers (Bolles and Roth, 1988).

4.1 Introduction

As we have seen in Chapter 2, the mechanical design guidelines and specifications are mainly dictated by *i*) the constraints present in the environment where the robot operates, i.e. living quarters specifically designed for paraplegic WUs, and the limitations on the mobility of the user. Therefore, issues, such as doorway negotiation, access to the payload by the user, and ground clearance dictate the dimensions of the robot chassis.

Quasiholonomy is achieved by placing the MC of the robot on the vertical passing through the mid-point of the line segment defined by the wheel centres (Salerno and Angeles, 2004c). Stability is achieved by locating the MC of the robot below the wheel axis. In order to locate the MC of the robot on the vertical line passing through the mid-point of the line linking the wheel centers, the symmetry with respect to the aforementioned vertical is respected throughout the design process. Moreover, in order to locate the MC of the robot below the wheel axis, all the robot components, such as motors, power supply, electronic equipment, are brought as low as possible. Throughout the design process we try to follow the "keep it simple" design approach. Most of the robot parts are dimensioned according to standard stress analysis techniques (Juvinall and Marshek, 2006).

4.2 First Design Solution

The robot virtual prototypes (RVPs) have been designed using *PRO/Engineer V20* by *PTC* (Utz and Cox, 1997). Exploiting the techniques of virtual prototyping, several design solutions are derived in the foregoing computer-aided design (CAD) environment, thus strongly reducing the development costs (Salerno et al., 2004b).

The first RVP, depicted in Fig. 4.1a, consists of *i*) two custom-made wheels endowed with elastomeric O-ring belts that act as tires, *ii*) a custom-fabricated cage made of four aluminum alloy braces for guaranteeing the parallelism between the wheels, and *iii*) a bolted chassis.

The actuation system of the first RVP, rendered in Fig. 4.1a, consists of a DC permanent magnet brushed motor along with a three stage (74 : 1 ratio) PG directly coupled to a custom-made wheel based on O-ring technology.

4.2.1 Wheel Design

The wheel design of the first RVP consists of two custom-made components (18 and 19 of Fig. 4.1b), an elastomeric O-ring (15 of Fig. 4.1b) and three nut-bolt sets (7 and 13 of Fig, 4.1b). The O-ring plays the role of the wheel tire. The toroidal shape of the O-ring strongly reduces the rolling friction between wheel and ground, thus

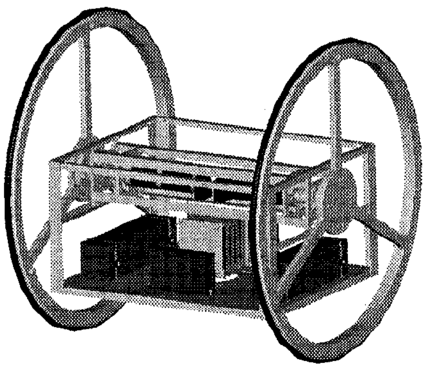

(a)

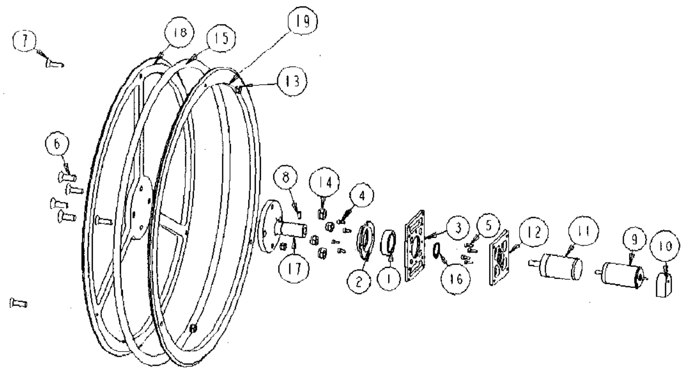

(b)

Figure 4.1: (a) First RVP; (b) first wheel sub-assembly

increasing the accuracy of robot positioning. The three nut-bolt sets are designed to ease the O-ring servicing.

One novel feature of this wheel design is the O-ring; elastomeric O-rings are intended to be used as seals, cushion installation, and low-power drive belt transmissions. Only once has an O-ring been used in a robotic wheel (Leow, 2002).

O-Ring Dimensioning

In selecting the O-ring we follow a procedure stemming from the integration of standard design methodologies for some mechanical systems, such as rotary seals (Parker Seals, 2001), drive belts (Fenner Drives, 2004) and band brakes (Juvinall and Marshek, 2006), whose dynamics resemble the one of our system.

The first step consists in determining the O-ring compound, as selected compound may have significant influence on the groove design. Polyurethane is chosen for its excellent wear resistance, high tensile strength and high elasticity in comparison with any other elastomer (Parker Seals, 2001). Moreover, the heat resistance (82°C) and cold flexibility (−40°C) are also high enough to safely use polyurethane in the environment in which the robot navigates. Polyester urethane is preferred to polyether urethane for its better resistance to water; in fact, wet floors and humid areas sometimes present in a living quarter might be harmful for the robot tires. Furthermore, polyurethane features also *i*) a chemical resistance to ozone and aging, and *ii*) excellent dynamic properties (Parker Seals, 2001). Such a compound selection complies also with the general requirements for elastomer drive belt materials (Parker Seals, 2001).

For the given application of the robot and the corresponding design specifications on *a*) ground clearance, *b*) position of the overall mass centre of the robot under full payload and *c*) door negotiation, the wheel radius is $r = 0.295\,\mathrm{m}$, as discussed in Chapter 2. This value represents the minimum desired dimension of the outer diameter (OD) of the O-ring, as installed in the groove. Off-the-shelf O-rings for sealing applications are discarded because of their small cross section (CS) diameter; in fact, the biggest CS diameter available is only 6.985×10^{-3}m, which does not guarantee a sufficient resistance to compression. Custom-made O-rings are discarded as well, since they are 20 times more expensive than those off-the-shelf. Therefore, we select O-rings for drive-belt applications; in particular we select a 95 Shore A durometer (the highest hardness available) O-ring of $3/4'' = 19.05 \times 10^{-3}\,\mathrm{m}$ of CS diameter (the biggest available) and $11.22'' = 284.99 \times 10^{-3}\,\mathrm{m}$ of length (Tampa Rubber & Gasket Co., Inc., 2005).

Groove Dimensioning

After having selected the O-ring, its groove needs to be designed. The design follows these guidelines *i*) under minimum payload, there should be at least $0.2 \times 10^{-3}\,\mathrm{m}$ of radial compression of the tire cross section; by doing so the O-ring will not quickly take a 100% compression set[1]; and *ii*) the groove should accommodate an internal diameter (ID) stretch of the O-ring (as installed in the groove) of 5%. This percentage is chosen so as *a*) to have the running and break-out friction O-ring/groove as high as possible and *b*) not to shorten the life of the O-ring. The percent reduction in cross section diameter of the O-ring corresponding to the 5% ID stretch, turns out to be 2.41% (Parker Seals, 2001).

[1] "The compression set is the amout by which a rubber specimen fails to return to original shape after release of compressive load" (Parker Seals, 2001).

Finally, the groove is also designed so as to guarantee that the ID expansion needed to reach the groove during assembly does not exceed 50% of the ultimate elongation of the polyurethane (Parker Seals, 2001).

4.2.2 Actuation System Dimensioning

The Quasimoro actuation system consists of two identical units; each of them endowed with *i*) a Maxon RE 40 (148867) brushed motor (9 in Fig. 4.1b), equipped with a PG, namely, a Maxon GP 42 C (203123) (11 in Fig. 4.1b) . The PG is secured to the motor mount (12 of Fig. 4.1b) by means of four screws (5 of Fig. 4.1b). A rolling bearing (1 in Fig. 4.1b) and a custom-made wheel hub (11 in Fig. 4.1b) are added in order to reduce the bending moment of the planetary gearhead output shaft of 30%, approximately. The bearing is mounted on a custom-made housing (2 of Fig. 4.1b), which is fastened to a custom-made plate (3 of Fig. 4.1b) by means of four screws (4 of Fig. 4.1b). A snap ring (16 of Fig. 4.1b) prevents the bearing from axial motion along the wheel-hub. The driving torque is transmitted to the wheel by means of four nut-bolt sets (6 and 14 of Fig. 4.1b), while the wheel-hub is connected to the PG by means of a set screw (8 of Fig. 4.1b). A snapshot of the overall motor mount assembly is given in Fig. 4.2a.

In order to guarantee the wheel rolling under any payload condition, the torque applied to the wheel cannot be higher than $\tau_f = \mu_s Mr/2s = 10.7\,\text{Nm}$, where $M = 227.003\text{N}$ is the overall weight of the robot under minimum payload, $\mu_s = 0.4$ is the sliding friction coefficient of rubber (wheel tire) on rubber (floor) (Frederikse and Lide, 1996), $r = 0.295\,\text{m}$ is the wheel radius, while $s = 1.25$ is a safety factor.

In order to dimension the actuation system a series of simulation runs in Matlab 6.5.1.199709 and Simulink 5.1 (R13SP1) using the variable-step solver ODE45 (Dormand-Prince) is conducted. The assumptions made for the simulated model are the same of those made in Section 2.10, except one: robot moving on a horizontal surface. For the first RVP, the values of the geometric and inertial parameters of the robot, calculated for a minimum (i.e. no payload) and a maximum payload are displayed in

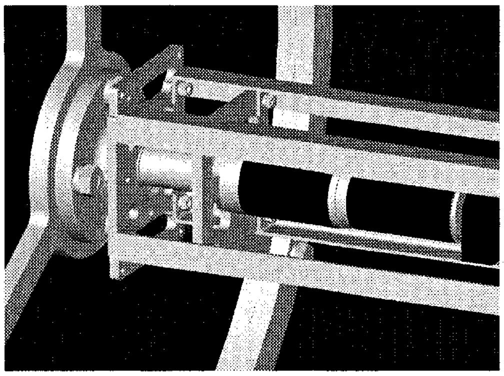

(a)

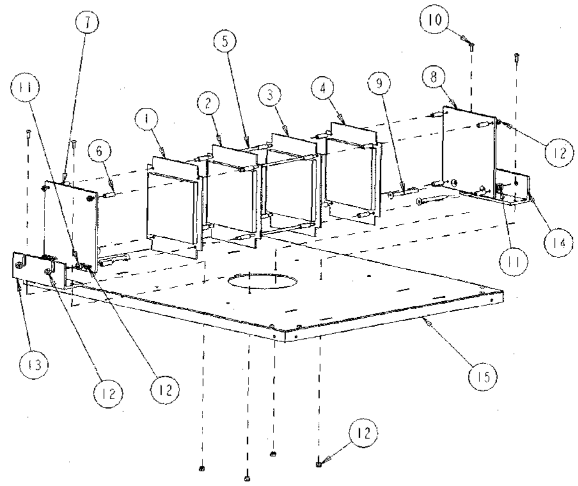

(b)

Figure 4.2: First RVP (a) motor mount close-up; (b) control unit exploded view

Payload	J_1, J_2 [kg m^2]	m, m_3 [kg]	d, r, l [m]
Minimum	0.591, 0.628	3.459, 16.222	0.120, 0.295, 0.480
Maximum	0.725, 0.918	3.459, 23.222	0.030, 0.295, 0.480

Table 4.1: Geometric and inertial parameters—first RVP

Table 4.1.

Both the forward dynamics and the forward kinematics of the robot are simulated (Salerno et al., 2004b); the desired profiles of the driving (v) and steering (ω) velocities of the robot used in simulation are 40s-period square waves of 2.00 m/s and 3.33rad/s peak-to-peak amplitude, respectively. The mathematical model used in the simulation runs relies on that described in Section 3.2. The simulated robot manoeuvres are intended to strongly excite the robot dynamics, see Table 4.2. In this Table, $\theta_3(0)$ is the value of the tilt angle of the intermediate body at time zero, P_M is the maximum power consumption observed in simulation, n_M is the maximum absolute value of the angular velocity of the wheel, τ_M is the maximum absolute value of the torque applied to the wheel, τ_{rms} is the root mean square (RMS) torque applied to the wheel, R1...R11 refer to the rectilinear motion, C1...C4 refer to the circular motion, and RT1...RT2 refer to the rotation.

Manoeuvre	$\theta_3(0)$[°]	P_M[W]	n_M[rad/s]	τ_{rms}[Nm]	payload	slope
R1	−90°	70.62	8.18	3.87	max	0%
R2	90°	73.49	8.42	3.87	max	0%
R3	90°	67.92	7.09	3.25	min	0%
R4	−90°	67.92	6.78	3.26	min	0%
R5	−90°	54.29	8.00	3.56	min	5%
R6	−90°	54.23	8.18	4.04	max	5%
R7	90°	54.67	8.00	3.67	min	5%
R8	90°	62.47	8.28	4.04	max	5%
R9	−90°	98.59	11.48	8.01	min	20%
R10	−90°	112.16	11.76	7.86	max	20%
R11	90°	100.68	11.51	7.99	min	20%
R12	**90°**	**112.28**	**11.76**	**8.01**	max	**20%**
C1	90°	95.76	9.53	4.10	max	0%
C2	−90°	95.30	9.53	4.15	max	0%
C3	90°	94.64	9.63	4.68	min	0%
C4	−90°	98.49	9.85	5.34	min	0%
RT1	90°	28.05	2.80	3.26	min	0%
RT2	−90°	27.11	2.74	2.13	max	0%

Table 4.2: Simulated manoeuvres for actuation system dimensioning

Planetary Gearhead and Motor Selection

As indicated in Table 4.2, the manoeuvre R12 features the highest values of P_M, n_M and τ_{rms}, which are used as reference in the actuation system dimensioning. In this light, one needs a speed reducer with a maximum continuous torque of at least $\tau_{rms} = 8.008\,\text{Nm}$ and an intermittent torque of at least $\tau_{max} = 10.00\text{Nm}$. These requirements are fulfilled by a PG with 42.00×10^{-3}m of chassis diameter (ceramic version) by Maxon Precision Motors, Inc. (2003). Knowing the maximum recommended input speed $n_{max,rec,in} = 8000.00\,\text{rpm} = 840\,\text{rad/s}$ (Maxon Precision Motors, Inc., 2003) of the PG and knowing the operating speed of the wheel

$$n_{op} = \frac{v}{r} = 6.780\,\text{rad/s} \approx 64.74\text{rpm},$$

one can easily compute the maximum reduction ratio $\varepsilon_{max} = n_{max,rec,in}/n_{op} = 123.57$. One selects the three-stage PG that features the next smallest reduction ratio of $\varepsilon = 338/3$ having a maximum efficiency of $\eta = 0.72$.

Motor series	τ_{cont} [Nm]	τ_{stall} [Nm]
Maxon RE 40, 150.00 W	2.01×10^{-1}	2.50
Maxon RE 35, 90.00 W	1.13×10^{-1}	1.07

Table 4.3: Motor selection—step one

Let us calculate speed and torque at the motor shaft: $n_{op,m} = \varepsilon n_{op} = 7.659 \times 10^2$ rad/s, $\tau_{rms,m} = \tau_{rms}/(\varepsilon\eta) = 9.90 \times 10^{-2}$ Nm and $\tau_{max,m} = \tau_{max}/(\varepsilon\eta) = 1.24 \times 10^{-1}$ Nm. The $\tau_{rms,m}$ value must be smaller than the motor continuous torque τ_{cont}, in order to prevent the motor from overheating. Moreover, the stall torque τ_{stall} of the selected motor should usually exceed the required peak torque, τ_{max}. Furthermore, for the reasons outlined in Chapter 2, our motor choice is DC brushed; now, once we select the PG Maxon GP 42 C (203126) (Maxon Precision Motors, Inc., 2003), we are bound to select one of the two DC brushed motors of Table 4.3. The abovementioned motors feature graphite brushes, which are better suited than precious metal ones for start/stop operations. Selection falls on the RE35 90.00 W motor, whose τ_{cont} is high enough. After having selected the motor series one needs to select the motor winding. The no-load speed target must be achieved with the maximum voltage $U = 33.6$ V supplied by the battery (see Subsection 4.2.3), the voltage drop over the PA being negligible (see Subsection 4.6.2); U defines the minimum speed-target constant, which is given by

$$K_{n,theor} = n_{0,theor}/U = 42.56 \,\text{rad/sV}. \tag{4.1}$$

Based on this calculation, motor 118776 (Maxon Precision Motors, Inc., 2003) may be chosen, which corresponds to the winding with the next highest speed constant (51.55 rad/sV) and has a second shaft end for mounting the encoder; however, the motor selection process stops because the 118776 motor has $\tau_{cont} = 7.80 \times 10^{-2}$ Nm, which is smaller than the RMS torque $\tau_{rms,m} = 9.90 \times 10^{-2}$ Nm. Therefore, the selection process restarts from the motor series choice.

By selecting the RE40 150.00 W series (Maxon Precision Motors, Inc., 2003) we have:

$$\left.\frac{\Delta n}{\Delta \tau}\right|_{av} = 0.42 \times 10^{-3}\,\mathrm{rad/sNm},$$

while the desired no-load speed can be easily computed as (Maxon Precision Motors, Inc., 2003):

$$n_{0,theor} = 1.375 \times 10^{3}\,\mathrm{rad/s}$$

and (4.1) becomes

$$K_{n,theor} = 40.93\,\mathrm{rad/sV}.$$

We may select the motor of 148866 winding (Maxon Precision Motors, Inc., 2003), which satisfies: $\tau_{max,m} < \tau_{stall}$. However, in order to avoid overheating of the motor windings and consequent permanent damages to the motor (U being twice the nominal voltage of the motor), the RE40 150.00 W 148866 is discarded as well. Therefore, the actuation system dimensioning process needs to be restarted from the PG selection step. The PG of the Maxon GP 42 C series with the next smallest reduction ratio is selected; it is a two-stage PG with the same efficiency as the previous one, but with $\varepsilon = 74$ (model 203123). In this light we have: $n_{op,m} = 4.996 \times 10^{2}\,\mathrm{rad/s}$, $\tau_{rms,m} = 1.51 \times 10^{-1}\,\mathrm{Nm}$ and $\tau_{max,m} = 1.90 \times 10^{-1}\,\mathrm{Nm}$. From these values, we are bound to select the RE40 motor series. As far as the motor winding is concerned we have: $n_{M,m} = 8.667 \times 10^{2}\,\mathrm{rad/s}$, $n_{0,theor} = 9.380 \times 10^{2}\,\mathrm{rad/s}$ and $K_{n,theor} = 27.92\,\mathrm{rad/sV}$. We can then select the motor with winding 148867, which has the next highest speed constant (33.28 rad/sV). Hence, the exact value of speed-torque gradient is (Maxon Precision Motors, Inc., 2003)

$$\frac{\Delta n}{\Delta \tau} = 0.315 \times 10^{-3}\,\mathrm{rad/sNm},$$

while

$$n_{0,theor} = n_{M,m} + \frac{\Delta n}{\Delta \tau}\tau_{max,m} = 9.329 \times 10^{2}\,\mathrm{rad/s}$$

and

$$K_{n,theor} = n_{0,theor}/U = 27.76\,\mathrm{rad/sV}.$$

The actual value of the speed constant (33.28 rad/sV) being higher than the latter, the motor runs faster than required which, however, can be compensated by the controller. This selection ensures also that there is a speed regulating reserve of more than 15%. Thus, even unfavorable manufacturing tolerances of the PG-motor system do not pose any problem. It is easy to verify that the operating point of the robot is contained in the recommended operating range of the motor at hand (Maxon Precision Motors, Inc., 2003).

The selected motor meets also the power requirements estimated in simulation. As a matter of fact, the power rating, i.e. 150 W, is higher than the maximum power calculated by simulation, i.e. 112.28 W, see Table 4.2.

4.2.3 Power Amplifier and Battery Dimensioning

Knowing the torque constant of the selected motor, $K_t = 0.030\,\mathrm{Nm/A}$ (Maxon Precision Motors, Inc., 2003), the desired maximum continuous current and the desired peak current are $i_{cont} = \tau_{rms,m}/K_t = 5.01\,\mathrm{A}$ and $i_{peak} = \tau_{max,m}/K_t = 6.28\,\mathrm{A}$, respectively. Both i_{cont} and i_{peak} suggest the selection of the 25A8 series of pulse-width modulation (PWM) power amplifiers for brushed motors (Advanced Motion Controls, 2004c), which features a maximum (internally limited) continuous current of 12 A and a peak current (lasting 2 s maximum and internally limited) of 25 A.

In order to verify the proper dimensioning of the PAs, few calculations need to be performed. The PA self-shutdown voltage $V_{ss} = 80\,\mathrm{V}$ should be greater than the maximum motor terminal voltage $V_{m,max}$, which can be calculated from the following equation, neglecting the voltage drop across the motor winding resistance,

$$V_{m,max} = I_m R_m + E \approx E = K_n n_{m,max} = 17.25\,\mathrm{V} < V_{ss} = 80\,\mathrm{V}$$

where I_m is the motor current, R_m is the motor winding resistance, E is the back-EMF voltage, $K_n = 3.312 \times 10^{-4}\,\mathrm{sV/rad}$ (Maxon Precision Motors, Inc., 2003) is the motor speed constant, and $n_m = 5.741 \times 10^{2}\,\mathrm{rad/s}$ is the maximum motor speed (estimated from simulation results)[2].

Battery Design: Selection and Service Life

It is recommended to dimension the robot battery nominal voltage to be 10%-50% greater than the maximum required voltage for the application. This percentage is to account for the over-time variations of the torque constant K_τ, the speed constant K_n and of the losses in control unit and PAs. Additionally, the battery nominal voltage should be at least 10% below the lowest value of the following: *i*) shunt regulator voltage (if present); and *ii*) PA self-shutdown voltage. In this regard, the Quasimoro battery is properly dimensioned by respecting all the above-mentioned design constraints. Furthermore, the internal resistance of the battery, $R_{in,batt}$, should be much smaller than the internal resistance of the PA, $R_{in,PA}$, in order to avoid circuit loading (Horowitz and Hill, 1989). To this end, Quasimoro's design satisfies the inequality: $R_{in,PA} = 50\,\mathrm{k}\Omega >> R_{in,batt} = 0.084\,\Omega$.

In motion-control applications, two important factors have to be taken into account when dimensioning the battery: the internal resistance and the nominal voltage. Quasimoro is powered by two Nickel-metal Hydride battery packs arranged in series; each pack has 14 *Sanyo Twicell HR-D* cells. Each cell is a HR-D 7.500 Ah (Sanyo Group, 2004). The latter is preferred to the 7.300 Ah and to the 9.000 Ah because of the smaller internal resistance (3mΩ < 5mΩ). This set-up is characterized by a nominal voltage $V_{nom} = 33.6\,\mathrm{V}$ and $R_{in,batt} = 0.084\,\Omega$ (Sanyo Group, 2004), which is low enough not to hamper the robot controller performance (Salerno and Angeles, 2004b). The nominal voltage is selected as 1.4 times the nominal voltage of the motor for a better exploitation of the actuator.

During deceleration or downward motion, the mechanical energy (kinetic and potential) of Quasimoro is regenerated via the power amplifier back onto the battery. This process is called regenerative breaking (RB), and charges the battery without

[2]It is noteworthy that the foregoing inequality is satisfied even by taking into account the maximum permissible speed of the motor $n_{max,perm} = 861\,\mathrm{rad/s}$: $V_{m,max} \approx E = K_n n_{max,perm} = 25.87\,\mathrm{V} < V_{ss} = 80\,\mathrm{V}$.

reaching potentially dangerous voltages or voltages that may cause an amplifier over-voltage shutdown. This condition is obtained by properly dimensioning the Quasimoro battery. In order to dimension the battery so as to avoid potentially dangerous recharge currents during RB, we refer to the following worst case scenario: robot decelerating while performing a downward motion such that both potential and kinetic energies are converted into electrical. We also use the conservative assumption of neglecting the dissipative forces. Under these assumptions we estimate a recharge current during RB that is within the limit recommended by the battery pack manufacturer ($7.478\,\mathrm{A} < 7.5\,\mathrm{A}$). Moreover, also the maximum final voltage at the end of the RB is within the limit recommended by the battery pack manufacturer ($39.2\,\mathrm{V} \leq 42.0\,\mathrm{V}$)[3].

The foregoing battery design guarantees a safe RB only for this version of Quasimoro. Future versions of Quasimoro that will consider applications different from wheelchair-user augmentation might require the use of additional components such as a set of capacitors (for storing RB energy in excess) or a shunt regulator.

In order to estimate the service life of Quasimoro battery packs we can determine the approximate performance, in service hours, by using nomographs (Linden, 2002).

The maximum power consumption of Quasimoro control unit power supply can be estimated by adding the maximum power dissipation (13 W) to the nominal output power (50 W), thus obtaining: $P_{control-unit,max} = 50\,\mathrm{W}$ (RTD Embedded Technologies, 2003). Being the minimum operating voltage of Quasimoro battery packs $V_{min,batt} = 30.8$ one can estimate the maximum average input current of Quasimoro control unit power supply as follows

$$I_{max,average,control-unit} = P_{control-unit,max}/V_{min,batt} = 2.045\,\mathrm{A}.$$

Knowing the maximum continuous current of Quasimoro motors $I_{max,cont,motor} = 6\,\mathrm{A}$ (Maxon Precision Motor, Inc., 2002) we have that the maximum average output current of Quasimoro battery packs is $I = I_{max,average,control-unit} + 2I_{max,cont,motor} =$

[3] `http://www.battlepack.com/`

14.045 A.

The robot battery weight is given by $m_{batt} = 4.9\,\text{kg}$ (Sanyo Group, 2004). Hence, by entering the nomograph of Fig. 29.8 of (Linden, 2002) with $I/m_{batt} = 2.866\,\text{A/kg}$ we have that Quasimoro has a minimum autonomy of 10 hours.

4.2.4 Robot Drive System

In order to align the wheel axes a cage made of four custom-fabricated aluminum alloy braces is designed, as shown in Fig. 4.3a. This solution would guarantee the parallelism of the wheels with a corresponding benefit to the positioning accuracy of the robot.

Extra-support Bearing

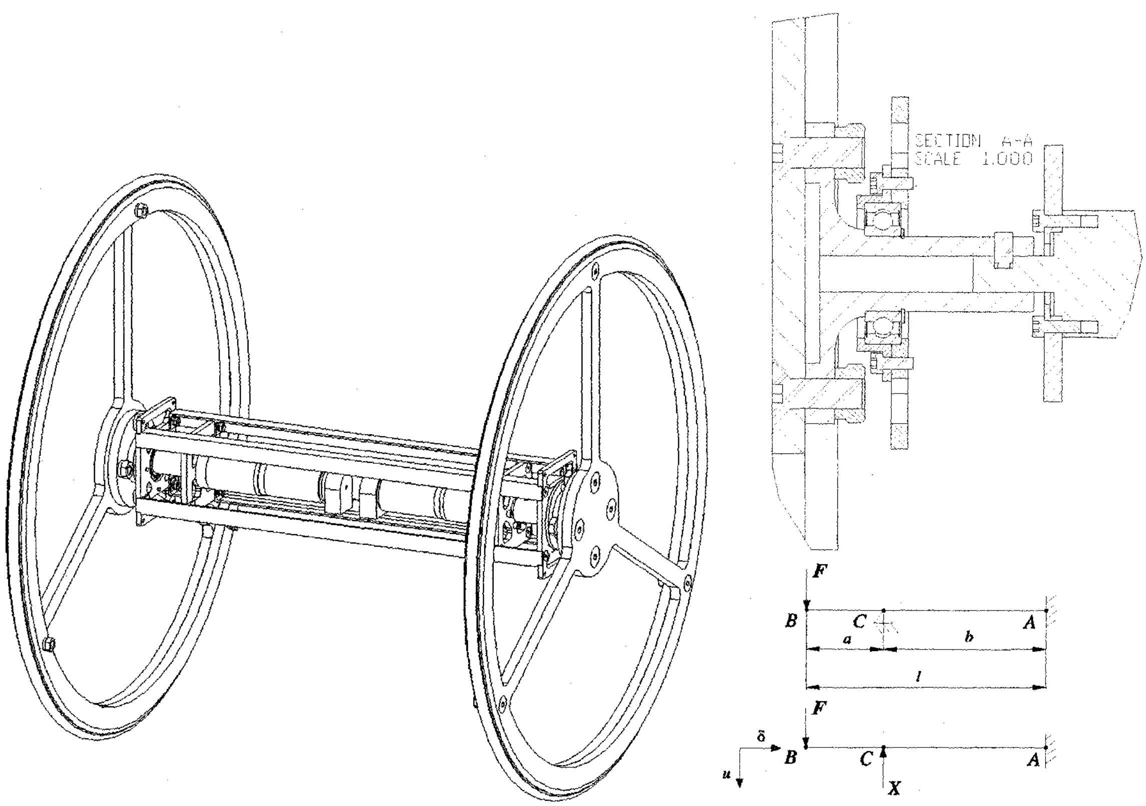

(a) (b)

Figure 4.3: First RVP (a) drive system; (b) extra-bearing modelling for stress analysis

Extra support to the PG output shaft, which actuates the wheel, is needed if the radial load acting on the PG output shaft exceeds the maximum permissible value indicated by the PG manufacturer. More specifically, with reference to the GP 42 C PG of Quasimoro, the maximum permissible radial load, computed 12×10^{-3} m from the PG flange, is $F_p = 150$ N (Maxon Precision Motors, Inc., 2003). It is noteworthy that the maximum permissible radial load of a PG increases with the radial dimensions of the internal bearings of the PG (that increase the overall dimensions of the PG). The radial load acting on the output shaft of each PG of the first RVP, without any extra-bearing, is given by a force F. The latter is half the overall weight of the robot without considering the wheel. As we shall see in eq. (4.4), $F = 114.136$ N, hence $F < F_p$. However, the radial load F should also be less than or equal to 50% of the maximum permissible load (150 N) in order to account also for humps and bumps. Therefore, an extra-support bearing needs to be installed between the wheel and the PG because $F > F_p/2$. In Fig. 4.3b we represent the design solution with extra-support bearing along with a schematics for stress analysis. The clamp constraint represents the double bearing of the planetary gearhead (Maxon Precision Motors, Inc., 2003). The support indicates the single extra-support bearing. The load is equal to half the weight of the robot. It is also assumed that the two different shafts (one of the planetary gearhead and the other of the wheel hub) have same material and cross-section.

As described above, an extra-support bearing needs to be used for limiting the radial load acting on the output shaft of the gearhead. In order to bring the value to specifications, an extra-support bearing is added as far as possible from the flange of the PG—see Fig. 4.3b—as shown presently.

Reaction Forces F is the shear force acting at the tip of the beam in Fig. 4.3b, whence the values below for the horizontal and vertical displacements, are obtained:

$$\delta_C = 0 \quad u_C = 0, \tag{4.2}$$

in which $\delta_C = X_1 b/EA_{cs}$, with A_{cs} denoting the cross-section area, E the Young modulus of the output shaft of the PG, and X_1 the horizontal reaction at A. From the first of eqs. (4.2) we have $\delta_C = X_1 b/EA_{cs} = 0 \Rightarrow X_1 = 0$. Moreover, the contribution of the force F to the vertical displacement of section C is given by (Viola, 1985)

$$u_C^F = \frac{Fa^3}{6EI} - \frac{Fl^2 a}{2EI} + \frac{Fl^3}{3EI}$$

where $I = \pi r^4/4$ and r is the radius of the PG output shaft, while that of the reaction X is

$$u_C^X = -\frac{Xb^3}{3EI}$$

Therefore, applying the principle of superposition (Juvinall and Marshek, 2006), we have

$$u_C = u_C^F + u_C^X = \frac{Fa^3}{6EI} - \frac{Fl^2 a}{2EI} + \frac{Fl^3}{3EI} - \frac{Xb^3}{3EI}.$$

From the second of eqs. (4.2) we have

$$\frac{Fa^3}{6EI} - \frac{Fl^2 a}{2EI} + \frac{Fl^3}{3EI} - \frac{Xb^3}{3EI} = 0,$$

which leads to

$$X = \left(\frac{Fa^3}{6EI} - \frac{Fl^2 a}{2EI} + \frac{Fl^3}{3EI}\right)\frac{3EI}{b^3} = \frac{3F}{b^3}\left(\frac{a^3 - 3l^2 a + 2l^3}{2}\right). \tag{4.3}$$

By plotting the foregoing vs. a, one can readily observe that the extra-bearing should be installed as close as possible to F.

Radial Load of the PG Output Shaft Due to the extra-support bearings, the radial load is contained within the value specified by the PG manufacturer. This is verified by means of *i*) a static stress analysis and *ii*) a dynamic stress analysis.

The maximum static radial load force acting at section B is given by

$$F_{st,max} = \frac{M + m_p}{2} = 114.136\,\mathrm{N} \tag{4.4}$$

where $M = 154.722\,\mathrm{N}$ and $m_p = 73.550\,\mathrm{N}$ are the robot weight (without taking into account the weight of the wheel units) and the payload weight, respectively. Hence, with $a = 27 \times 10^{-3}$ m, $l = 86 \times 10^{-3}$ m and $b = l - a = 59 \times 10^{-3}$ m, eq. (4.3) yields

$$X = 1.686 F_{st,max}.$$

Moreover, with $X = R_C$ (R_C being the reaction force at section C), one can compute the reaction force R_A at section A as follows (equilibrium of the vertical forces):

$$R_A = R_C - F_{st,max} = 0.686 F_{st,max} = 78.135\,\mathrm{N} < F_p = 150\,\mathrm{N}. \tag{4.5}$$

In order to verify the resistance to impact of the robot wheel, the following calculations need to be carried out. Using a safety factor of $k = 1.85$, the impact force acting at section B is given by

$$F_{impact,max} = k F_{st,max} = 216.4\,\mathrm{N}.$$

Hence, we have:

$$R_{A,impact} = 0.686 F_{impact,max} = 148.45\,\mathrm{N} < F_p = 150\,\mathrm{N}. \tag{4.6}$$

In this light, the presence of extra-support bearings diminishes *i*) the radial load by more than 30% (see eqs. (4.5) and (4.6)); and *ii*) the radial load is almost 50% of the maximum permissible radial load (see eq. (4.5)), thus accounting for humps and bumps as well.

4.3 Second Design Solution

In order to lower the overall mass centre of the robot, to limit the width of the robot and to contain the bending moment of the PG output shaft (without having to resort to an extra-support bearing), the use of a timing belt transmission is considered. Moreover, in order to reduce the manufacturing costs a commercial bicycle wheel is chosen, as opposed to its custom-made counterpart.

These design corrections affect mainly the robot drive system (RDS). However, before discussing how the RDS is redesigned we shall dwell on some design issues encountered when deriving this second solution.

Which commercial wheel?

An intense brain-storming session has led us to select a commercial bicycle wheel. However, several wheel design solutions have been considered before making the final decision.

Given the application of Quasimoro, we attempt to use the $24'' = 609.6 \times 10^{-3}\,\mathrm{m}$ *Economy Wheel*, with a standard round profile urethane snap-on tire, by *Skyway*, which represents a low cost alternative to the commercial $24'' = 609.6 \times 10^{-3}\,\mathrm{m}$ wheelchair alternative designed for the home health-care market (Skyway Machine, Inc., 2002). Unfortunately, *Skyway* provides a metal keyway hub only for wheels that are not larger than $20'' = 508 \times 10^{-3}\,\mathrm{m}$; the $24'' = 609.6 \times 10^{-3}\,\mathrm{m}$ wheels have a metal hub that is not suitable for hosting a keyway. Therefore, although the foregoing composite wheel by *Skyway* respects our specifications, the interfacing with a custom-made hub would be rather complicated and expensive, as opposed to the use of a bicycle wheel. Therefore, the outcome of this step is the choice of bycicle wheels.

Wheel hub motors?

In order to fully exploit the commercial bicycle wheel solution, the conceptual design of a drive system featuring the *Heinzmann* hub-motor (Heinzmann GmbH, 2004), one of the most successful actuators for electrical bicycles, is attempted. Using these motors would allow us to drastically reduce the overall dimensions of the robot actuation system (particularly the longitudinal dimensions) and, correspondingly, to better exploit the interior part of the robot chassis. However, we discard the *Heinzmann* hub-motor solution because *i*) it is at least twice as expensive as the Maxon motor solution of Subsection 4.2.2, *ii*) no encoder can be readily custom-fitted to sense the position of the wheel shaft, and *iii*) the integral gearbox is a simple gear train made of two mating spur gears, which are not recommended for Quasimoro, as anticipated in Chapter 2.

Why timing belts?

In order to prevent the PG from failing upon impact between the wheel and obstacles, a TS that would decouple the driving torque from the bending moment of the PG output shaft is designed. Although chains are generally, under the same transmission conditions, much cheaper than timing belts, a chain transmission is discarded for various reasons (Kanehira et al., 2005): *i*) a chain is more suitable for long-term continuous running and power transmission with limited torque fluctuation; and *ii*) it produces undesirable speed variations stemming from the chordal action phenomenon.

Although suitable for applications like ours, which require precise positioning accuracy and repeatability, metal timing steel belts are discarded for the design complications introduced by the belt camber phenomenon[4]. Belt camber is the deviation of a belt edge from a straight line; for our application the estimated camber is approximately 2×10^{-3} m. To cope with this issue, one should resort to independently steerable pulleys, which represents a sophistication that goes against the "keep it simple" approach.

A timing belt TS, see Fig. 4.15b in Section 4.7, is selected because (SDP/SI Inc., 1991): *i*) backlash between pulley and belt teeth is negligible with respect to that of a friction belt system; *ii*) timing belts do not require lubrication; and *iii*) timing belts do not slip and there is no relative motion between two elements in mesh. Timing belt TSs feature also the following advantages: *i*) maintenance is minimal and infrequent, *ii*) operation is quiet and smooth, *iii*) sudden shocks and changes in load are dampened. Some limitations of timing belts are the following: *i*) their length cannot be adjusted, *ii*) adverse service environments (extreme temperature ranges, high moisture, oily or chemically filled atmospheres) can damage belts and cause severe slipping. However, all these limitations do no apply to Quasimoro design and application.

Hence, a second RVP of Quasimoro is devised, see Fig. 4.4a[5].

---

[4]`http://www.belttechnologies.com`

[5]The timing belt is purposefully omitted in order to better show the transmission mechanism.

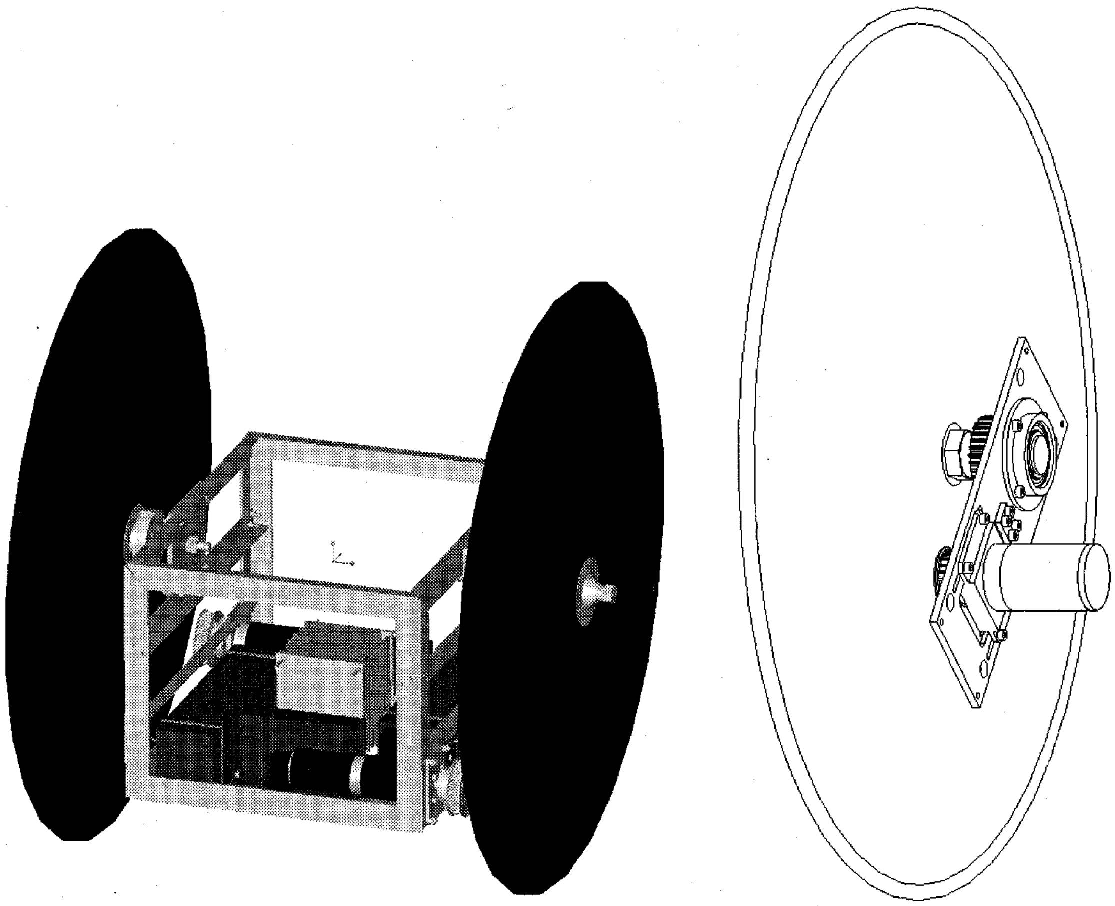

(a) (b)

Figure 4.4: (a) Second RVP; (b) second wheel sub-assembly

Robot Drive System Design

The design of Fig. 4.4a does not allow for the regulation of the timing belt tension. To this end the RDS is redesigned. The novel RDS is characterized by a bicycle wheel tightened to a custom-made shaft by means of a frictional connector; the timing belt takes care of the mechanical power transmission from the output shaft of the PG to the custom-made shaft, as depicted in Fig. 4.4b. Such a solution allows for redundant sensing, since motion sensors can be readily assembled on the custom-made shaft 2 of Fig. 4.5a. In this Figure, we indicate with 1 the two frictional *Shaftlocks*$^{\mathrm{TM}}$ which fasten the bicycle wheel 6 to shaft 2. Note that we take away the bicycle wheel hub and bearings. We are only using the wheel rim and tire. With 4, we indicate a ball bearing that allows shaft 2 to rotate with respect to the robot chassis, on which plate 10 is to be mounted. The actuation system, of which we report only the PG 5, is housed in motor mount 9, which is itself fastened to plate 10. The motion is transmitted from the driving pulley 8—fastened to PG 5 by means of a key and two set screws, not displayed here—to the driven pulley, which is mounted on shaft 2 by means of a key (two spacers will prevent the pulley from moving axially); device 3 is intended to re-tighten the timing belt, not displayed here.

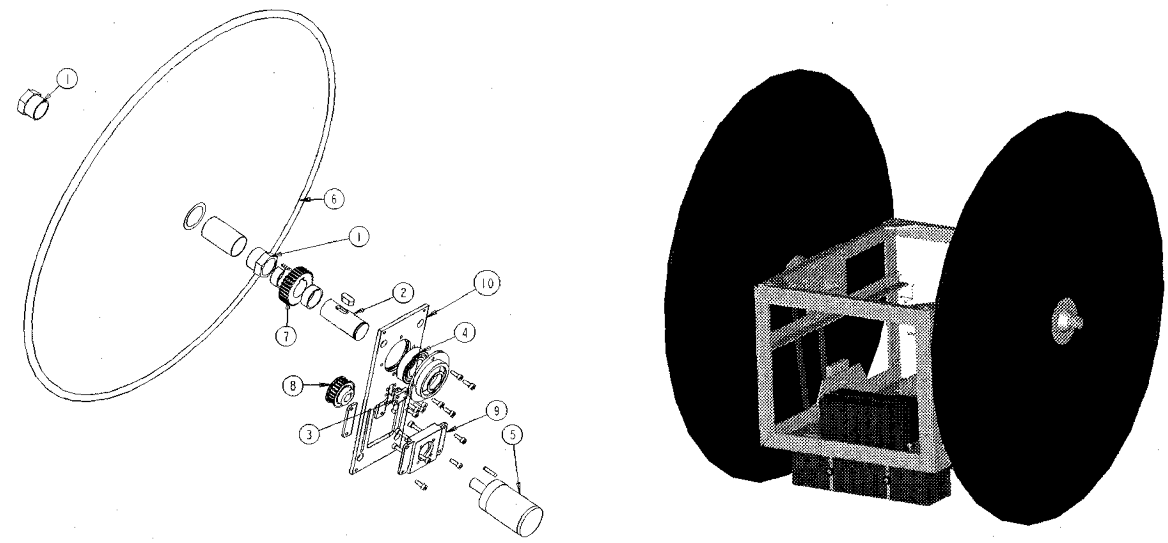

(a) (b)

Figure 4.5: (a) Exploded view of the second RDS; (b) third RVP under no load

This RDS solution turns out to be more cost-effective than that shown in Fig. 4.3a; in fact, the machining costs are dramatically cut down by the selection of a commercial wheel. Moreover, the selection of a cheaper aluminum alloy, namely, Al 6061 (as opposed to Al 7075 featured by the first solution), for most of the components, helps to further reduce the overall robot cost.

4.4 Third Design Solution

Although the second design solution allows for sensor redundancy and for direct sensing of the wheel rotation (e.g. by means of an optical encoder that might be housed in the robot chassis and connected to the custom-made shaft), we discard it. There are several reasons behind this decision, which is mainly dictated by the need for simplicity and cost-reduction, along with the possibility of investigating the effect of toe and camber-angle variation on relatively low-speed vehicles (as compared to high-speed ones, such as cars). To do this, the *front* bicycle wheels and custom-made shafts are replaced, along with their bearings, with *rear* bicycle wheels. This leads to the final RDS design. More specifically, instead of the custom-made shaft solution, which is rather expensive, a simpler and more cost-effective one is adopted, which uses the bicycle wheel shaft and bearings. The novel RDS is embedded in the RVP, as displayed in Figs. 4.5b and 4.6. The payload, displayed in the latter, consists of a 2 l soft-drink bottle, two food boxes and two telephone books. We can readily see how this design solution provides an optimum space utilization of the robot chassis volume. The layout of the electronic equipment is redesigned in such a way that it

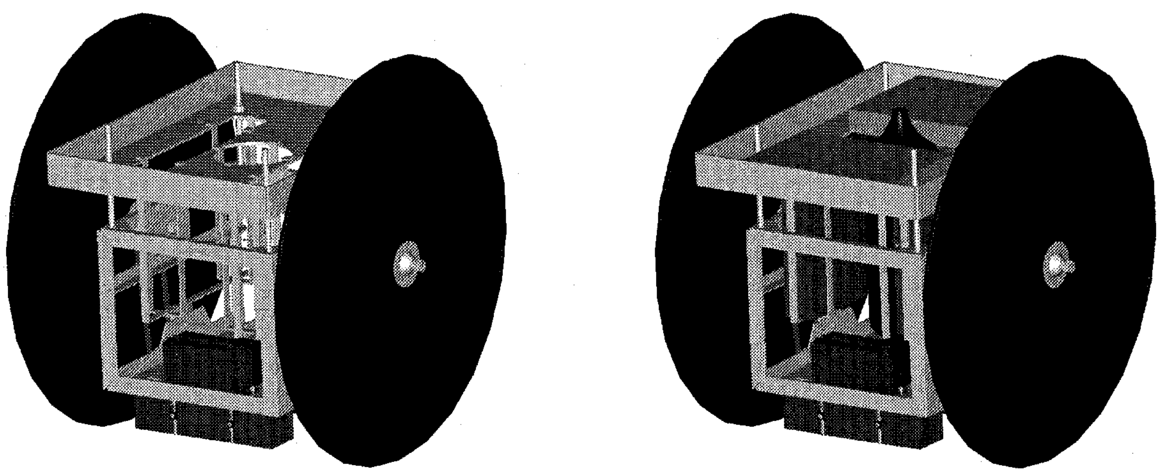

(a) (b)

Figure 4.6: (a) third RVP with PH; (b) third RVP under full-load

can be easily serviced, much like a drawer, as shown in Fig. 4.7.

In the framework of modern mechatronics, the electrical and electronics aspects in the design and implementation of Quasimoro are not decoupled from the mechanical ones. As a matter of fact, in selecting the type of controller we have to devise a system such that: *i*) it is limited in dimension in order to easily fit inside the robot

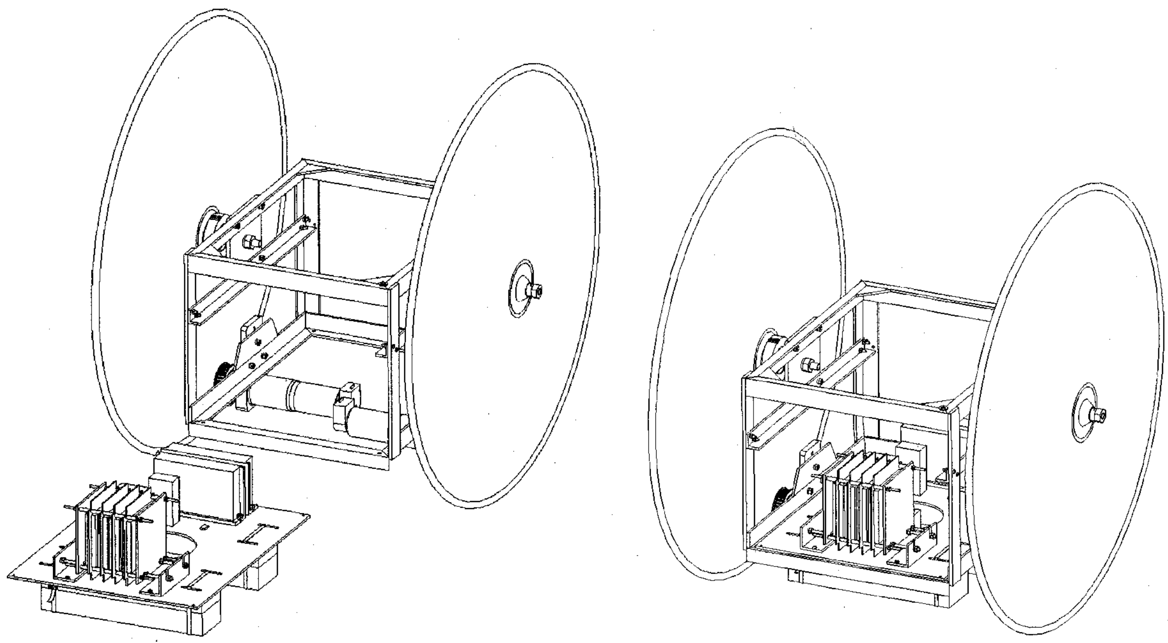

Figure 4.7: Electronic equipment servicing—third RVP

chassis, *ii*) it is lightweight in order to make the robot easily transportable, and *iii*) it has sufficient processor speed, memory size and I/O precision in order to implement dynamics model-based control strategies such as CTC. The control of modern mobile robots usually relies on the knowledge of their kinematics. Therefore, most of the time a micro-controller is selected as the control unit, the computational cost of kinematic control algorithms being not significant for such devices. However, if the objective is to implement model-based control strategies, such as CTC, we need to select controllers with higher performance than micro-controllers. In this light, we select a PC/104 computer board for the Quasimoro controller.

The base plate of the robot, made of Al6061T6, is designed for hosting the PC/104 stack, PAs and battery packs; the latter are located below the platform in order to lower the robot MC in a balanced (front-back) way. Therefore, the base plate is practically parallel to the ground when the system is unloaded and at rest. A timing belt is secured to the PG output shaft by means of a key and two set screws. The timing belt design features a 232.45×10^{-3} m nominal centre distance at installation; considering a

	Driving pulley	Driven pulley	Timing belt
P/N:	A6A55M034DF0912	A6A55M040NF0912	A6R55M130090

Table 4.4: Timing belt transmission components—third design solution

no more than $0.25'' = 6.35 \times 10^{-3}$ m variation from assembly and manufacturing tolerances, the minimum centre distance is 226×10^{-3} m, as depicted in Fig. 4.8a. In order to take into account the belt take-up phenomenon (SDP/SI Inc., 1991), which reflects in a maximum adjustment in the center distance of $0.5'' = 12.7 \times 10^{-3}$ m from its nominal value, three slots are vertically machined on the motor mount. The reduction ratio achieved by the timing belt transmission is practically unity (1.18), the selected pulleys and belt being those of Table 4.4, where P/N is the part number (SDP/SI Inc., 1991). The pulleys are made of aluminum alloy and the timing belt is of the *PowerGrip GT* type made of neoprene with fiberglass tension members (SDP/SI Inc., 1991).

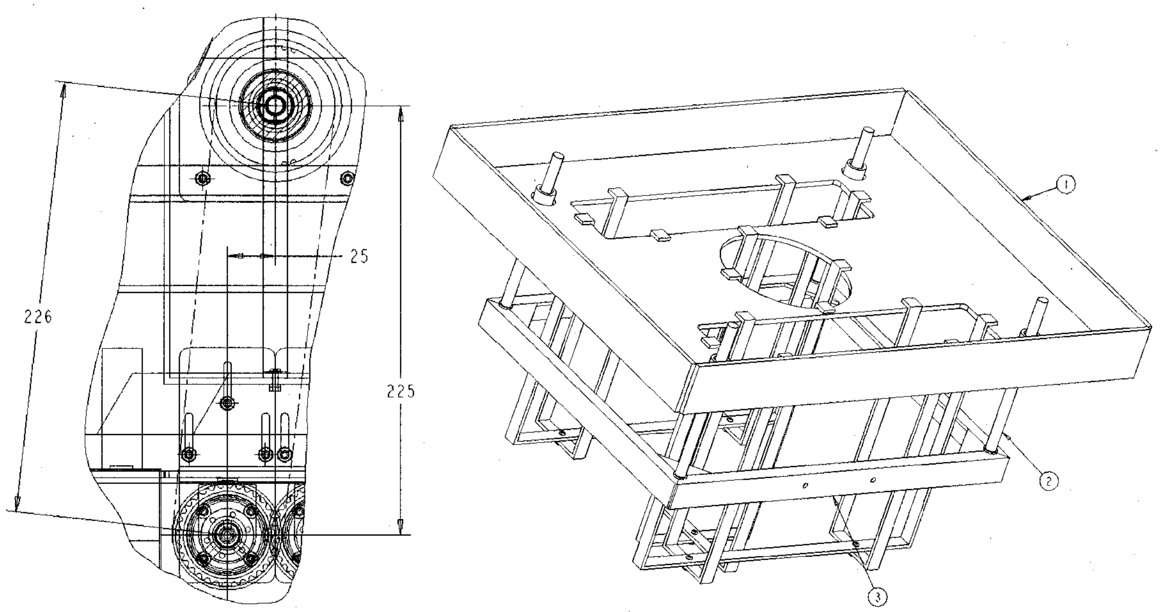

(a) (b)

Figure 4.8: (a) Third RDS design (side view); (b) PH design

The payload holder (PH), shown in Fig. 4.8b, consists of a tray with three subframes, which are meant for holding books and bottles.

The robot chassis consists of 14 extruded aluminum alloy stock components, which are welded together, and two plates, namely, the wheel plate and the motor mount, which are screwed on the welded frame, as depicted in Fig. 4.9a. The motor mount has three vertical slots in which are located the three nut-bolt sets that secure the motor mount to the robot chassis; these slots are designed for belt tension regulation.

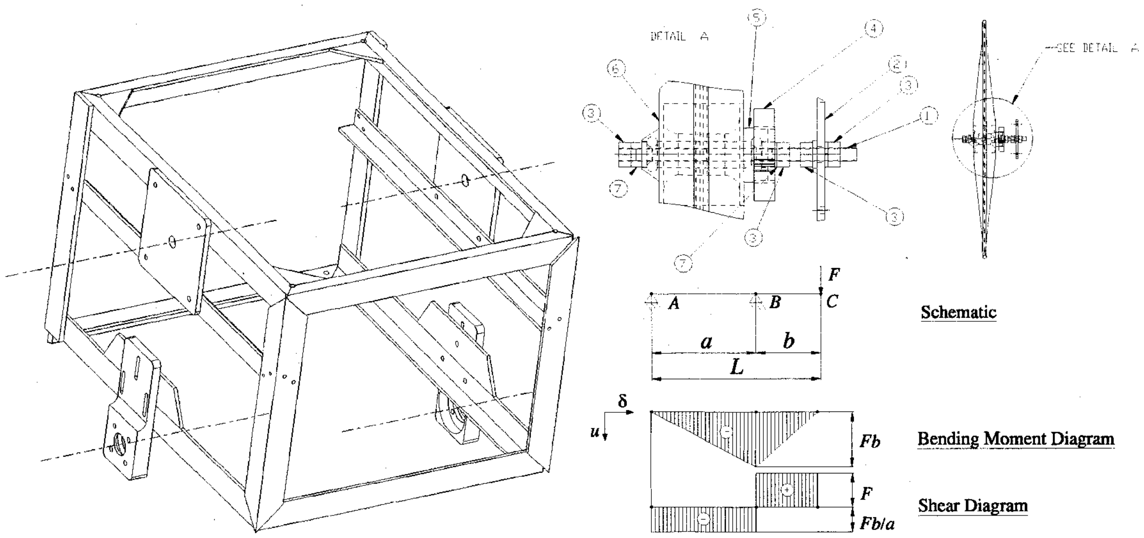

(a) (b)

Figure 4.9: (a) Third robot chassis design; (b) Bicycle wheel axle stress analysis

Please see Appendix B for further details.

4.4.1 Robot Drive System Design

The scheme for the stress analysis is included in Fig. 4.9b, where the two supports represent the bearings of the wheel, while the force is half the weight of the robot. The bending moment computed at section B of Fig. 4.9b is given by

$$M_B = Fb \tag{4.7}$$

where F is the force acting at section C, while b is the distance between sections B and C. The shear force diagram is discontinuous at section B. The shear force between sections B and C is given by F, while between sections A and B is Fb/a.

The polar moment of area of the wheel axle is given by

$$I = \frac{\pi d^4}{64} \tag{4.8}$$

where d is the nominal diameter of the wheel axle.

Moreover, the vertical displacement of section C is given by (Juvinall and Marshek, 2006)

$$u_C = u_{max} = \frac{Fb^2 L}{3EI}. \tag{4.9}$$

while the normal stress measured at the critical section B is given by (Viola, 1985)

$$\sigma_B = \frac{M_B r}{I} \tag{4.10}$$

where $r = d/2$. By substituting eqs. (4.7) and (4.8) into eq. (4.10), we have

$$\sigma_B = 32\frac{Fb}{\pi d^3}. \tag{4.11}$$

We can then estimate the shear stress at the critical section B using Jourawski approximation formula (Viola, 1985)

$$\tau_B = \frac{T_B S}{Id} \tag{4.12}$$

where $T_B \approx F$ is the shear force computed at section B (we take the highest of the two discontinuity values of shear force at section B), while S is the static moment of the cross-section (Viola, 1985), i.e.,

$$S = \frac{2}{3}r^3.$$

In this light we have

$$\tau_B = \frac{16}{3}\frac{F}{d^2\pi}. \tag{4.13}$$

Using eqs. (4.11) and (4.13), one can compute the combined stress of the critical section B according the Huber-von Mises-Hencky failure criterion for ductile materials, also known as von Mises stress (Viola, 1985)

$$\sigma_{B,H} = \sqrt{\sigma_B^2 + 3\tau_B^2}\ . \tag{4.14}$$

The admissible combined stress is given by

$$\sigma_{adm} \leq \frac{\sigma_y}{s}$$

where σ_y is the yield stress of the material—$\sigma_y = 417.1\,\text{MPa}$ for AISI 4140 steel, as per p. 512 of (Oberg et al., 1988)—and s is a safety factor. More specifically, $\sigma_{adm} = \sigma_{B,H}K$, where K is the stress-concentration factor—see p. 209 of (Oberg et al., 1988):

$$K = 1 + q(K_t + 1) \tag{4.15}$$

where K_t is the theoretical stress concentration factor, while q is the index of sensitivity of the material. Moreover, we know that $L = 0.117\,\text{m}$, $a = 0.0715\,\text{m}$, $b = 0.0455\,\text{m}$, $d = 3/8'' = 0.009525\,\text{m}$, and that $F = (M/2) - m_w^\star = 111.515\,\text{N}$, where M is the overall weight of the robot (under full-payload) in Newtons, while $m_w^\star$ is the sum of the weights of the wheel rim, spokes and tire in Newtons as well. M and $m_w^\star$ are both estimated using the `model analysis/MASS PROPERTIES` built-in function of *PRO/Engineer 2001i*. In this light eqs. (4.11), (4.13) and (4.14) yield

$$\sigma_B = 5.981 \times 10^7\,\text{Pa} \quad \tau_B = 2.087 \times 10^6\,\text{Pa}$$

and $\sigma_{B,H} = 59.920\,\text{MPa}$ respectively. With $E = 30 \times 10^6\,\text{psi} = 2.068 \times 10^5\,\text{MPa}$ denoting the modulus of elasticity of steel—p. 512 of (Oberg et al., 1988)—eq. (4.9) becomes

$$u_{max} = 0.108 \times 10^{-3}\,\text{m}.$$

The bicycle wheel shafts used in Quasimoro feature a $3/8'' = 0.009525\,\text{m}$ diameter and 26 tpi[6]. The reciprocal of the latter is the axial pitch p—p. 1477 of (Oberg et al., 1988). The height of the thread is given by $H = 0.866p = 0.846 \times 10^{-3}\,\text{m}$, hence the depth of the thread is $d_t = 0.625H = 0.529 \times 10^{-3}\,\text{m}$—p. 1474 of (Oberg et al., 1988). Therefore, the basic major diameter of the threaded shaft being equal to $D = 3/8'' = 9.525 \times 10^{-3}\,\text{m}$, the minor diameter is $d = D - 2d_t = 8.467 \times 10^{-3}\,\text{m}$. A

[6]tpi stands for the number of threads per inch.

conservative assumption is to consider the smallest fillet radius of the threaded shaft $r = 0.108p = 0.105 \times 10^{-3}\,\mathrm{m}$—see p. 1481 of (Oberg et al., 1988). For the given values of D, d and r one can compute $K_t = 3.5$—see Fig. 7 of p. 212 of (Oberg et al., 1988). $q \in [0.4, 0.6]$ for ductile materials, and hence, a conservative value of q is $q = 0.6$. In this light, the stress-concentration factor formula (4.15) returns $K = 2.5$. Therefore, choosing a safety factor $s = 1.3$—see p. 208 of (Oberg et al., 1988)—we have

$$\sigma_{adm} = 149.8\,\mathrm{MPa} \leq \frac{\sigma_y}{1.3} = 320.8\,\mathrm{MPa}.$$

With this inequality strictly satisfied, it is apparent that the use of the bicycle wheel shaft in the Quasimoro design meets the prescribed safety requirements.

4.5 Robot Semiconductor Power Switch

Mechanical contactors specifically designed to switch DC are commercially available. However, their current rating is usually less than 30 A. Some AC contactors are rated to switch DC at a considerably derated (lower) voltage. This voltage rating may be sufficient for some lower battery pack voltages. When multiple poles of a multiple breaker are placed in series, a higher DC rating may be allowed (Walker, 1999). This leads to increased size and weight.

An alternative to a mechanical contactor is to use a semiconductor contactor that features smaller size and weight. In mobile robot design both weight and dimensions are critical parameters and should be minimized whenever possible during robot-component dimensioning. For this reason, Quasimoro features a semiconductor power switch.

Quasimoro's power switch is dimensioned according to the reference values

$$I_{max,out,batt} = 58\,\mathrm{A} \quad V_{batt,max} = 42\,\mathrm{V}$$

that are the maximum output current and the maximum output voltage of the battery. The $I_{max,out,batt}$ value is computed taking into account the output peak current of the robot PAs and the maximum input current of the robot control unit power supply—see Subsection 4.7.3.

Quasimoro's power switch is based on an original *design* carried out for another mobile robot (McMordie, 2002; Campbell, 2004). A similar design can be found also as a sub-circuit of the custom-made DC circuit breaker of the *Sunshark* solar racing car—Fig. 2 of (Walker, 1999). Moreover, the printed-circuit board (PCB) *implementation* is identical to that of a previously designed system (Smith and Sharf, 2005).

As core discrete components of Quasimoro's power switch, metal oxide semiconductor field effect transistors (MOSFETs) are chosen because of their lower conduction losses for the given reference voltage ($V_{batt,max}$). The use of insulated gate bipolar transistor (IGBT) may be suitable for higher voltages.

4.5.1 Simulation Results

Using 5SPICE[7], several simulation tests are run. The goal is to analyze the time-response of the power switch upon different load conditions and power switch states, before prototyping the contactor.

With reference to the schematic of Fig. 4.10, several load conditions are simulated. Details on the results of these simulations are reported in Section 6.1.

The resistances R_1 and R_2 are 2.7 kΩ and 150 kΩ, respectively (Smith and Sharf, 2005). Simulation results show that when the output terminal of the power switch is short-circuited (load of negligible resistance) and the J3 switch is in the OFF position, the circuit prevents a load current of 167 A from flowing. Moreover, whatever the load is (from short-circuit to full load condition) the load current never exceeds 0.0335 mA as long as J3 is in the OFF position.

We also analyze eight different scenarios in order to test the design of the power switch, see Table 4.5. In the latter $R_{load} = 0\,\Omega$ represents a short-circuit at the output terminals of the power switch.

Under testing conditions #2 we have no current flow in the circuit. We study

[7] `http://www.5spice.com/`

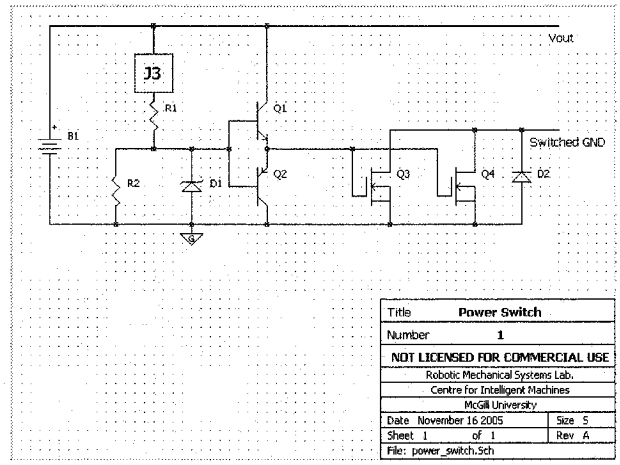

Figure 4.10: Power switch schematics

Test #	J3 status	Description
1	open	$R_{load} = 0\,\Omega$
2	open	$R_{load} = 1\,\mathrm{T}\Omega$
3	closed	$R_{load} = 0\,\Omega$
4	closed	$R_{load} = 1\,\mathrm{T}\Omega$
5	open	$R_{load} = 1000\,\mathrm{K}\Omega$
6	closed	$R_{load} = 1000\,\mathrm{K}\Omega$
7	open	$R_{load} = \infty$ (no load)
8	closed	$R_{load} = \infty$ (no load)

Table 4.5: Simulation test set-up for current flow analysis

also the current path—i.e. the set of segments of a circuit which are interested by a current different from zero. They are indicated in Figs. 4.11–4.12 by thicker lines. From the simulation results reported in Figs. 4.11–4.12, one can observe that the desired functionality of the power switch is achieved.

It is noteworthy that

- tests #5 and #6 feature the same *current path*, except for the absolute values of the currents, of tests #1 and #3, respectively (only the absolute values of the currents are different) and

- test #7 features the same voltage and current readings of test #2.

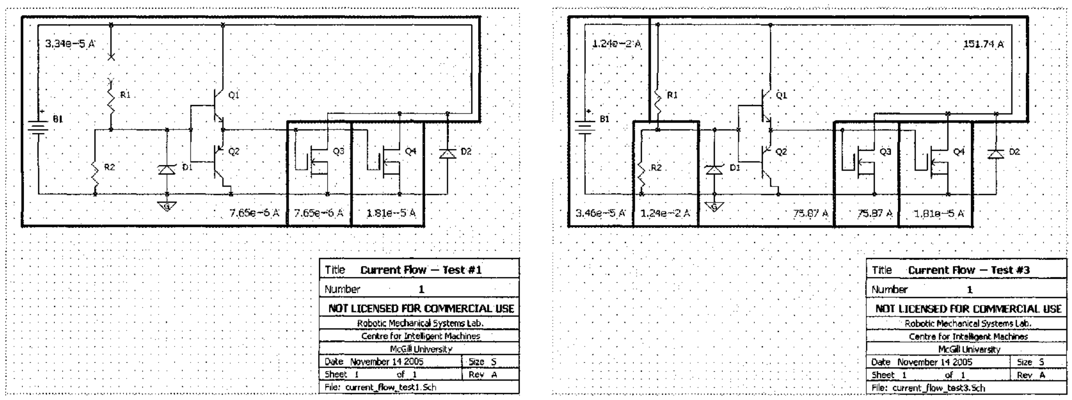

(a) (b)

Figure 4.11: Current flow (a) Test #1; (b) Test #3.

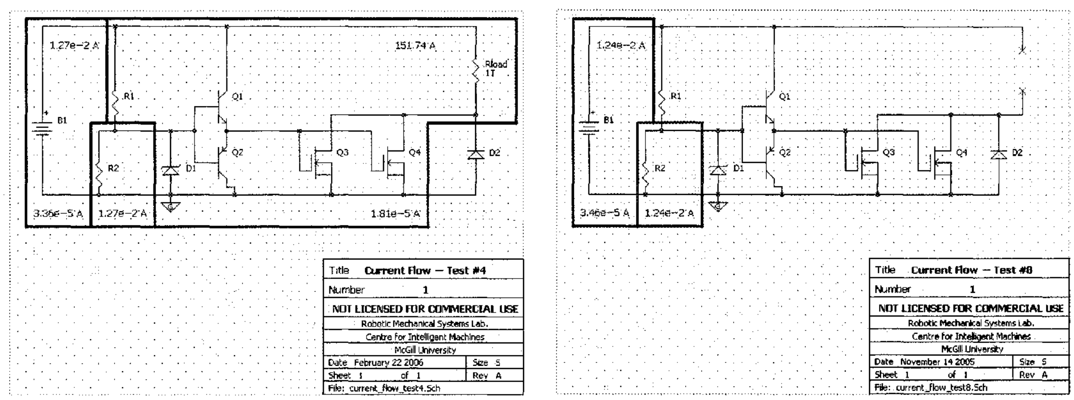

(a) (b)

Figure 4.12: Current flow (a) Test #4; (b) Test #8.

4.6 Final Analysis of Robot Dynamics Prior to Manufacturing

Once all the components (motor, PGs, PAs, battery, etc.) of a robotic system have been identified and virtually interfaced in a CAD environment, the robot dynamics needs to be analyzed taking into account the mathematical model of its components.

4.6.1 Power Supply Modelling

Since electrically powered robots can draw significant peak power and operate from non-ideal voltage sources, the variation of the supply voltage as a function of the total load current must be considered. As shown in (Poulakakis, 2002) a very good match between measured and modelled supply voltage is given by $V = V_{nom} - iR_{in}$, where V_{nom} is a fixed internal voltage source in series with an internal resistance R_{in}, while V and i are the voltage and the current delivered by the battery, respectively.

Quasimoro is powered by two Nickel-metal Hydride battery packs arranged in series; each pack has 14 *Sanyo Twicell HR-D* cells. This set-up is characterized by $V_{nom} = 33.6\,\text{V}$ and $R_{in} = 0.084\,\Omega$ (Sanyo Group, 2004).

4.6.2 Drive System Modelling

The drive system of an electrically powered robot consists of a motor and a power amplifier. Two different kinds of torque-speed limitation of the drive may take place, namely, motor saturation and amplifier saturation. More specifically, the torque applied by a DC motor is directly proportional to the current applied at its input terminals (by the amplifier), provided that motor and amplifier are not saturated. Since the electrical time constant of a DC servomotor is much smaller than the mechanical time constant because of the low inductance of the motor, we can perform an initial approximation by neglecting the armature inductance. Therefore, the j-th ($j = 1, 2$) robot motor can be modelled as (Poulakakis, 2002):

$$\tau_{j,m} = \begin{cases} K_t i_j & \text{for } n \leq n_{j,\max} \\ K_t(V - K_n n_j)/R_A & \text{for } n_j > n_{j,\max}\,\text{(saturation)} \end{cases}$$

where $n_{j,\max} \equiv (V - R_a i_j)/K_n$, K_t is the torque constant, K_n is the speed constant, R_a is the armature resistance, $\tau_{j,m}$ is the actual (delivered by the motor) output torque of the motor (computed at the output shaft of the motor), n_j is the output speed of the motor (computed at the output shaft of the motor), and i_j is the input current of the motor. The power amplifier takes a voltage signal, as required by the desired torque (dictated by the controller) and outputs a current signal; this voltage is the input to the motor. The amplifier is considered as an ideal current source, there being thus no voltage drop across it. Under this assumption, the amplifier can be modelled as (Poulakakis, 2002)

$$i_{j,m} = \begin{cases} \tau_{d,j,m}/K_t & \text{for } i \leq i_{j,\text{peak}} \\ i_{j,\max} & \text{for } \tau_{d,j,m} > K_t i_{j,\text{peak}}\ \text{(saturation)} \end{cases}$$

K_t [Nm/A]	K_n [sV/rad]	R_A [Ω]	$i_{j,\text{peak}}$ [A]
0.030	3.312×10^{-4}	0.316	12.000

Table 4.6: RDS parameters of Quasimoro

where $\tau_{d,j,m}$ is the desired output torque of the j-th motor (computed at the output shaft of the motor) while $i_{j,\max}$ is the maximum continuous output current of the amplifier.

Quasimoro's drive system consists of *i*) two *Maxon RE* 40 (148867) motors equipped with a planetary gearhead, namely, a *Maxon GP* 42 *C* (203123) (Maxon Precision Motors, Inc., 2003); and *ii*) two *Advanced Motion Controls* 25*A*8 servo amplifiers (Advanced Motion Controls, 2004c); the drive system has the parameters displayed in Table 4.6.

In order to verify the proper operation of the robot, we conduct a series of numerical simulations of the robot kinematics and dynamics along with the power supply and actuation system dynamics. Simulation runs are carried out using Matlab 6.5.1.199709 and Simulink 5.1 (R13SP1) with the variable-step solver ODE45 (Dormand-Prince). The mathematical model used in the simulation runs relies on that described in Section 3.2. The following assumptions are made: *i*) the robot undergoes motion on an inclined planar surface of 20%-slope; *ii*) the robot wheels are always in contact with the ground; *iii*) linear viscous damping in the bearings, accounted for by means of a Rayleigh dissipation function (Angeles, 2003); and *iv*) the presence of the reaction torque on the IB. In these simulations we also consider the moments of inertia of the driving pulleys, motor rotor and PG, along with the friction torque stemming from motor brushes and bearings—0.245 Nm, see (Maxon Precision Motors, Inc., 2003)—and the gradient (i.e. slope-related) resistance: $\tau_g = [Mgr \cos \arctan (0.20)]/2 = 6.761$ Nm.

The viscous damping coefficient b is estimated by simulating the open-loop dynamics of the system under a rectilinear motion with an initial velocity of 2 m/s. We assume an exponential decay of the robot velocity to 0.2 m/s in time T under the effect of gravity and damping. To be on the safe side, two different values of T are used:

Payload	$J_1, J_2\,[\mathrm{kg\,m^2}]$	$m, m_3\,[\mathrm{kg}]$	$d, r, l\,[\mathrm{m}]$
Minimum	0.402, 0.588	2.507, 15.275	0.113, 0.305, 0.448
Maximum	0.531, 0.851	2.507, 22.735	0.061, 0.305, 0.448

Table 4.7: Geometric and inertial parameters

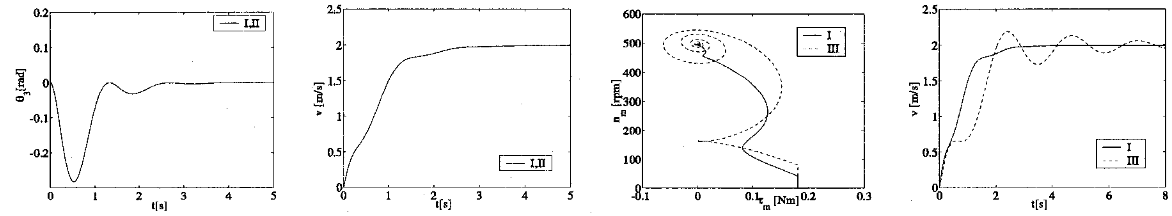

(a) (b) (c) (d)

Figure 4.13: (a) θ_3 vs. t; (b) v vs. t; (c) actuator torque-speed curve; (d) v vs. t.

$T = 10\,\mathrm{s}$ and $T = 50\,\mathrm{s}$, which returns $b = 0.275\,\mathrm{Nms/rad}$ and $b = 0.000275\,\mathrm{Nms/rad}$, respectively. The PRO/Engineer-calculated values of the geometric and inertial parameters of the robot third design solution, for a minimum payload (i.e. no payload) and a maximum payload are included in the simulation runs, see Table 4.7.

From additional simulation results we can conclude that *i*) even if the power amplifiers saturate, the robot performance does not change, see Fig. 4.13a-b; and that *ii*) the system features robustness with respect to both payload and initial tilt-angle variation, see Fig. 4.13c-d (Salerno and Angeles, 2004b). The robustness with respect to parametric uncertainty is analyzed by comparing the closed-loop (CL) dynamics of the robot while carrying out the rectilinear motion manoeuvre starting from rest:

I) under maximum payload-condition; and

II) the one under minimum payload-condition.

In order to analyze the robustness of the controller with respect to the latter we compare the CL dynamics of the robot while carrying out the rectilinear motion manoeuvre under maximum payload

I) starting from rest (stable equilibrium configuration); and

III) from an initial condition such that $\theta_3(0) = 30^\circ$[8].

[8] We used III) in order to distinguish it from II).

The use of motor incremental encoders, IB tilt sensor and of a linear-quadratic regulator (LQR) is assumed in the simulated control architecture (Salerno and Angeles, 2004b). This assumption can be dropped since satisfactory performance can be achieved without resorting to the LQR, as shown in Chapter 6.

4.7 Prototype

A prototype of Quasimoro has been manufactured and assembled, see Fig. 4.14a.

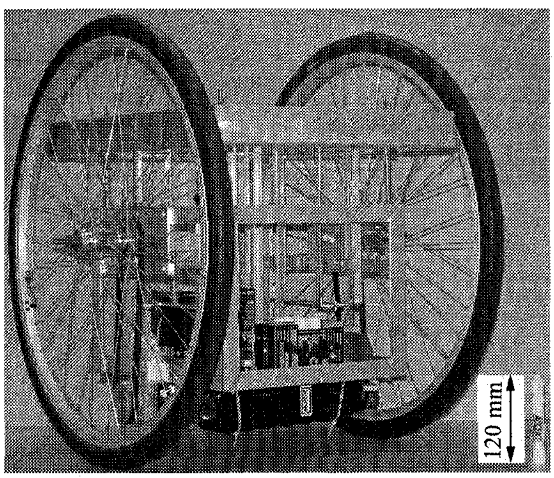

(a)

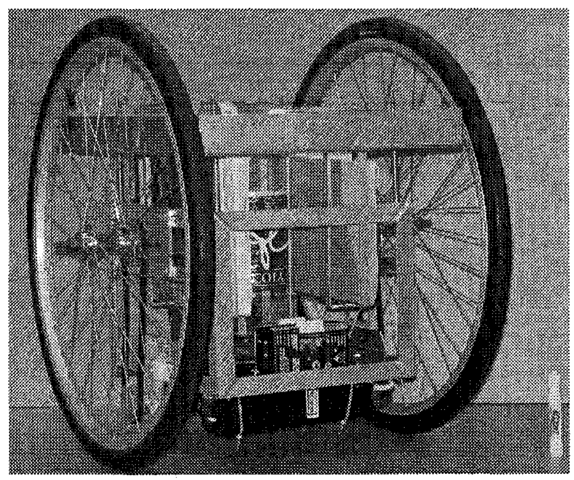

(b)

Figure 4.14: Mechanical prototype under (a) no load and under (b) full-load

The core of the mechanical structure is designed and fabricated so as to be easily interfaced to different devices that would be custom-made for complying with different applications in other fields, such as entertainment, surveillance and medical robotics (as an assistive technology device for hospital patients) and RHA. However, for the specific application of robotics for paraplegic WU augmentation, a specialized PH module is designed to be easily removed from the robot and to hold books, medication, food, drinks and any other item that the user might need on a daily basis, as depicted in Fig. 4.14b. Under nominal full payload, i.e. 75 N, the robot preserves its stability at rest without any need of powering the motors, as opposed to Segway^{TM} (Segway Inc., 2005; Kamen et al., 2000) and other self-balancing two-wheeled systems (Salerno and Angeles, 2004c).

The RDS, depicted in Fig. 4.15a allows to dampen the oscillations of the intermediate body during robot motion. This is mainly due to the presence of timing belts and of commercial bicycle bearings. Moreover, the robot actuators, the heaviest components after the battery, are successfully installed below the robot chassis so that the robot static and dynamic stability is strongly improved.

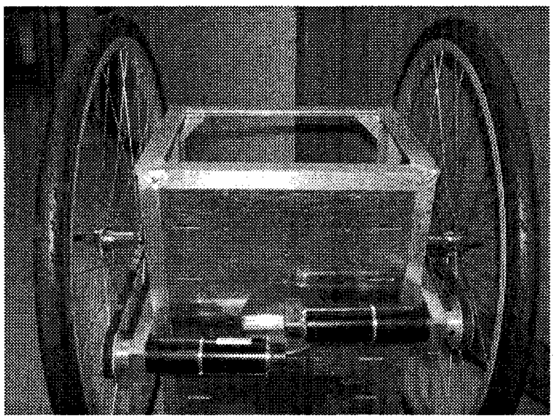

(a)

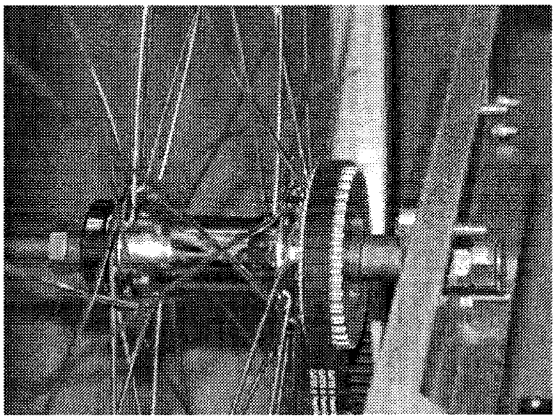

(b)

Figure 4.15: RDS: (a) actuation system (bottom-front part of the robot) and (b) driven pulley close-up

In order to transmit torque to the wheels, a timing pulley is threaded, screwed and glued on the traditional threaded hub—minus the freewheel mechanism[9] and the sprocket(s)—of a rear bicycle wheel, as depicted in Fig. 4.15b. The design gives the possibility of modifying the wheel camber, and the toe angle by simply interposing wedges between the wheel plate (to which the bicycle wheel shaft is secured) and the robot chassis.

Most of the beams composing the robot chassis are welded together, thus saving time and money on robot maintenance by reducing to a minimum the number of screws that need to be periodically re-tightened.

The layout of the electronic equipment is designed in such a way that it could be easily serviced, much like a drawer, as shown in Fig. 4.16a.

[9] `http://www.sheldonbrown.com/freewheels.html`

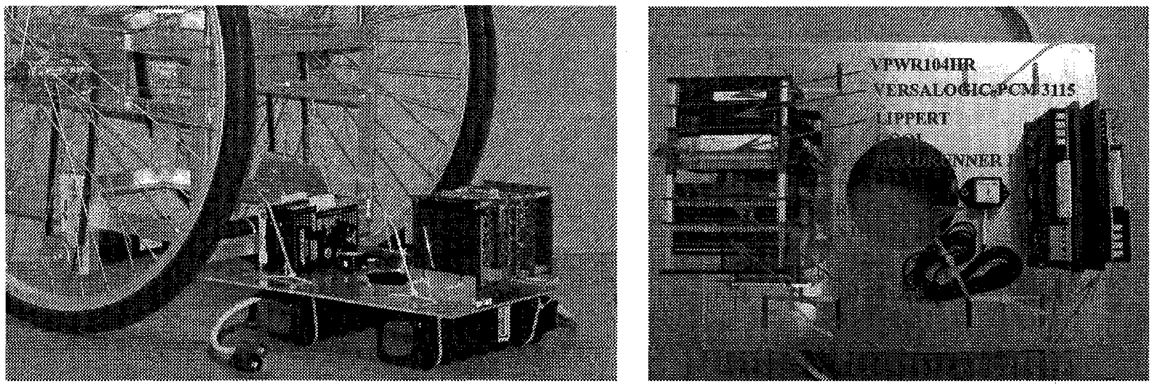

(a) (b)

Figure 4.16: Electronic equipment (a) servicing and (b) top view

4.7.1 On-Board Control Unit

The *Cool RoadRunner II* is selected as the PC/104 computer board (LiPPERT Automationstechnik Gmb, 2001), shown in Fig. 4.16b. This all-in-one board by *Lippert* features a 300MHz Pentium®-Class central processing unit (CPU), which is fast enough for implementing model-based control strategies (Villani et al., 2000). Moreover, it does not require active cooling and has all the peripherals that constitute a PC on board along with 256 Mbyte SDRAM and CompactFlash™ socket. In order to implement real-time control algorithms, a dedicated operating system (OS) is selected. The *QNX 6.1* OS is installed on a *Kingston* 256 MByte compact flash card (Krten, 1999).

4.7.2 Communication

In order to endow the robot with wireless communication capabilities, a PC/104 PCMCIA module, namely, the PCM-3115 by *Versalogic* (Versalogic Corp., 1997), is stacked on to the Quasimoro CPU board, shown in Fig. 4.16b. An *Orinoco Classic Gold* wireless card is used in conjunction with the PCM-3115 to establish communication between the robot and a desktop PC.

Direction	Type	Quantity
Input	**Analog**	
	Applied Torque	2
Output	**Analog**	
	Commanded Torque	4
	Digital	
	Power Amplifier Enable Signals	2

Table 4.8: I/O requirements (excluding tilt sensor and HCTL signals)

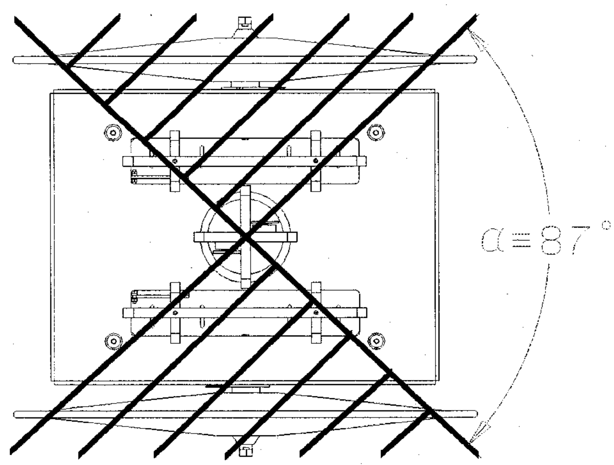

Figure 4.17: Visual field limitation of the robot

4.7.3 System Integration

The selection of the I/O board, a *Micro/Sys MPC550* (Micro/Sys, Inc., 1999), shown in Fig. 4.16b, is dictated by the requirements displayed in Table 4.8. The redundancy of DIO and A/D channels with respect to the requirements allows for redundant sensing. A PC/104 power supply, the *VPWR104HR* by *RTD Embedded Technologies* is selected (RTD Embedded Technologies, 2003), as shown in Fig. 4.16b. This selection is mainly dictated by the nominal voltage of the robot battery packs (33.6 V), which is in the input voltage range required by the VPWR104HR (8–40 V); this range is wide enough to make the VPWR104HR extremely suitable for battery-powered vehicle systems, such as Quasimoro.

Future versions of Quasimoro will be endowed with other sensors in order to increase the robot *autonomy* and *intelligence.* With reference to range finding and vision sensors, there are two challenges to face here: the oscillations of the IB, and the visual field of the robot, which is limited by the wheel spokes and rims. However, the visual field limitations of the robot vary with the location of the vision sensors on the robot; for example, if a camera is located on top of the robot chassis, there is a visual field angle of about 90°, as depicted in Fig. 4.17.

More details on system integration aspects can be found in the next Chapter.

Chapter 5

Mechatronic Prototyping

5.1 Wiring and Cabling

Quasimoro harness is completely custom made. In Figs. 5.1 and 5.2 we indicate the analog-to-digital (AD) harness and digital-to-analog (DA) harness, the digital input/output (DIO) harness and the PA signal harness. Please see Appendix C for further details.

5.1.1 Robot Grounding Point and Battery Return

Almost everything that is powered electrically in a mobile robot should be grounded to the frame or the body of the robot. Each grounding point serves to complete the power loop for transmitting electrical signals within the robot. The negative

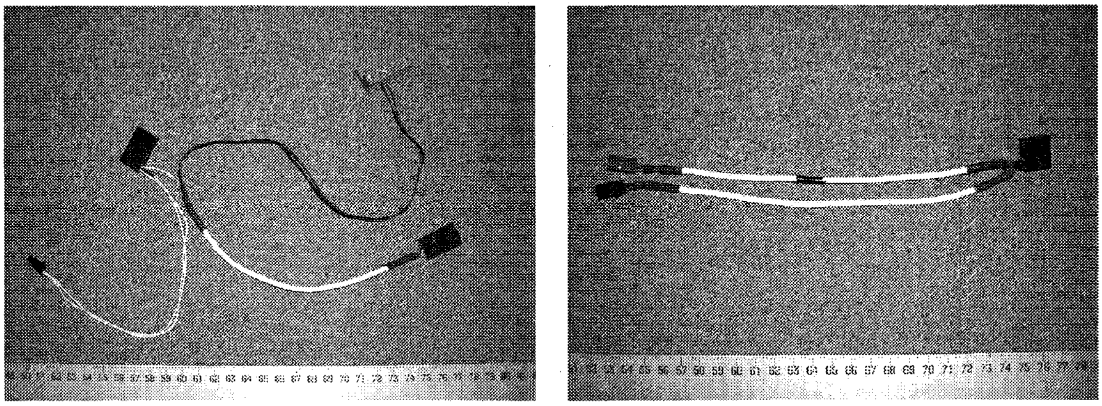

(a) (b)

Figure 5.1: The Quasimoro harness: (a) AD; and (b) DA

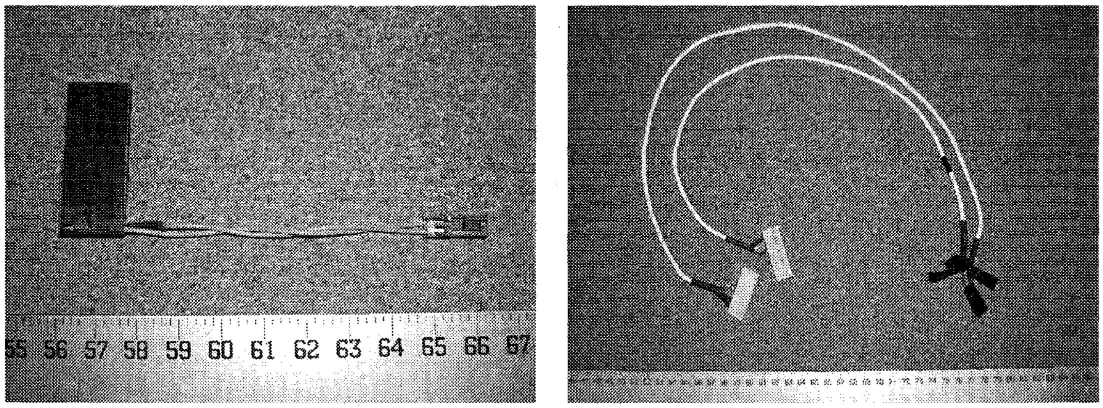

(a) (b)

Figure 5.2: The Quasimoro harness: (a) DIO; and (b) PA signal

battery terminal should also be grounded to the frame, which causes the frame to serve as a gigantic conductor, thus reducing electrical noise. However, any ground failure, whether total or partial, can play havoc on the on-board electronic system and can lead to failure of the robot on-board control unit[1]. Therefore Quasimoro's negative battery terminal is *not* grounded to the robot chassis. The electrical noise of Quasimoro's electrical system is then reduced by connecting inductive filter cards (IFCs) in-between the PAs and the robot motors (Advanced Motion Controls, 2004b).

5.1.2 Reverse Battery Protection

Future versions of Quasimoro might require the use of reverse battery protection. To this end, if power losses are not an issue, a Schottky diode—either the 120NQ405 (International Rectifier, 2005b) or the 110CNQ045ASL (International Rectifier, 2005a)—can be installed on the positive terminal of the robot battery. Otherwise, if efficiency is an issue, one can use a P-channel MOSFET, namely, the IRF 4905 (International Rectifier, 2005c) instead of the Schottky diode, by connecting the gate to the battery return and the drain to the battery positive terminal.

[1]By grounding the robot frame, for example, a major short circuit can occur if a positive lead accidentally comes into contact with the frame (Smith and Sharf, 2005).

5.1.3 Protection Against Short-Circuits

In order to protect the Quasimoro electrical system from short-circuits, a three-level fuse-based system is implemented. A time delay fuse F1—see Table 5.1—is installed on the cable connecting the positive terminals of the battery and the power switch. Two slow-blow fuses, F2, connect the positive input power terminals of the PAs with the positive output terminal of the power switch. Finally, a fast-acting fuse is in charge of protecting the on-board control unit of Quasimoro. This fuse, F3, connects the positive input terminal of the VPWR104HR to the positive output terminal of the power switch.

Symbol	**Part Number**	**Description**
F1	7460K313 (McMaster-Carr®)	32 V/40 A Time Delay Fuse
F2	F127-ND (Digi-Key)	250 V/15 A Slow-Blow Fuse
F3	F485-ND (Digi-Key)	250 V/10 A Fast-Acting Fuse

Table 5.1: Over-load protection system

5.2 Electrical/Electronic Hardware Re-Design

5.2.1 Power Amplifiers

The Quasimoro PAs work in current (torque) mode. The current mode produces a torque output from the motor, proportional to the input reference signal. Motor output torque is proportional to the motor current.

Mechanical commutators of brushed motors, such as Quasimoro's (Maxon Precision Motors, Inc., 2003), introduce some limitations on the starting current[2], $I_{start} = 75.9\,\text{A}$, and the maximum permissible speed, $n_{max,perm} = 8200\,\text{rpm} = 858.27\text{rad/s}$. However, both in simulation runs and experiments, the current and the speed of Quasimoro's actuators never exceed I_{start} and $n_{max,perm}$, respectively. This is achieved by a three-layer control:

- via software, by means of the robot control algorithm;

[2] I_{start} is the maximum current that the brushes can sustain without shortening the motor life.

- via hardware, by setting the peak current flowing through the motor windings to a value of $\approx 12\,\mathrm{A}$, see Section 5.3;

- via hardware, by connecting a slow-blow fuse, see Table 5.1, between power switch and PA.

Enabling/Disabling the Power Amplifier

The "inhibit lines" of the AMC25A8 power amplifiers of Quasimoro are inverted for safety reasons. More specifically, when a ground signal is assigned to each of the inhibit lines, the PA will turn OFF. This inhibition will cause a FAULT condition and the on-board LED will light-up to red (Advanced Motion Controls, 2004c). For safety reasons, this condition is not desirable because the PA will be enabled as soon as the power is applied to its input terminals. We would rather have the PA in a disabled state by default. To this end, the inhibit lines are inverted (Advanced Motion Controls, 2004a) by removing jumper J1, a "000" chip resistor, from the PA circuit board. This operation is extremely delicate and can produce serious harm to the PA if not executed with care and using the proper equipment. In this regard, we use a dedicate desoldering station, such as the "FP-102 Solder/Desolder Station" along with the "FM-2023 SMD Mini Parallel Remover" (HAKKO, 2006). Once the jumper-removal operation is completed, the PA can be enabled by pulling to ground the signals in input to pin $P1$-11, $P1$-12 and $P1$-13. These pins are soldered together using a jumper wire in order to minimize the amount of cables[3], as suggested by Smith and Sharf (2005).

Quasimoro does not use pin $P1$-10, which is intended for modifying the maximum continuous $I_{max,cont}$ torque preset by the PA manufacturer. In this regard, the maximum output continuous torque $I_{max,cont}$ of the PA is bounded to be half the peak output torque I_{peak} (i.e. $I_{peak} = 2I_{max,cont}$). However, future versions of Quasimoro can benefit from setting the $I_{max,cont}/I_{peak}$ ratio to a different desired value by connecting

[3]Given the length of the jumpering wire of only 0.004 m no PVC wire-cover is required.

a properly dimensioned resistor between pin $P1$-10 and pin $P1$-2 of the PA (Advanced Motion Controls, 2004c).

5.2.2 Electromagnetic Interference—Inductive Filter Cards

In order to reduce electrical noise generated by electro-magnetic interference (EMI) and to increase the longevity of the Quasimoro motors, two inductive filters, one per motor, are dimensioned. One of the feasible solutions is to use two (one per PA) high current filter inductors from *Vishay Dale* (model number: IHV-30-150)(Vishay Dale, 2001). However, we select to use two IFCs, which are equipped with capacitors as well, that would help in meeting both noise-prevention and minimum-inductance requirements[4]. The selected IFCs are two FC15030 from Advanced Motion Controls (2004b); they filter the signal from the PA to the motor by means of an inductance (line to line) of 300 μH and a capacitor (Advanced Motion Controls, 2004b). Furthermore, robot noise-sensitive sensors benefit from the use of these IFCs that feature inductors and capacitors as well.

In order to dimension the IFCs both specifications on nominal inductance of the IFC and its current rating needs to be taken into account. More specifically, the PWM-generated current-rise-time depends on both bus voltage and load inductance (the IFC is to be considered a load in series with the motor). Therefore, certain minimum load inductance requirements are necessary, depending on the bus voltage. The Quasimoro PAs require a minimum load inductance of 200 μH at 20 V (the higher the bus voltage the smaller the minimum required inductance). In this light, a combined (motor plus IFC) load inductance of 380 μH at 30.8 V (minimum acceptable Quasimoro battery voltage before recharge) meets the requirements. Moreover, the continuous current of the Quasimoro IFC is 30 A (Advanced Motion Controls, 2004b), which is greater than the 25 A of maximum continuous current of Quasimoro PA (Advanced Motion Controls, 2004c). Therefore, the requirements for system integration are met.

[4] In order to interface PWM PAs with DC motors one needs to take into account the minimum inductance requirement of the PA.

The inductance of the IFCs is also sufficiently high to prevent the motor overheating when at rest. This phenomenon is typically experienced by PWM-operated motors featuring low inductance.

5.3 Power Amplifier Calibration

Since Quasimoro's PAs close the current loop internally, poor current loop tuning cannot be corrected with tuning from an external controller. Therefore, it is necessary

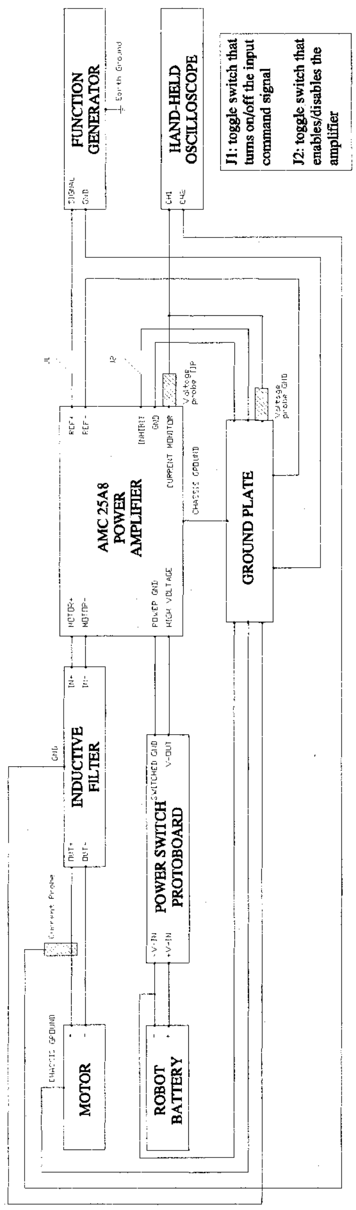

Figure 5.3: Experimental set-up for PA calibration

to properly calibrate the Quasimoro PAs in order to guarantee the success of robot control strategies. The desired performance can be achieved only after PA calibration is completed.

A scheme summarizing the experimental set-up used to calibrate the PAs of Quasimoro is reported in Fig. 5.3. As we can see from this Figure a common ground is used for all the components. Further, a protoboard, see Section 6.1, is used to implement the power switch.

The following equipment is needed for carrying out the PA calibration:

- A current probe[5] and a digital oscilloscope with isolated channels (not all the pins of the PA are isolated from the PA ground), such as a THS720A TEKScope (auto-ranging 100 Hz, Scope/DMM Digital Real Time 500MS/S/Channel) from Tektronix[6].
- A DMM , such as a the 175 True RMS Multimeter from Fluke[7].
- A function generator, such as a 0.2-2 Hz *GFG-8016D* from GW Instruments[8].
- A test-bench for clamping the actuator, a power strip (with surge suppressor) and a ground plate.

First, a preliminary test aimed at verifying the functionality of the sub-system composed by battery and power-switch is performed. Then, the calibration of the PAs is conducted. The first part of the calibration consists in setting the current limit and verifying the PA functionality, while the second part consists in tuning the current loop.

From the calibration of the PAs two different settings arise—see Table 5.2. *Setting*

[5]In alternative to the current probe, a properly dimensioned shunt resistor can be used (featuring a resistance that is less than 10% of the motor resistance and minimum power rating equal to that of the motor). However, results are not as accurate as with the current probe used for the reported experiments (mainly because of the power dissipated in the shunt resistor).

[6]`http://www.tek.com/`

[7]`http://www.fluke.com/`

[8]`http://www.instrunet.com/`

Pot #	*Setting A*	*Setting B*
1	$R_{23} = 25.31\,\mathrm{k\Omega}$	$R_{23} = 25.31\,\mathrm{k\Omega}$
2	$R_{12} = 36\,\mathrm{k\Omega}$	$R_{12} = 26.19\,\mathrm{k\Omega}$
3	$R_{12} = 24.37\,\mathrm{k\Omega}$	$R_{12} = 24.37\,\mathrm{k\Omega}$
4	$R_{12} = 22.13\,\mathrm{k\Omega}$	$R_{12} = 22.13\,\mathrm{k\Omega}$

Table 5.2: PA #2 calibration results

A limits the output peak current of the PA to $I_{peak} = (36/44) \times 25 = 20\,\mathrm{A}$, the maximum resistance of the on-board potentiometer *Pot #2* being $44\,\mathrm{k\Omega}$. The latter induces a torque, measured at the output shaft of the motor, equal to $\tau_{peak} = K_\tau I_{peak} = 0.030 \times 20 = 0.6\,\mathrm{Nm}$ (K_τ is the torque constant) for 2 s at most (Advanced Motion Controls, 2004c). Quasimoro motor is capable to sustain such a torque without reaching dangerous temperatures. As a matter of fact, according to the time-to-thermal-overload formula provided by the motor manufacturer, if the starting temperature of Quasimoro's actuator is 25° C, the motor is capable to maintain a torque of 1.52 Nm for 2 s without reaching dangerous temperatures.

However, the maximum continuous current of the Quasimoro motors is given by $I_{max,cont,motor} = 6\,\mathrm{A}$. Therefore, the output peak current of the PA should be $I_{peak} = 12\,\mathrm{A}$ (we recall that $I_{peak} = 2I_{max,cont}$, see Subsection 5.2.1) in order to have $I_{max,cont,motor} = I_{max,cont}$. This condition is not satisfied by *Setting A*, but is satisfied by *Setting B*, where $I_{peak} = (26.19/44) \times 25 = 14 \approx 12\,\mathrm{A}$. In this regard, *Setting B* is selected for Quasimoro control, although it does not fully exploit the motor characteristics. The choice is dictated by safety reasons. The Quasimoro application is extremely sensitive to safety issues since the robot has to be deployed in living quarters for the mobility-challenged, and has to work in strict cooperation with the user. More specifically, *Setting B* fully complies with the MPC550 DA converter specifications (Micro/Sys, Inc., 1999). If the robot control algorithm fails, *Setting B* guarantees that the maximum continuous current of the actuators (6 A) is not exceeded even if the MPC550 DA converter outputs the maximum reference signal of 10 V. On the contrary, *Setting A* can be used to implement control algorithms for

A [V]	2.000	4.000	6.000	8.000
A_I [A]	1.300	2.750	4.250	5.750
A_V [V]	0.320	0.700	1.000	1.5
$A_{I,monitor}$ [A]	1.280	2.800	4.000	6.000

Table 5.3: PA current sensor calibration

future versions of Quasimoro that might require higher torque demands.

Using either *Setting A* or *Setting B*, the system response to square waves of different amplitude and frequency is satisfactory. Hence, the default values of current loop gain and current loop integrator are acceptable. Therefore, no chip-resistor or chip-capacitor replacement is needed for the PA current loop tuning.

5.3.1 Calibration of the Current Sensor—Estimation of the Motor Torque

Each of Quasimoro's PAs is endowed with a current sensor. More specifically, pin $P1$-8 of the PA outputs a voltage, V_{cm}, which is proportional to the current measured at the motor terminals. The output signal of pin $P1$-8 provides an estimation of the motor torque because Quasimoro's actuators are two DC motors.

Using *Setting B* and inputting a 100 Hz square wave of amplitude A we measure the current at the motor terminals, I_{motor}, with a current probe. Using a voltage probe we measure V_{cm} as well. Both I_{motor} and V_{cm}, monitored by a digital scope, turn out to be 100 Hz square waves of amplitude A_I and A_V, respectively—see Table 5.3. Knowing that the signal output by $P1$-8 of the PA is proportional to the actual motor current with a scaling of 4 A/V (Micro/Sys, Inc., 1999), one can estimate the amplitude of the current at the motor terminals $A_{I,monitor}$ as $4 \times A_V$. Using the current probe read-outs A_I, one can calibrate the on-board current sensor of the PA:

$$x_1 = 1.300/0.320 = 4.062\,\mathrm{A/V}; \quad x_2 = 2.750/0.700 = 3.929\,\mathrm{A/V};$$

$$x_3 = 4.250/1.000 = 4.250\,\mathrm{A/V}; \quad x_4 = 5.750/1.500 = 3.833\,\mathrm{A/V}.$$

Hence, the factor by which V_{cm} has to be multiplied in order to return an estimation

Pot #	*Setting A*	*Setting B*
1	$R_{23} = 24.68\,\mathrm{k\Omega}$	$R_{23} = 24.68\,\mathrm{k\Omega}$
2	$R_{12} = 36\,\mathrm{k\Omega}$	$R_{12} = 26.07\,\mathrm{k\Omega}$
3	$R_{12} = 24.05\,\mathrm{k\Omega}$	$R_{12} = 24.05\,\mathrm{k\Omega}$
4	$R_{12} = 22.33\,\mathrm{k\Omega}$	$R_{12} = 22.33\,\mathrm{k\Omega}$

Table 5.4: PA #1 calibration results

of the motor current is given by

$$x_{calib} = \frac{\sum_{i=1}^{4} x_i}{4} = 4.019\,\mathrm{A/V}.$$

Once the calibration of PA #2 is completed, the results can be duplicated on PA #1—see Table 5.4.

The difference between the values of potentiometer *Pot #1* of PA #1 and that of PA #2 is due to the different built-in maximum value of the resistance. The same applies to potentiometer *Pot #3*.

5.4 Adhesive Installation

As seen in Chapter 4, each of Quasimoro's wheel features a timing-belt TS, whose components are a driving pulley, a driven pulley and a timing belt. This TS is in charge of the torque transmission from the output shaft of the PG to the robot wheel hub.

The driving pulley is re-machined in order to increase the contact surface with the PG output shaft. Also the driven pulley is re-machined in order to produce a threaded surface that would allow the assembly on the threaded hub of the bicycle wheel. Hence, the driven pulley is screwed on the wheel hub. An industrial adhesive is used to prevent the torque commanded by the motor to unscrew the driving pulley from the wheel hub.

5.4.1 Estimated Driven Pulley Torque

Knowing the stall torque of the Quasimoro motors ($T_s = 2.290\,\text{Nm}$), the speed reduction ratio of the Quasimoro PGs ($i_{pg} = 74$), and the speed reduction ratio of the Quasimoro timing-belt transmission ($i_{tb} = 1.18$), one can compute the maximum torque T_{max} acting on the internal diameter of each of the Quasimoro driven pulleys:

$$T_{max} = T_s \frac{D_i}{D_e} i_{tb} i_{pg} = 107.72\,\text{Nm}.$$

With reference to this formula, $D_e = 0.0624\,\text{m}$ and $D_i = 0.0336\,\text{m}$ represent the external diameter and the internal diameter of the driven pulley, respectively.

5.4.2 Threadlocker

The prevailing torque, $T_{p,10}$[9], of the 242, 262 and 271 Loctite® *threadlockers*[10] is reported in Table 5.5 (Loctite, 2005). Although *Prism series instant adhesives* (Loctite, 2005) feature high shear strength (up to $25 \times 10^6\,\text{Pa}$), they are disregarded because they are better suited for bonding prismatic surfaces. Among the three threadlockers

Model Number	*Typical Use*	$T_{p,10}$ [Nm]
242	Removable	380.55
262	High Strength	1681.5
271	Permanent	2212.5

Table 5.5: Threadlocker prevail torques and typical usages

of Table 5.5 we select the 271 because of the nominal diameter of our application ($D_i = 0.0336\,\text{m} > 0.0250\,\text{m}$). The 242 and 262 are generally used for fasteners of nominal diameter smaller than $3/4'' = 0.0195\,\text{m}$, while the 271 is used for locking larger bolts (M25 and higher). Adopting a linear interpolation technique one can compute the prevailing torque for a D_i diameter as:

$$T_{p,D_i} = \frac{T_p D_i}{10} = 7434\,\text{Nm} >> T_{max} = 107.72\,\text{Nm}.$$

The linear approximation by T_{p,D_i} being almost 70 times T_{max}.

[9] Computed for M10 steel nuts and bolts and tested according to ISO 10964.

[10] "Threadlockers are used to prevent fasteners loosening in situations of vibration and thermal cycling." (Loctite, 2005).

5.4.3 Adhesive-based Assembly of the Driven Pulley and Wheel Hub

In this Subsection we describe the procedure for assembling the Quasimoro driven pulley and wheel hub. The equipment required for this procedure is listed below:

- Loctite threadlocker 271 (adhesive).
- Loctite N-primer 7649 (the primer speeds up the cure time of the adhesive).
- Isopropyl rubbing alcohol, micro-fiber cloth (for grease removal), and a non-metallic brush.

Goggles, latex disposable gloves and lab overall should be used in order to protect eyes and skin from the adhesive primer.

The procedure entails four steps, namely,

1) Clean throughout the threads on the mating surfaces by using cloth and alcohol. Visible dirt (grease spots) can be removed with the brush.

2) Secure the wheel to a test-bench in a vertical position and apply the primer to the wheel threads only.

3) Apply the adhesive to the threads of the wheel hub only.

4) Assemble the driven-pulley as fast as possible[11].

The procedure is initially performed on the left driving unit and then, after the test-bench motion experiment success (see Section 6.2), it is performed on the right driving unit. By doing so we first make sure that one driving unit is fully functional before performing the adhesive installation on the other driving unit of the robot.

[11] The Loctite 271 being an anaerobic adhesive, the torque necessary to secure the driven timing pulley on the wheel hub thread will increase, during the assembly, with the number of screwing rotations.

5.5 Calibration of the Robot Drive System

Several techniques are available in the literature for properly installing and pretensioning a timing-belt TS. However, most timing-belt applications often exhibit their own individual operating characteristics. The static installation tensions recommended in manufacturer catalogs serve *only* as general guidelines in determining the level of tension required (SDP/SI Inc., 2005). The drive system needs to be throughly tested to confirm that it performs as intended.

5.5.1 Static Belt Tension

The role of the belt-installation tension T_{st}, also known as static installation tension, is to allow the belt to maintain a proper fit with the pulleys while under load, and to prevent belt ratcheting under peak loads. For the 0.005 m-pitch $GT2$ belt featuring a 0.009 m width, the minimum installation tension is $T_{st,min} = 37.36\,\mathrm{Nm}$ per span, while a typical value is $T_{st,typ} = 80.07\,\mathrm{N}$ per span (SDP/SI Inc., 2005). However, T_{st} can also be predicted as outlined below.

If the Quasimoro motors are stalled, their output torque is (Maxon Precision Motors, Inc., 2003)

$$\tau_{stall} = 2.290\,\mathrm{Nm}.$$

By transporting this torque to the driving pulley we have

$$\tau_{stall,dp} = i_{pg}\tau_{stall} = 169.46\,\mathrm{Nm}$$

where $i_{pg} = 74$ is the speed reduction ratio of the Quasimoro PGs. Further, according to a conservative assumption, the static value of the belt tension, T_{st}, can be estimated using formula (SDP/SI Inc., 2005)

$$T_{st} = \frac{1.05\tau_{stall,dp}}{d} + m\left(\frac{s}{1000}\right)^2 = 739.33\,\mathrm{lb} = 3289\,\mathrm{N}, \tag{5.1}$$

where s is the belt speed[12] (which is zero because the motor is stalled), $d = 0.0541\,\mathrm{m}$

[12]The belt speed can be estimated as the product of the pitch diameter of the driving pulley and the speed of the driving pulley.

is the pitch diameter of the driving pulley, and $m = 0.170$ is the mass factor (SDP/SI Inc., 2005).

5.5.2 Force/Deflection Method

Belt-span tension can be measured by deflecting a belt span 1/64″ per inch (0.0004 m per 0.025 m) of span length at midspan, with a known force. This method, named force/deflection method, is generally convenient, but not always very accurate, due to difficulty in measuring small deflections and forces common in timing-belt TSs with short span lengths (SDP/SI Inc., 2005). However, the force/deflection method is most effective on TSs with long span lengths like those of Quasimoro.

The deflection force minimum and maximum values can be predicted using the formulas (SDP/SI Inc., 2005)

$$F_{min}^{pred} = \frac{T_{st} + \frac{t_{pred}}{L} Y}{16} \tag{5.2}$$

$$F_{max}^{pred} = \frac{1.1 T_{st} + \frac{t_{pred}}{L} Y}{16} \tag{5.3}$$

where

- t_{pred} is the predicted value of the belt span length,
- $Y = 14.9$ (SDP/SI Inc., 2005) is a constant dependent on the timing belt characteristics, and
- $L = 0.650$ m is the pitch length of Quasimoro timing belts (SDP/SI Inc., 2005).

The value of the span length can be predicted using the following formula

$$t_{pred} = \sqrt{D_{cd} - \left(\frac{D - d}{2}\right)^2} = 7.67 \times 10^{-2}\text{m} \tag{5.4}$$

where

- $D_{cd} = 232 \times 10^{-3}$ m is Quasimoro's timing pulley centre distance[13],

[13] `http://www.sdp-si.com/Cd/default.htm`

- $D = 0.0637\,\mathrm{m}$ is the pitch diameter of the driven pulleys (SDP/SI Inc., 2005) and

- $d = 0.0541\,\mathrm{m}$ is the pitch diameter of the driving pulleys (SDP/SI Inc., 2005).

5.5.3 Experiments

In order to properly set the tension of Quasimoro's timing belts, a calibrated weight F is tightened to the middle point of the timing-belt span, P_{span}, by means of a nylon rope. P_{span} lies in between tooth #21 and #22. The *actual* deflection measured in P_{span}, indicated by d_{act}, is caliper-measured.

In order to set-up the experiments, the *actual* timing-belt span is measured: $t_{act} = 9.055'' = 0.230\,\mathrm{m}$. Hence, the maximum and minimum values of the deflection force, F^{act}_{min} and F^{act}_{max} are estimated using t_{act}. The results are shown in Table 5.6. For

T_{st}	T_{st}[N]	F^{pred}_{min}[N]	F^{pred}_{max}[N]	F^{act}_{min}[N]	F^{act}_{max}[N]
From eq. (5.1)	3289	205.95	226.50	206.93	227.48
Typical value ($T_{st,typ}$)	80.07	5.47	6.00	6.45	6.98
Minimum value ($T_{st,min}$)	37.36	2.82	3.06	3.78	4.05

Table 5.6: Quasimoro's static belt tension

example, the minimum value of the deflection force is computed as follows:

$$F^{act}_{min} = \frac{T_{st} + (t_{act}/L)Y}{16} = \frac{T_{st} + 5.2724}{16}.$$

The same applies to the values of F^{act}_{max}. The expected maximum deflection is $d_{max} = t_{act}/64'' = 0.1415'' = 0.0036\,\mathrm{m}$. Adopting a conservative approach, the experiments are performed using F^{act}_{max} as a reference. Another conservative approach consists in choosing the first weight-wise commercially available calibrated weight F *greater* than F^{act}_{max} (i.e. for $F^{act}_{max} = 4.05\,\mathrm{N}$, we select $F = 1\,\mathrm{lb} = 4.45\,\mathrm{N}$; for $F^{act}_{max} = 6.98\,\mathrm{N}$, we select $F = 2\,\mathrm{lb} = 8.90\,\mathrm{N}$ and so on).

As seen from the results of experiment #1, the minimum value of T_{st}, $T_{st,min}$, is not achieved because the actual deflection is greater than the maximum: $d_{act} > d_{max}$, see Table 5.7[14]. Therefore, the experiment #2 is performed by increasing the belt tension. However, the results of experiment #2 are not satisfactory either (as we can see from Table 5.7 $d_{act} > d_{max}$). Therefore, in order to further increase the belt

Experiment	F[N]	d_{act}[m]	N
#1	$4.45(T_{st} = T_{st,min})$	$0.0069 > d_{max}$	1
#2	$4.45(T_{st} = T_{st,min})$	$0.0051 > d_{max}$	1
#3	$4.45(T_{st} = T_{st,min})$	$0.0032 < d_{max}$	2
#4	$8.90(T_{st} = T_{st,typ})$	$0.0054 > d_{max}$	2

Table 5.7: Experimental results — timing-belt re-tightening

tension, experiment #3 is conducted, where the belt tightening involves two people.

Experiment #3 is satisfactory because: $d_{act} < d$. Hence, no further tension increase is recommended. The reason behind this decision is linked to the maximum permissible radial load. In fact, by running experiment #4, with the same *actual* tension of experiment #3 (i.e. without further increasing the belt tension) and with $F = 8.90\,\mathrm{N}$ $(T_{st} = T_{st,typ})$, we have $d_{act} = 0.0054\,\mathrm{m} > d_{max}$. Therefore, the *actual* belt tension is $T_{st,min} < T_{st,act} < T_{st,typ}$, and is also smaller than the maximum permissible radial load of the output shaft of the Quasimoro PG (Maxon Precision Motors, Inc., 2003)

$$T_{st,act} < R_{max,perm} = 150\,\mathrm{N}. \tag{5.5}$$

However, even if the inequality (5.5) is satisfied, we have to keep in mind that a higher belt tension will load the PG bearings, thus increasing their wear. For this reason, we do not tighten further the belt.

As shown in Section 6.2, tightening the belt between the minimum and typical values of T_{st} successfully prevents the system from ratcheting even when the motors are stalled.

[14] N is the number of people required in order to tension the belt.

5.6 Robot Programming

Quasimoro's on-board computer is a $PC/104$ CPU board from LiPPERT, namely, a Cool Road-Runner II (LiPPERT Automationstechnik Gmb, 2001). The robot can be accessed by the user (username: `quasimoro`) and by the robot administrator/manufacturer (username: `root`). The access to the robot can be: *i*) remote/wired *ii*) remote/wireless or *iii*) direct/wired. The user can generally operate the robot by *ii*), while *i*) and *iii*) are used by the robot administrator/manufacturer for maintenance purposes.

5.6.1 Direct/Wired

In the direct/wired communication mode with the robot, the $PC/104$ computer board can be either powered by an AT—*not* ATX—power supply or by the robot battery packs and the $PC/104$ power supply board. It might happen that the first solution (AT power supply) does not provide exactly 12 V, the voltage requirement at the the $PC/104$ computer board floppy connector. In this regard, it is noteworthy that the floppy connector accepts a power signal ranging from 10.8 V to 13 V.

In order to establish a direct/wired communication with Quasimoro, the robot administrator should connect a PC keyboard, a PC monitor and a PC mouse to the $PC/104$ computer board.

5.6.2 Remote/Wireless

None of the manufacturer drivers of the PCMCIA 3115 $PC/104$ card is used in setting-up the wireless connection of Quasimoro. The wireless specifications of Quasimoro are given in Table 5.8. The user can establish remote/wireless communication with

hostname	*quasimoro.cim.mcgill.ca*
IP address	132.206.72.38
Media Access Control (MAC) address	00022$DA9EFE$4

Table 5.8: Quasimoro wireless specifications

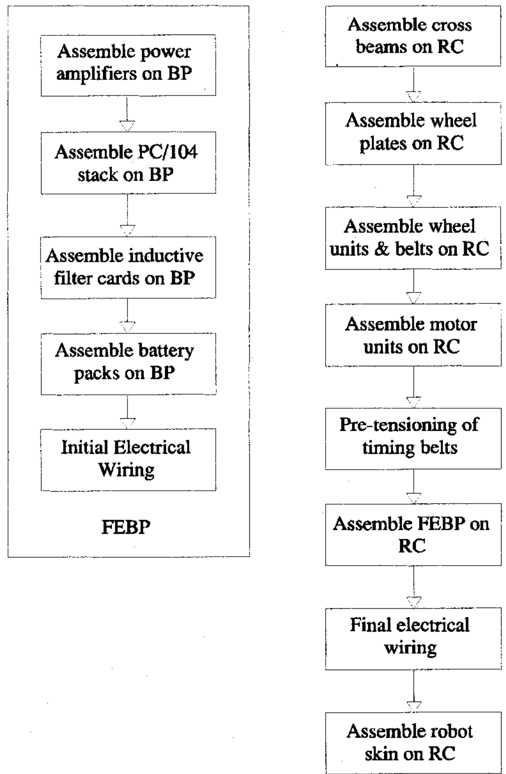

Figure 5.4: Robot component assembly sequence

the robot by using a PC and an access point. We recall that Quasimoro is meant to be used as a test-bed for conducting research on how to improve the living conditions of wheelchair users. In this regard, the robot will operate in a laboratory environment that resembles the living quarters of a mobility-challenged subject.

5.7 Robot Assembly

The assembly sequence of Quasimoro's components is provided in Fig. 5.4. The motor unit consists of motor mount, driving pulley, motor, gearhead and encoder. The wheel unit consists of a bicycle wheel and a driven timing pulley. A series of spacers is installed on the wheel axle so that the distance between the midplanes of driven pulley and wheel plate is given by

$$0.0297\,\mathrm{m} + \frac{(w_{dp} + w_{wp})}{2} \quad [\mathrm{m}],$$

where w_{dp} and w_{wp} are the width of the Quasimoro driven pulley and of Quasimoro wheel plate, respectively.

One of the key issues in the assembly of timing-belt TSs is the initial allignment of the drive components. More specifically, pulley allignment is a necessary procedure for a proper operation of these systems. The person in charge of the robot assembly needs to make sure, by means of a caliper, that the distances of the two pulleys (driving and driven) with respect to a common reference planar surface (such as a level-calibrated test-bench) are equal.

In Fig. 5.4, we also include the assembly sequence of the fully equipped base plate (FEBP), i.e. the robot base plate (BP) ready to assembled on the robot chassis (RC).

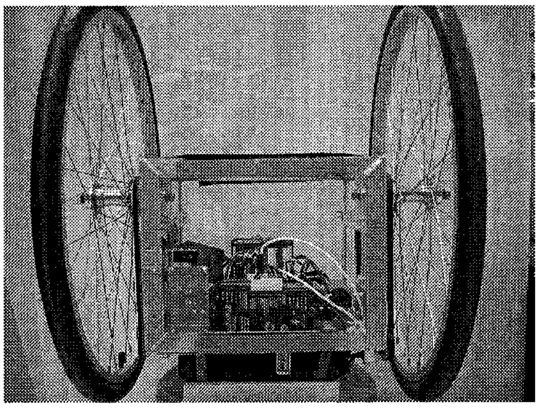

(a)

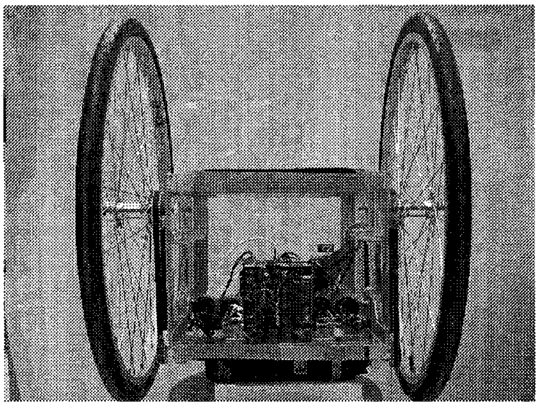

(b)

Figure 5.5: Fully integrated prototype (a) front view; (b) back view

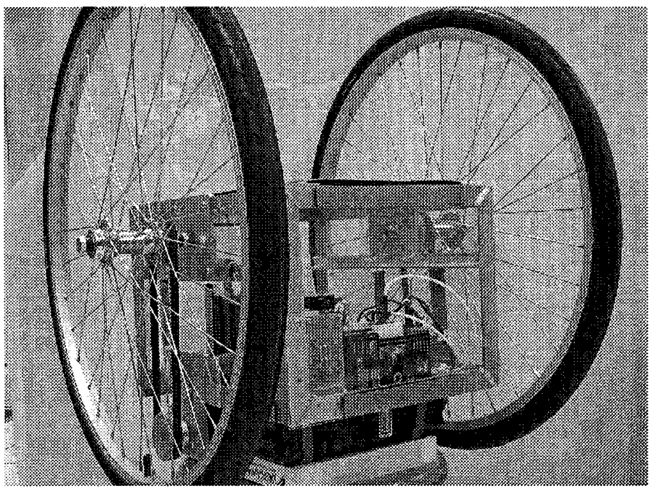

Figure 5.6: Prospective view — fully-integrated prototype

The robot skin consists of nine 8.2×10^{-4} m-thick custom-made panels of Lexan™[15].

5.8 Fully-Integrated Prototype

After having followed the assembly instructions and having coded drivers and control algorithms we can proceed with the wiring and interfacing of the electronic boards of the robot. The resulting system is included in Figs. 5.5–5.6.

[15] `http://www.geplastics.com`

Chapter 6

Experimental Results

6.1 Power Switch

Experiments are performed in order to *i*) verify the functionality of the power switch under different load conditions and *ii*) validate the design reported in Section 4.5. To this end, a *protoboard*, namely, a solderless breadboard (Horowitz and Hill, 1989), is populated with all electronic components of Table 6.1 according to the layout of Fig. 4.10. The input-voltage signal $V_{in} = 30.59\,\mathrm{V}$ is generated by means of a *Dual Tracking DC-Power Supply 6302A* from *Topward*. The measurements are performed using a *digital multi-meter DMM175* from *Fluke*.

Symbol	**Part Number** (Digi-Key Corp.)	**Description**
J3	CH812-ND	rocker switch
R1	TBH25P2K70J-ND	resistor
R2	311-150KATR-ND	resistor
Q1	ZTX453-ND	PNP transistor
Q2	ZTX553-ND	NPN transistor
Q3, Q4	IRFP150N-ND	N-Channel MOSFET
D1	SMAZ5V6DICT-ND	Zener diode
D2	ES1DDICT-ND	Fast Rectifier

Table 6.1: Power switch—bill of materials

Load:	180 kΩ		1.5 kΩ		180 Ω	
Measurement:	V_{out} [V]	R_{ds} [Ω]	V_{out} [V]	R_{ds} [Ω]	V_{out} [V]	R_{ds} [Ω]
J3 closed:	30.59	0.20	30.59	0.80	30.59	N/A
J3 open:	0.00	∞	0.00	∞	0.00	N/A

Table 6.2: Experiments on the power switch under different loads

6.1.1 Experiments with Different Loading Conditions

With the purpose of testing power switch functionality, different resistive loads are applied to the output terminals of the power switch. The results obtained are shown in Table 6.2. In this Table, V_{out} represents the output voltage, i.e. the voltage measured at the output terminals of the power switch, while R_{ds} indicates the drain-to-source resistance of MOSFETs Q3 and Q4.

The measured values of R_{ds} suggest that the MOSFETs turn on as soon as J3 is closed, as one should have expected. Hence, $V_{out} = V_{in}$ since the switched ground signal equals the ground signal. It is also possible to observe that when J3 is open, the MOSFETs provide an infinite drain-to-source resistance. Therefore, V_{out} goes to zero because the switched ground voltage equals V_{in}.

6.1.2 Comparison of Simulation and Experimental Results

Experiments under no-load condition are conducted using the solderless breadboard. The results are compared with those obtained from simulation runs in Table 6.3[1]. Simulation results match experimental data except for the value of V_{out} when J3 is open. The underlined values of Table 6.3 do not match because of the following assumption used to derive the simulated model of the power circuit: the capacitance of the MOSFETs has been neglected.

[1]Both experiments and simulation runs return: $V_{g1s1} = V_{g2s2}$, $V_{g1d1} = V_{g2d2}$ and $V_{d1s1} = V_{d2s2}$.

Simulation	J3 closed	J3 open	**Experiment**	J3 closed	J3 open
V_{out} [V]	30.59	<u>30.59</u>	V_{out} [V]	30.61	<u>0.10</u>
V_{c1b1} [V]	25.54	30.59	V_{c1b1} [V]	25.28	30.17
V_{c2b2} [V]	−5.05	0.00	V_{c2b2} [V]	−5.33	0.00
V_{R2} [V]	5.05	0.00	V_{R2} [V]	5.33	0.00
V_{R1} [V]	25.54	0.00	V_{R1} [V]	25.28	0.00
V_{c2e2} [V]	−5.27	−0.24	V_{c2e2} [V]	−4.92	−0.02
V_{g1s1} [V]	5.27	0.24	V_{g1s1} [V]	4.92	0.03
V_{c1e1} [V]	25.32	30.35	V_{c1e1} [V]	24.83	30.15
V_{g1d1} [V]	5.27	0.24	V_{g1d1} [V]	4.92	0.01
V_{d1s1} [V]	0.00	0.00	V_{d1s1} [V]	0.00	0.01

Table 6.3: Results obtained under no-load and based on IRFP150N MOSFETs—comparison between simulations and experiments

6.2 Test-Bench Motion Experiment

The test-bench motion experiment is intended to test *i*) the robot electrical system; *ii*) the adhesive performance; *iii*) the belt tension (ratcheting, PG bearing grip, etc.); and *iv*) the robot in stall condition. The experiments described in this section are also useful to monitor the motor current under loading conditions.

6.2.1 Set-Up

In order to set-up the experiment, a few steps are taken:

- Install motor #2 along with its IFC and PA.
- Install the left wheel on the robot chassis (after having performed the adhesive-based assembly, see Subsection 5.4.3). Do not install the right wheel yet.
- Install the robot power switch and wire it to the PA and IFC.
- Clamp the robot chassis on a test bench; the robot needs to be clamped upside down in order to test the effect the gravity under accidental full swing of the IB.

- Use a function generator to supply a step signal of 0-10 V to the negative reference pin, namely $REF-$[2], of the robot PA and to provide a common ground to the negative terminal of the battery, the positive reference pin, $REF+$, and ground pin, *SIGNAL GND*, of the robot PA.

- Connect the robot battery packs in series (black connector on red connector) and install them on the robot chassis.

- Use an oscilloscope along with a current probe in order to monitor the motor current.

- Use cable-ties in order to prevent the robot wiring from moving under the gravity.

- Without connecting the signal cable of the PA to the function generator, connect the battery terminals to the power switch. The PA LED should not light up. However, as soon as the robot power switch is turned ON the PA LED should light up displaying a faulty condition (red LED).

- Turn OFF the robot power switch and disconnect the positive connector of the robot battery from the power switch.

- The output signal of the function generator is set to produce a step signal of 0-10 V amplitude. This is extremely important for the proper operation of Quasimoro since the $MPC550$ $PC104$ outputs exactly a control analog signal in the 0-10 V range.

- Connect $REF+$, $SIGNALGND$ and $INHIBIT$ pins of the PA to the function generator ground terminal.

- Connect the current probe to the positive terminal of the motor.

[2]This allows us to test the adhesive performance: the robot left wheel will in fact rotate in the unscrewing direction of the driven pulley.

- Connect the battery return to the ground of the function generator.
- Connect the positive (negative) terminal of the battery to the positive (negative) terminal of the power switch.
- Connect the negative reference pin of the PA to the output of the function generator. As a consequence of this, the robot wheels start rotating.

6.2.2 Results

After having completed the set-up, one can proceed with the testing. Gently turn the potentiometer of the function generator in such a way to increase the step output signal amplitude from 0 to 10 V. Correspondingly, the motor current (read at the current probe) will increase from 0 to 4 A, thus not exceeding the motor maximum continuous current value of 6 A (Maxon Precision Motors, Inc., 2003). One might think naively that the maximum current that the motor will continuously draw is 6A, see Section 5.3. However, in this experiment we observe a motor continuous current of 4 A. At this point it is important to recall that the motor current depends on motor speed, back-electromotive force (back-emf) and passive forces (introduced by the belt transmission). In this regard, the 6 A measured during PA calibration is not anymore valid as a reference.

If we try to stop the wheel by applying a braking force (e.g. by clamping our hands on the wheel tire), the wheel will stop even with the maximum command signal of 10 V. Ratcheting is not experienced during the braking of the wheel (even by applying a sudden intermittent stop).

Several experiments on the RDS, such as intermittent start/stop and continuous motion, are performed. Throughout these experiments, the current probe readout never exceeds 4 A. However, ratcheting is experienced when a 10 V step is suddenly assigned to the wheel, which is initially at rest. This is no surprise; it is always wise to gradually increase the motor torque instead of *instantaneously* assign a value of 2/3 of the maximum continuous current to the wheel which is initially at rest. It is also noteworthy that in stalled conditions the motor never reaches the stall current. In fact, the 4 A threshold, mainly dictated by the built-in current limitation of the PA, is never exceeded.

After having successfully performed the test-bench motion experiment, we proceed with the installation of the adhesive for the right wheel of the robot, see Section 5.4. The robot motion control experiments, which represent the final step of the experimental validation, are then carried out.

6.3 Motion Control Experiments

Before carrying out the motion control experiments, we set a fixed voltage at the robot controller and then check the signal at the amplifier with an oscilloscope to make sure that the signal is noise-free.

6.3.1 Preliminary Tests

The fully assembled robot, without payload, is secured on a stool. The power switch is then turned ON. As a consequence of this,

- Quasimoro's control unit power supply green LED turns ON, thus confirming that the robot control unit is successfully powered up;
- both Quasimoro's MPC550 green and red LEDs turns ON, thus confirming that the robot data acquisition card is operational; and
- PA red LEDs turns ON, thus confirming that they are ready to be enabled as soon as the robot super-user issues such a request.

After a few seconds, the red active Quasimoro wireless board LED (the one far from the PCMCIA slot) starts blinking for a few times and one of the green LEDs of the wireless card turns ON, thus confirming connectivity of the robot with the wireless access point. In order to verify such a connectivity,

- log-in onto one of the McGill University's Centre for Intelligent Machines (CIM) PCs;
- connect by the secure shell protocol, SSH[3], to `citrine.cim.mcgill.ca` as `quasimoro` user; and
- issue the command `ping quasimoro` and observe the data transfer report: no data loss is observed, all the packages from/to the robot are successfully sent/received.

Below we report the program file names along with a description:

- `test_1`: enabling/disabling robot power amplifiers;
- `test_2`: request of spinning the wheels in the same direction;
- `test_3`: request of spinning the wheels in opposite directions;
- `test_4`: request of spinning the wheels in the same direction (by applying a torque that is twice that of `test_2`);
- `test5`: request of spinning the wheels in opposite directions (by applying a torque that is twice that of `test3`).

From the PC, we launch the control algorithm `test_1`. As a consequence of this, both LEDs of Quasimoro's PAs switch from red (PAs disabled) to green (PAs enabled); after a few seconds, they return to their default disabled state, following the pre-programmed instructions.

We then launch the control algorithm `test_2`. This enables the robot PAs; after a few seconds the algorithm induces the wheels to rotate synchronously in the same direction. The wheels then stop and the PAs are disabled.

Algorithms `test_3`, `test_4` and `test_5` are then launched and performed with success one after the other.

[3] `http://www.putty.nl/`

Confident of the success of the preliminary tests we proceed to the motion control experiments.

6.3.2 Control Scheme

The control algorithm used for the experiments outlined below is purely open-loop and sensorless[4]. This allows the roboticist to better appreciate the control simplifications introduced by the design for quasiholonomy.

The command signals are sent to the robot on-board controller from a desktop PC through wireless communication. The reference signals are the torques to be assigned to the robot motors.

Real-Time Control

The robot is programmed to operate *interactively* with the user. More specifically, the user can command the robot, by executing the program files listed in Table 6.4. Quasimoro is also programmed to stop and to be remotely turned ON and OFF.

Program file name	Description
f	Perform a forward motion
b	Perform a backward motion
r	Perform a CW rotation
l	Perform a CCW rotation
s	Stop robot motion
on	Enable the robot motion capabilities
off	Disable the robot motion capabilities

Table 6.4: Quasimoro real-time control program files

The robot user can remotely control Quasimoro in navigating through a cluttered environment. To substantiate this claim, an experiment is run. The user controls the robot while sitting on a wheelchair. The robot successfully avoids three obstacles in order to reach the user position. The user teleoperates the robot using the real-time commands recorded in Table 6.4.

[4]The only feedback signal used in the robot control is the motor current used to close the control feedback loop of the power amplifier.

As we can see from the sequence depicted in Fig. 6.1, the robot successfully achieves the task. The task is accomplished in less than 60 s.

Figure 6.1: Quasimoro navigating through a cluttered environment

Pre-Programmed Control

Quasimoro can also be controlled according to a pre-programmed control strategy. In order to substantiate this claim two experiments are run.

In the first experiment the robot is commanded to follow a straight line. To this end, the user orders the robot to perform the `rectilinear_motion` control algorithm. After an initial overshoot, mainly due to the reaction torque, the IB tilt angle is stabilized to zero, as depicted in Fig. 6.2. Furthermore, the robot remains within a 1 m-wide rectilinear path during the motion (Salerno and Angeles, 2006).

Quasimoro average speed, during this experiment is 2.1 m/s. The robot is capable of even higher speeds. As a matter of fact, the system could benefit of a maximum continuous motor torque that is five times the one used in this experiment (Salerno and Angeles, 2006). Therefore, Quasimoro is a fast robot.

The deviation of the robot motion with respect to a pure rectilinear motion is due to micro-slippage of the wheels.

In the second experiment the robot is commanded to perform a rotation in place. To this end, the user orders the robot to perform the control algorithm `rotation`. As described in Fig. 6.3, the IB tilt angle remains approximately equal to zero during the motion (the reaction torque on the IB being zero in principle). Moreover, the robot remains within its footprint (Salerno and Angeles, 2006).

During this experiment the average rotational speed of the robot is 4.32 rad/s. The average rotational speed could be increased further. From Fig. 6.2 and 6.3 we can infer that the robot successfully achieves the given tasks.

6.3.3 Application-Driven Validation

Quasimoro is a mobile robot for wheelchair-user augmentation. In order to substantiate this claim, an experiment is run. The custom-made PH is installed on the robot. The robot is then loaded with the following items: two books, a bottle of water and two meals. The user remotely commands the robot to bring him the items.

The system accomplish the task in less than seven seconds. Moreover, the maximum overshoot before the stabilization of the IB does not exceed 30°. As we can see from the sequence depicted in Fig. 6.4, the robot successfully achieves the task.

6.3.4 Downhill Motion

In order to analyze the robot behaviour under gravity, a suitable experiment is run: The robot is left to roll downhill, under no control, according to the parameters below:

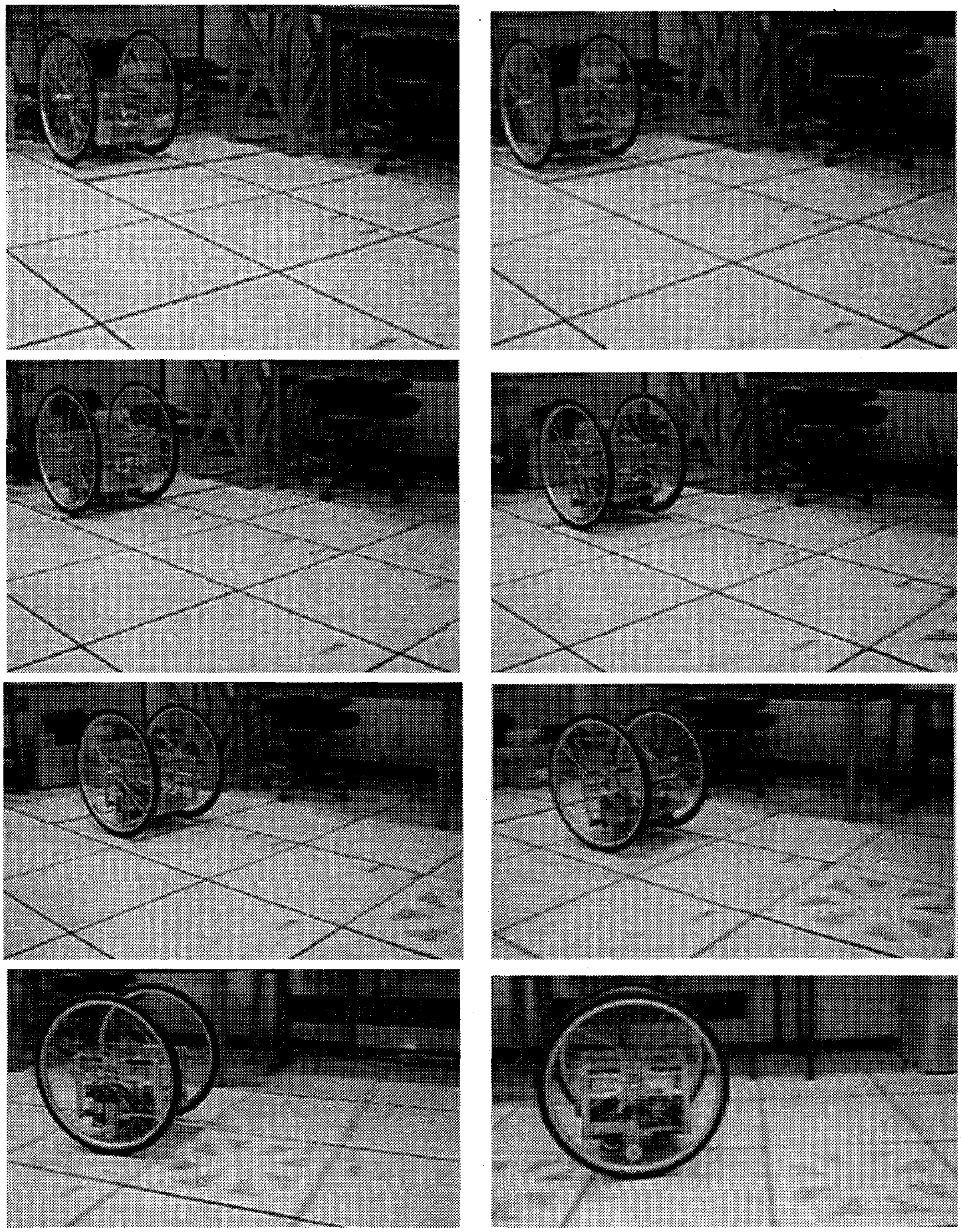

Figure 6.2: Quasimoro rectilinear motion experiment

- a negative 15%-slope
- height of 0.290 m

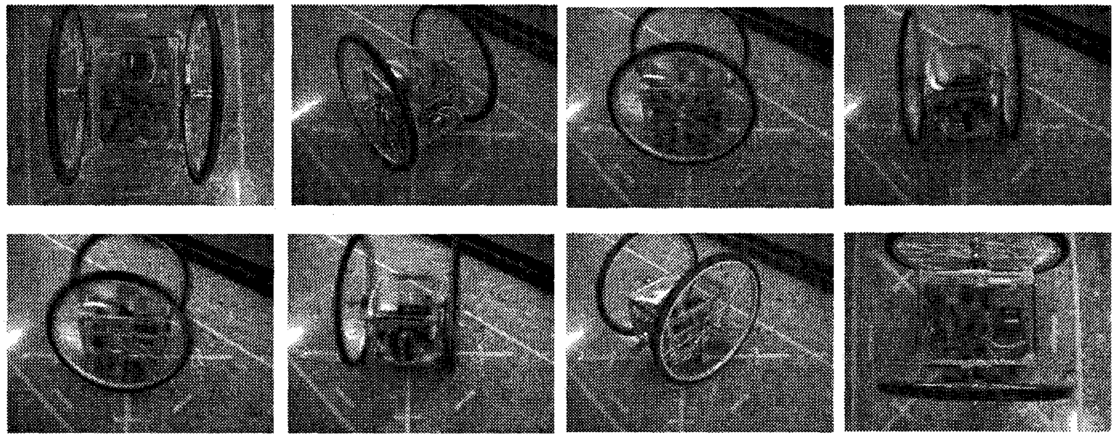

Figure 6.3: Quasimoro rotation in place experiment

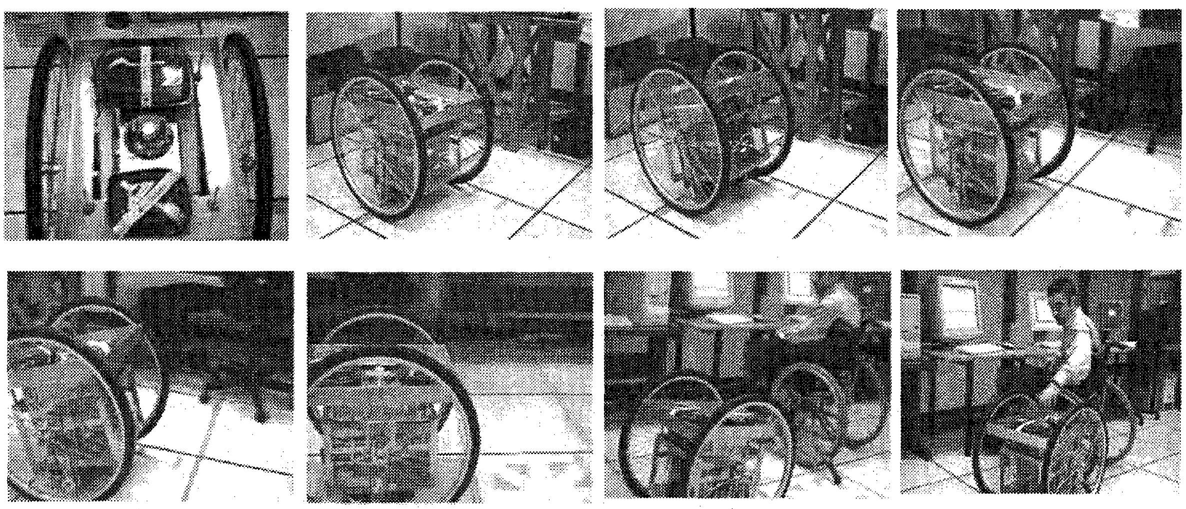

Figure 6.4: Quasimoro application experiment

- span of 1.860 m and
- an initial velocity equal to zero.

The experiment shows that the time traveled by the robot while on the slope is 1 s.

6.3.5 Impact Analysis

The prototype successfully withstands the maximum payload condition without reaching mechanical failure. Further, to verify the strength of the wheel shafts under impact, few motion experiments are also run. The prototype successfully withstands wall-impacts at a cruising speed of $2\,\mathrm{m/s}$.

The experiments described in this Section, rely *only* on the built-in current sensor of the robot PAs[5]. The oscillations of the IB are successfully dampened by the RDS without having to resort to the use of tilt sensor, incremental encoders and LQR control algorithm. In light of this, the robot control is strongly simplified.

[5]This sensor is used by the internal current loop of the Quasimoro PAs (Advanced Motion Controls, 2004c).

Chapter 7

Concluding Remarks

7.1 Conclusions

The problem of designing and controlling a quasiholnomic two-wheeled mobile robot for wheelchair-user augmentation was studied and successfully solved using both theory and experiments.

The conceptual design of the robot was conducted. A proof that quasiholonomy simplifies the computed-torque control of nonholonomic systems was provided. Guidelines on quasiholonomic robot design were also proposed. The dynamics of the robot at hand was derived according to the Lagrange formalism by means of modern concepts such as quasiholonomy and the holonomy matrix. The controllability analysis of the system was then undertaken. In this regard, it was also proven that two-wheeled quasiholonomic mobile robots are both locally accessible and small-time locally controllable.

The embodiment design, detail design, prototyping and experimental tests were then described. A novel robot drive system, based on the use of a timing-belt transmission, a bicycle wheel and adhesive, was designed, calibrated and tested. It was proven that Quasimoro, the robot under study, exhibits a performance that is acceptable even without feedback control or any device for electronic stabilization of the IB. It was also proven that Quasimoro achieves speeds higher than 2 m/s. Furthermore, it was shown that the system is capable of path-following while carrying and stabilizing the payload.

7.2 Recommendations for Further Research

The effect of toe and camber angles on low-speed vehicles by inserting wedges between wheel plate and robot chassis should be investigated. The effect of caster wheels on the robot positioning accuracy should also be investigated.

At high speeds it might be interesting to find out when the use of a dynamics model-based control algorithm is preferred over its purely kinematic counterpart.

In order to further investigate the positioning accuracy and repeatability of the proposed prototype, other sensors might be added. In this regard, the robot is already supplied with a tilt sensor (Crossbow Technology, Inc., 2004), two incremental encoders (Maxon Precision Motors, Inc., 2003) and a PC/104 quadrature/decoder board (Microcomputer Systems, Inc., 2004). Other types of sensors might be added, such as range finding and vision systems, that would further increase the robot autonomy.

To further examine other ways of simplifying the robot user interface, the use of a frequency modulation (FM) remote-controller, e.g., the $6YG$ six-channel FM system (Futaba Corp., 2003) can be considered. More specifically, the on-board timers/counters of Quasimoro data acquisition card, namely, the MPC550, can be used in order to interface the FM receiver with the CPU board. Voice control and personal digital assistant (PDA) control should also be considered.

Finally, a detailed parametric mathematical model of the overall system should be formulated, with the purpose of finding the optimum design variables for fastest, most accurate performance and lowest-cost production and maintenance. This optimization task can be accomplished using a multidisciplinary approach.

Bibliography

ActivMedia Robotics, LLC (2001). *Pioneer 2 PeopleBot^{TM}*. Manual, Version 9.

Advanced Motion Controls (2004a). *AMC Amplifiers—Installation Notes*. Section G—Engineering Reference.

Advanced Motion Controls (2004b). *AMC Inductive Filter Cards*. Datasheet.

Advanced Motion Controls (2004c). *AMC Series 25A8 Servo Amplifiers*. Datasheet.

Aghili, F. (1997). *Design and Control of Direct-Drive Systems*. Ph.D. Thesis, Department of Mechanical Engineering, McGill University, Montreal.

Angeles, J. (1992). The design of isotropic manipulator architectures in the presence of redundancies. *Int. J. Robotics Research* 11(3):196–200.

Angeles, J. (2003). *Fundamentals of Robotic Mechanical Systems: Theory, Methods, and Algorithms*. 2nd ed., Springer-Verlag, New York, NY.

Angeles, J., Ranjbaran, F., and Patel, R. (1992). On the design of the kinematic structure of seven-axes redundant manipulators for maximum conditioning. In *IEEE Proc. Int. Conf. Robotics and Automation*, Nice, France.

Applied AI Systems, Inc. (2000). *Labo-3*. Datasheet.

Asada, H. (1982). A geometrical representation of manipulation, dynamics and its application to arm design. In *Robotics Research and Advanced Applications*, W. J. Book, (Ed.), ASME, New York, NY.

Asada, H. and Youcef-Toumi, K. (1987). *Direct-Drive Robots: Theory and Practice*. The MIT Press, Cambridge, MA.

Åström, K. J. and Wittenmark, B. (1997). *Computer-Controlled Systems: Theory and Design*. Prentice Hall, Upper Saddle River, NJ.

Batavia, P. H. and Nourbakhsh, I. (2000). Path planning for the Cye personal robot. In *Proc. IEEE/RSJ Int. Conf. Intelligent Robots and Systems*, Takamatsu, Japan.

Bischoff, R. and Graefe, V. (2003). HERMES—An intelligent humanoid robot designed and tested for dependability. In *Experimental Robotics VIII, STAR 5*, B. Siciliano and P. Dario, (Eds.), Springer-Verlag, New York, NY.

Bloch, A. M. (2003). *Nonholonomic Mechanics and Control*. Springer-Verlag, New York, NY.

Bloch, A. M., Reyhanoglu, M., and McClamroch, N. H. (1992). Control and stabilization of nonholonomic dynamic systems. *IEEE Trans. Automatic Control* 37(11):1746–1757.

Bolles, R. C. and Roth, B. (1988). Part II: Devices. In *Robotics Research: The Fourth International Symposium*, P. Winston and M. Brady, (Eds), the MIT Press, Cambridge, MA.

Bolmsjö, G., Neveryd, H., and Eftring, H. (1995). Robotics in rehabilitation. *IEEE Trans. Rehabilitation Engineering* 3(1):77–83.

Borenstein, J. and Ulrich, I. (1997). The GuideCane—A computerized travel aid for the active guidance of blind pedestrians. In *Proc. IEEE Int. Conf. Robotics and Automation.*, Albuquerque, NM.

Bräul, T. (2003). *Embedded Robotics: Mobile robot design and applications with embedded systems*. Springer-Verlag, New York, NY.

Briand, A., Fraize, G., Milles, P., and Rouyer, J. L. (1987). Eureka: Advanced mobile robots for public safety applications. In *Proc. Remote Systems and Robotics in Hostile Environments—International Topical Meeting*, Pasco, WA.

Campbell, D. (2004). *Bounding and Stair Descent in the Hexapod RHex*. M.Eng. Thesis, Department of Electrical and Computer Engineering, McGill University, Montreal.

Campion, G., Bastin, G., and d'Andrea-Novel, B. (1991). Modelling and state feedback control of nonholonomic mechanical systems. In *Proc. IEEE 30th Conf. Decision and Control*, Brighton, England.

Campion, G., Bastin, G., and d'Andrea-Novel, B. (1996). Structural properties and classification of kinematic and dynamic models of wheeled mobile robots. *IEEE Trans. Robotics and Automation* 12(1):47–62.

Canadian Centre for Justice (2001). *Canadians with Disabilities*. Authority of the Minister responsible for Statistics Canada, Ottawa, ON.

Cavallo, A., Setola, R., and Vasca, F. (1996). *Using Matlab, Simulink and Control System Toolbox. A practical approach*. Prentice Hall, Englewood Cliffs, NJ.

Chen, C. T. (1999). *Linear System Theory and Design*. Oxford University Press, New York, NY.

Clement, C. and Villedieu, E. (1987). Surveyor—Mobile surveillance system for hazardous environments. In *Proc. Remote Systems and Robotics in Hostile Environments — International Topical Meeting*, Pasco, WA.

Cook, A. M. and Hussey, S. M. (2002). *Assistive Technologies: Principles and Practice*. Mosby, St. Louis, MO.

Cortés Monforte, J. (2002). *Geometric, Control and Numerical Aspects of Nonholonomic Systems*. Springer-Verlag, New York, NY.

Critchlow, A. J. (1985). *Introduction to Robotics*. MacMillan Publishing Company, New York, NY.

Crossbow Technology, Inc. (2004). *Solid-State Analog Series Tilt Sensors CXTA01*. Datasheet.

d'Andrea-Novel, B., Bastin, G., and Campion, G. (1992). Dynamic feedback linearization of nonholonomic wheeled mobile robots. In *Proc. IEEE Int. Conf. Robotics and Automation*, Nice, France.

Daniali, H. M., Zsombor-Murray, P., and Angeles, J. (1994). Isotropic design of spherical parallel manipulators. In *Proc. ASME Advances in Design and Automation*, New York, NY.

De Luca, A. and Oriolo, G. (1995). Modelling and control of nonholonomic mechanical systems. In *Kinematics and Dynamics of Multibody Systems*, J. Angeles and A. Kecskemethy, (Eds.), Springer-Verlag, Wien, Austria.

De Luca, A. and Oriolo, G. (2000). Motion planning and trajectory control of an underactuated three-link robot via dynamic feedback linearization. In *Proc. IEEE Int. Conf. Robotics and Automation*, San Francisco, CA.

Dote, Y. and Kinoshita, S. (1990). *Brushless Servomotors: Fundamentals and Applications*. Clarendon Press, Oxford, UK.

Drenner, A., Burt, I., Dahlin, T., Kratochvil, B., McMillen, C., Nelson, B., Rybski, N. P. P., Stubbs, K., Waletzko, D., and Berk Yesin, K. (2002). Mobility enhancements to the Scout robot platform. In *Proc. IEEE Int. Conf. Robotics and Automation*, Washington DC.

Dudek, D. and Jenkin, M. (2000). *Computational Principles of Mobile Robotics*. Cambridge University Press, Cambridge, UK.

Dudley, D. (1962). *Gear Handbook: the Design, Manufacture, and Application of Gears*. McGraw-Hill, New York, NY.

Dunlop, G. R. (2003). Design for a large walking delta robot. In *Experimental Robotics VIII, STAR 5*, B. Siciliano and P. Dario, (Eds.), Springer-Verlag, New York, NY.

Environment Department (2001). *Disability Access Guide*. Newham Council, London, England.

ESCWA (2003). *Accessibility for the Disabled—A Design Manual for a Barrier Free Environment*. United Nations, New York, NY.

FAO (2001). *Press release PR 01/94—Disability is only a consequence of poverty*. Food and Agriculture Organization of the United Nations, Chief Publishing Management Service, Rome, Italy.

Fenner Drives (2004). *Urethane O-Ring*. Datasheet.

Fiorini, P., Ali, K., and Seraji, H. (1997). Health care robotics: A progress report. In *Proc. IEEE Int. Conf. Robotics and Automation*, Albaquerque, NM.

Fisette, P., Ferriére, L., Raucent, B., and Vaneghem, B. (2000). A multibody approach for modelling universal wheels of mobile robots. *Mechanism and Machine Theory* 35:329–351.

Fraquelli, E. (1935). Gyro-wheel car zooms along on giant tires at 116 mph. *Modern Mechanix and Inventions* 14:43.

Frederikse, H. P. R. and Lide, D. (1996). *CRC Handbook of Chemistry and Physics*. 76th ed., CRC Press, Cleveland, OH.

Futaba Corp. (2003). *6YG-FM Six-Channel Radio Control System*. User's Manual.

Gieras, J. F. and Wing, M. (1997). *Permanent Magnet Motor Technology: Design and Applications*. Marcel Dekker, New York, NY.

Girardin, P. (1994). *La Domotique*. Sociéte d'habitation du Québec, Sainte-Foy, QC, original in French.

Giuffrida, F., Morasso, P., and Zaccaria, R. (1998). PARTNER—a semi-autonomous mobile service robot in a wireless network for biomedical applications. In *Proc. Technology for Inclusive Design and Equality (TIDE) Congress*, Helsinki, Finland.

Golub, G. H. and Van Loan, C. F. (1996). *Matrix Computations*. Johns Hopkins University Press, Baltimore, MD.

González-Palacios, M. and Angeles, J. (1999). The design of a novel mechanical transmission for speed reduction. *ASME Journal of Mechanical Design* 121(4):538–543.

Goris, K. (2005). *Autonomous Mobile Robot: Mechanical Design.* M.Eng. Thesis, Department of Mechanical Engineering, *Vrije Universiteit Brussel,* Brussels, Belgium.

Gosselin, C. (1992). The optimum design of robotic manipulators using dexterity indices. *Journal of Robotics and Autonomous Systems* 9(4):213–226.

Gosselin, C. and Angeles, J. (1991). A global performance index for the kinematic optimization of robotic manipulators. *ASME Journal of Mechanical Design* 113:220–226.

Grasser, F., D'Arrigo, A., Colombi, S., and Rufer, A. C. (2002). Joe: A mobile, inverted pendulum. *IEEE Trans. Industrial Electronics* 49(1):107–114.

Guglielmelli, E., Goodwin, M., Mulè, C., and Dario, P. (1994). A supervisory system for the URMAD robotic unit. In *Proc. IEEE Int. Conf. Intelligent Robots and Systems*, Munich, Germany.

Guru, B. and Hiziroglu, H. (2001). *Electric Machinery and Transformers*. Oxford University Press, New York, NY.

Hada, Y. and Yuta, S. (2000). A first-stage experiment of long term activity of autonomous mobile robot—Result of repetitive base-docking over a week. In *Experimental Robotics VII*, D. Rus and S. Singh, (Eds.), Springer-Verlag, New York, NY.

Hagihara, S., Maeda, Y., and Tsutani, S. (1987). Multifunctional robot vehicle MRV-3. In *Proc. Remote Systems and Robotics in Hostile Environments—International Topical Meeting*, Pasco, WA.

HAKKO (2006). *HAKKO Solder/Desolder Stations*. Catalog (Techni-Tool).

Heinzmann GmbH (2004). *E-Bikes Standardmotoren (Hub-Motors).* Online Catalog, original in German.

Hill, B. M. (1997). *Design of Mechanical Properties for Serial Manipulators*. Ph.D. Thesis, Department of Mechanical Engineering, The University of Texas at Austin, Austin, TX.

Hirata, Y., Kosuge, K., Asama, H., Kaetsu, H., and Kawabata, K. (2000). Motion control of distributed robot helpers transporting a single object in cooperation with a human. In *Experimental Robotics VII*, D. Rus and S. Singh, (Eds.), Springer-Verlag, New York, NY.

Hollerbach, J. M. (1985). Optimum kinematic design for a seven degree of freedom manipulator. In *Robotics Research: The Second International Symposium*, H. Hanafusa and H. Inoue (Eds.), The MIT Press, Cambridge, MA.

Hollerbach, J. M. and Sahar, G. (1984). Wrist-partitioned inverse kinematic accelerations and manipulator dynamics. In *Proc. IEEE Int. Conf. Robotics*, Atlanta, GA.

Holzbock, W. G. (1986). *Robotic Technology, Principles and Practice*. Van Nostrand Reinhold Company, New York, NY.

Hong, D., Velinski, S. A., and Feng, X. (1999). Verification of a wheeled mobile robot dynamic model and control ratifications. *ASME J. Dynamic Systems, Measurement, and Control* 121(1):58–63.

Hoppenot, P. and Cole, E. (2001). Localization and control of a rehabilitation mobile robot by close human-machine interaction. *IEEE Trans. Neural Systems and Rehabilitation Engineering* 9(2):181–190.

Hoppenot, P., Colle, E., Aider, O. A., and Rybarczyk, Y. (2001). Arph—Assistant robot for handicapped people. In *Proc. IEEE 10th Int. Workshop on Robot and Human Interactive Communication*, Bordeaux and Paris, France.

Horowitz, P. and Hill, W. (1989). *The Art of Electronics*. 2nd ed., Cambridge University Press, Cambridge, England.

Iagnemma, K., Golda, D., Spenko, M., and Dubowsky, S. (2003). Experimental study of high-speed rough-terrain mobile robot models for reactive behaviors. In *Experimental Robotics VIII, STAR 5*, B. Siciliano and P. Dario (Eds.), Springer-Verlag, New York, NY.

International Rectifier (2005a). *110CNQ045A Schottky Rectifier—D-61 Package 110Amp*. Datasheet.

International Rectifier (2005b). *120NQ Series—Schottky Rectifier 120Amp*. Datasheet.

International Rectifier (2005c). *IRF4905 HEXFET—Power MOSFET*. Datasheet.

iRobot™ Corp. (2002). *Roomba Intelligent FloorVac*. Owner's Manual.

Isidori, A. (1989). *Nonlinear Control Systems: An Introduction*. Springer-Verlag, New York, NY.

Jacobsen, S., Smith, C. C., Biggers, K. B., and Iversen, E. K. (1988). Behavior based design of robot effectors. In *Robotics Research: The Fourth International Symposium*, P. Winston and M. Brady (Eds.), The MIT Press, Cambridge, MA.

Jeong, K. W., Chung, W., and Youm, Y. (1990). Development of postech 7-dof direct drive robot. In *Robotics and Manufacturing*, M. Jamshidi and M. Saif (Eds.), ASME Press, New York, NY.

Juvinall, R. C. and Marshek, K. M. (2006). *Fundamentals of machine component design*. 4th ed., John Wiley & Sons, Hoboken, NJ.

Kamen, D. J., Ambrogi, R. R., Duggan, R. J., Field, D. J., Heinzmann, R. K., Amsbury, B., and Langenfeld, C. C. (2000). Personal mobility vehicles and methods. Patent, PCT/US00/15144.

Kanehira, M., Otani, T., Yoshikawa, M., and Takahashi, T. (2005). *The Complete Guide to Chain*. Tsubakimoto Chain Co., Osaka, Japan.

Kawakami, A., Torii, A., Motomura, K., and Hirose, S. (2003). SMC rover: Planetary rover with transformable wheels. In *Experimental Robotics VIII, STAR 5*, B. Siciliano and P. Dario, (Eds.), Springer-Verlag, New York, NY.

Keafter, R. D. (1988). Mobile robots, research and development. In *International Encyclopedia of Robotics*, R. C. Dorf (Ed.), A Wiley-Interscience Publication, New York, NY.

Khosla, P. K. (1987). Choosing sampling rates for robot control. In *Proc. IEEE Int. Conf. Robotics and Automation*, San Francisco, CA.

Klafter, R. D., Chmielewski, T. A., and Negin, M. (1989). *Robotic Engineering: An Integrated Approach*. Prentice Hall, Englewood Cliffs, N.J.

Kraus, L., Stoddard, S., and Gilmartin, D. (1996). *Chartbook on Disability in the United States*. InfoUse, Berkeley, CA.

Krten, R. (1999). *Getting started with QNX Neutrino 2 : a guide for realtime programmers*. PARSE Software Devices, Kanata, ON.

Kuang, Z. et al. (1997). *Development of a Robotic Manipulator To Assist Disabled Children*. Gateway Coalition, Philadelphia, PA.

Larin, V. B. (2000). Control of manipulators and wheeled transport robots as systems of rigid bodies. *Int. Applied Mechanics* 36(4):449–480.

Leahy, M. B., Valavanis, K. P., and Saridis, G. N. (1986). The design of a mobile robot for instrument network deployment in Antarctica. In *Proc. IEEE Int. Conf. Robotics and Automation*, San Francisco, CA.

Leow, Y. (2002). *Kinematic Modeling, Mobility Analysis and Design of Wheeled Mobile Robots*. M.Eng. Thesis, Department of Mechanical Engineering, Nanyang Technological University, Singapore.

Lewis, A. D. (2000). Simple mechanical control systems with constraints. *IEEE Trans. Automatic Control* 45(8):1420–1436.

Linden, D. (2002). *Handbook of Batteries*. McGraw-Hill Handbooks, New York; McGraw-Hill.

LiPPERT Automationstechnik Gmb (2001). *Cool RoadRunner II—All-in-one PC/104-Plus CPU Board*. Technical Manual, Version 1.6.

Liu, G. and Li, Z. (2002). A unified geometric approach to modeling and control of constrained mechanical systems. *IEEE Trans. Robotics and Automation* 18(4):574–587.

Loctite (2005). *Loctite Threadlockers*. Catalog (Techni-Tool).

Ma, O. and Angeles, J. (1993). Optimum design of manipulators under dynamic isotropy conditions. In *Proc. IEEE Int. Conf. Robotics and Automation*, Atlanta, GA.

Mächler, P. (1998). *Robot Positioning by Supervised and Unsupervised Odometry Correction*. Lausanne, Switzerland: Ph.D. Thesis, *Départment d'Informatique, Ecole Polytechnique Fédérale de Lausanne*, Lausanne, Switzerland.

Maggi, G. (1901). Di alcune nuove forme delle equazioni della dinamica applicabili ai sistemi anolonomi (On some novel formulations of the equations of motions for nonholonomic systems). *Atti Accad. Naz. Lincei Rend Cl. Fis. Mat. Nat.* 10(5):287–291, original in Italian.

Markiewicz, B. R. (1973). Analysis of the computed torque drive method and comparison with conventional position servo for a computer-controlled manipulator. Technical Memorandum, NASA-CR-131521, JPL-TM-33-601, Jet Propulsion Laboratory, Pasadena, CA.

Martin, T. P., Byrd, J. S., and Fisher, J. J. (1987). Mobile robots in research and development programs at the Savannah River laboratory. In *Proc. Remote Systems and Robotics in Hostile Environments—International Topical Meeting*, Pasco, WA.

Maxon Precision Motor, Inc. (2002). *RE 40* ϕ40 mm*, Graphite Brushes,* 150 W *(Order number: 148867)*. April edition, maxon Precision Motors 02/03 Catalogue.

Maxon Precision Motors, Inc. (2003). *Maxon Precision Motors*. Catalog.

McAree, P., Samuel, A., Hunt, K., and Gibson, C. (1991). A dexterity measure for the kinematic control of a multifinger, multifreedom robot hand. *Int. J. Robotics Research* 10(5):439–453.

McMordie, D. (2002). *Towards Pronking with a hexapod robot*. M.Eng. Thesis, Department of Electrical and Computer Engineering, McGill University, Montreal.

Microcomputer Systems, Inc. (2004). *MSI-P400 PC/104 Quadrature Decoder/Counter Card*. Reference Manual.

Micro/Sys, Inc. (1999). *MPC550 Analog/Digital I/O Adapter for PC/104*. Reference Manual.

Neimark, J. I. and Fufaev, N. (1972). *Dynamics of Nonholonomic Systems*. American Mathematical Society, Providence, RI.

Neveryd, H. and Bolmsjö, G. (1995). WALKY, an ultrasonic navigating mobile robot for the disabled. In *Proc. 2nd Technology for Inclusive Design and Equality (TIDE) Congress*, Paris, France.

Nijmeijer, H. and van der Schaft, A. J. (1990). *Nonlinear Dynamical Control Systems*. Springer-Verlag, New York, NY.

Oberg, E., Jones, F. D., and Horton, H. L. (1988). *Machinery's Handbook* 23rd *Edition*. Industrial Press Inc., New York, NY.

O'Halloran, D., Wolf, A., and Choset, H. (2004). Design of a high-impact survivable robot. In *Proc. IEEE Int. Conf. Robotics and Automation*, New Orleans, LA.

Oriolo, G., Panzieri, S., and Ulivi, G. (1998). An iterative learning controller for nonholonomic mobile robots. *Int. J. Robotics Research* 17(9):954–970.

Ostrovskaya, S. (2001). *Dynamics of Quasiholonomic and Nonholonomic Reconfigurable Rolling Robots*. Ph.D. Thesis, Department of Mechanical Engineering, McGill University, Montreal.

Ostrovskaya, S. and Angeles, J. (1998). Nonholonomic systems revisited within the framework of analytical mechanics. *Applied Mechanics Reviews* 51(7):415–433.

Ottaviano, E. and Ceccarelli, M. (2002). Optimum design of parallel manipulators for workspace and singularity performances. In *Proc. Workshop on Fundamentals Issues and Future Research for Parallel Mechanisms and Manipulators*, Quebec City, QC.

Ou, Y. and Tsai, L. (1996). Isotropic design of tendon-driven manipulators. *ASME Journal of Mechanical Design* 118(3):360–366.

Paquin, V. and Cohen, P. (2004). A vision-based gestural guidance interface for mobile robotic platforms. In *Proc. Int. Workshop on Human-Computer Interaction*, Prague, Czech Republic.

Parker Seals (2001). *Parker O-Ring Handbook—ORD 5700A/US790*. Catalog.

Parkin, R. E. (1991). *Applied Robotic Analysis*. Prentice Hall, Englewood Cliffs, NJ.

Pars, L. A. (1979). *A Treatise on Analytical Dynamics*. Ox Bow Press, Woodridge, CT.

Pathak, K., Franch, J., and Agrawal, S. K. (2005). Velocity and position control of a wheeled inverted pendulum by partial feedback linearization. *IEEE Trans. Robotics and Automation* 21(3):505–513.

Paul, R. C. (1972). Modeling trajectory calculation and servoing of a computer controlled arm. Technical Memorandum, A.I. Memo 177, Stanford Artificial Intelligence Laboratory, Stanford University, Stanford, CA.

Poulakakis, I. (2002). *On the Passive Dynamics of Quadrupedal Running*. M.Eng. Thesis, Department of Mechanical Engineering, McGill University, Montreal.

Ray, L., Price, A., Streeter, A., Denton, D., and Lever, J. H. (2005). The design of a mobile robot for instrument network deployment in Antarctica. In *Proc. IEEE Int. Conf. Robotics and Automation*, Barcelona, Spain.

Rico Martinéz, J. M. and Duffy, J. (1998). Robot isotropy: A reassessment. In *Proc. of Sixth Int. Symp. Advances in Robot Kinematics: Analysis and Control*, Strobl, Austria.

Rivin, E. I. (1988). *Mechanical Design of Robots*. McGraw-Hill, New York, NY.

Robosoft (2002). *Robuter III Circular Base*. DataSheet.

Roth, B. (1986). Analytic design of open chains. In *Robotics Research: The Third International Symposium*, O. D. Faugeras and G. Giralt, (Eds.), The MIT Press, Cambridge, MA.

RTD Embedded Technologies (2003). *VPWR104HR PC/104 Vehicle Power Supply*. User's Manual, Revision 1.1.

Saha, S. K., Angeles, J., and Darcovich, J. (1988). The design of kinematically isotropic rolling robots with omnidirectional wheels. *Mechanism and Machine Theory* 30(8):1127–1137.

Saha, S. K., Angeles, J., and Darcovich, J. (1993). The kinematic design of a 3-dof isotropic mobile robot. In *IEEE Proc. Int. Conf. Robotics and Automation*, Atlanta, GA.

Salerno, A. and Angeles, J. (2003a). On the nonlinear controllability of a quasiholonomic mobile robot. In *Proc. IEEE Int. Conf. Robot. Automat.*, Taipei, Taiwan.

Salerno, A. and Angeles, J. (2003b). The preliminary design of a novel robot for human augmentation. In *Proc. CCToMM Symposium on Mechanisms, Machines, and Mechatronics*, St. Hubert, QC.

Salerno, A. and Angeles, J. (2003c). The robust design of a two-wheeled quasiholonomic mobile robot. In *Proc. ASME Design Engineering Technical Conferences*, Chicago, IL.

Salerno, A. and Angeles, J. (2004a). The control of semi-autonomous self-balancing two-wheeled quasiholonomic mobile robots. In *Proc. ROMANSY 15$^{\text{th}}$ CISM-IFToMM Symposium on Robot Design, Dynamics and Control*, Montreal.

Salerno, A. and Angeles, J. (2004b). The control of semi-autonomous two-wheeled robots undergoing large payload-variations. In *Proc. IEEE Int. Conf. Robotics and Automation*, New Orleans, LA.

Salerno, A. and Angeles, J. (2004c). A new family of two-wheeled mobile robots: Modeling and controllability. *IEEE Trans. Robotics* Under review.

Salerno, A. and Angeles, J. (2005). Modeling and controllability of two-wheeled quasi-holonomic robots. Technical Report , TR-CIM 05.06, Department of Mechanical Engineering and Centre for Intelligent Machines, McGill University, Montreal.

Salerno, A. and Angeles, J. (2006). Quasimoro: A novel, simple, quasiholonomic two-wheeled robot. *IEEE/ASME Trans. Mechatronics.* Under review.

Salerno, A., Ostrovskaya, S., and Angeles, J. (2002). The development of quasiholonomic wheeled robots. In *Proc. IEEE Int. Conf. Robotics and Automation*, Washington, DC.

Salerno, A., Ostrovskaya, S., and Angeles, J. (2004a). The dynamics of a novel rolling robot—Analysis and simulation. In *Proc. IFToMM 11^{th} World Congress in Mechanism & Machine Science*, Tianjin, China.

Salerno, A., Perlin, R., and Angeles, J. (2004b). The embodiment design of a two-wheeled self-balancing robot. In *Proc. The Inaugural CDEN Conference*, Montreal, Canada.

Sanyo Group (2004). *HR-D7500 Twicell Sanyo Nichel-Metal Hydride Battery*. Datasheet.

Sciavicco, L. and Siciliano, B. (2000). *Modelling and control of robot manipulators*. Springer, New York, NY.

SDP/SI Inc. (1991). *Handbook of Timing Belts, Chains and Friction Drives—D210*. Stock Drive Products—Sterling Instruments (SDP/SI), Catalog, New Hyde Park, NY.

SDP/SI Inc. (2005). *Handbook of Timing Belts and Pulleys—D265*. Stock Drive Products—Sterling Instruments (SDP/SI), Catalog, New Hyde Park, NY.

Segway Inc. (2005). *Segway^{TM} Human Transporter*. Online Datasheet.

Segway Inc. (2006). *Segway^{TM} Robotic Mobility Platform*. Online Datasheet.

Shekkar, S. (1997). Wheel rolling constraints and slip in mobile robots. In *Proc. IEEE Int. Conf. Robotics and Automation*, Albuquerque, NM.

Siciliano, B. and Dario, P. (2003). In *Experimental Robotics VIII, STAR 5*, B. Siciliano and P. Dario, (Eds.), Springer-Verlag, New York, NY.

Silverman, E. B., Simmons, R. K., Kniazewycz, B. G., Darvish, A. R., and Irving, T. L. (1987). Surveyor—Mobile surveillance system for hazardous environments. In *Remote Systems and Robotics in Hostile Environments—International Topical Meeting*, Pasco, WA.

Skyway Machine, Inc. (2002). *Skyway Wheelchair Wheels*. Online Datasheet.

Slotine, J. J. E. and Li, W. (1991). *Applied Nonlinear Control*. Prentice Hall, Englewood Cliffs, NJ.

Smith, J. A. and Sharf, I. (2005). *Paw Robot*. User's Manual, Version 2.1, Mechatronic Locomotion Laboratory, McGill University.

Statistics Canada (1991). *Health and Activity Limitation Survey (HALS)*. Authority of the Minister responsible for Statistics Canada, Ottawa, ON.

Sussmann, H. J. (1987). A general theorem on local controllability. *SIAM J. Control and Optimization* 25(1):158–194.

Suthakorn, J. and Chirikjian, G. S. (2000). Design and implementation of a new discretely-actuated manipulator. In *Experimental Robotics VII*, D. Rus and S. Singh (Eds.), Springer-Verlag, New York, NY.

Taghirad, H. D. (1997). *Robust Torque Control of Harmonic Drive Systems*. Ph.D. Thesis, Department of Electrical and Computer Engineering, McGill University, Montreal.

Takano, M., Masaki, H., and Sasaki, K. (1986). Concept of total computer-aided design system of robot manipulators. In *Robotics Research: The Third International Symposium*, O. D. Faugeras and G. Giralt, (Eds.), The MIT Press, Cambridge, MA.

Tampa Rubber & Gasket Co., Inc. (2005). *Clear-GO Urethane O-Rings*. Online Datasheet.

Tao, G. and Kokotovic, P. V. (1996). *Adaptive Control of Systems with Actuator and Sensor Nonlinearities*. John Wiley & Sons, Inc., New York, NY.

Tsukagoshi, H., Sasaki, M., Kitagawa, A., and Tanaka, T. (2005). Design of a higher jumping rescue robot with the optimized pneumatic drive. In *Proc. IEEE Int. Conf. Robotics and Automation*, Barcelona, Spain.

U.S. Congress (1988). *Technology-Related Assistance for Individuals with Disabilities Act of 1988*. Public Law 100-407, Washington, DC.

Utz, A. and Cox, W. R. (1997). *Inside Pro/Engineer: the Professional User's Guide to Designing With Pro/ENGINEER*. Onword Press, Santa Fe, NM.

Versalogic Corp. (1997). *PC/104 PCM-3115 PCMCIA Module*. User's Manual.

Villani, L., Natale, C., Siciliano, B., and Canudas de Wit, C. (2000). An experimental study of adaptive force/position control algorithms for an industrial robot. *IEEE Trans. Control Systems Technology* 8(5):777–786.

Viola, E. (1985). *Esercitazioni di Scienza delle Costruzioni (Exercises of Structural Engineering)*. Pitagora Editrice, original in Italian.

Vishay Dale (2001). *IHV High Current Filter Inductors*. Datasheet.

Walker, G. (1999). A DC circuit breaker for an electric vehicle battery pack. In *Proc. Australasian Universities Power Engineering Conference*, Darwin, Australia.

World Health Organization (WHO) (1976). *Document A29/INFDOCI/1*. WHO, Geneva, Switzerland.

Yang, D. C. and Lee, T. (1982). Optimization of manipulator workspace. In *Robotics Research and Advanced Applications*, W. J. Book (Ed.), ASME, New York, NY.

Yang, G., Chen, I. M., Lim, W. K., and Yeo, S. (2001). Kinematic design of modular reconfigurable in-parallel robots. *Autonomous Robots* 10:83–89.

Yoshikawa, T. (1986). Analysis and design of articulated robot arms. In *Robotics Research: The Third International Symposium*, O. D. Faugeras and G. Giralt, (Eds.), the MIT Press, Cambridge, MA.

Appendix A

Representation Details

A.1 State-Space Representation

$$
\begin{aligned}
D_4 &= (2m_3d^2\rho^2K + 2J_3\rho^2K - 2J_1\rho^2K)\cos{x_3}^3 + (-J_2J_1\rho^2 + J_2J_3\rho^2 \\
&\quad +J_2m_3d^2\rho^2)\cos{x_3}^2 + (-2m_3d^2\rho^2K + AK - 2J_3\rho^2K \\
&\quad -KB)\cos x_3 - J_2m_3d^2\rho^2 - J_2J_3\rho^2 + (A-B)J_2 \\
Q_{43} &= -4J_1\rho^4K\sin x_3\cos x_3(m_3d^2 + J_3 - J_1)x_5x_4 \\
&\quad +2J_1\rho^4K\sin x_3\cos x_3(m_3d^2 + J_3 - J_1)x_4^2 \\
&\quad -4K^2\sin x_3\rho^2x_6x_5J_1 + 2m_3^2d^3\sin x_3\rho^2Kg \\
&\quad +2J_1\rho^4K\sin x_3\cos x_3(m_3d^2 + J_3 - J_1)x_5^2 \\
&\quad -2m_3d^2\sin x_3\rho^4K\cos x_3(m_3d^2 + J_3 - J_1)x_5^2 \\
&\quad -2J_3\rho^4\sin x_3K\cos x_3(m_3d^2 + J_3 - J_1)x_4^2 \\
&\quad +4J_3\rho^4\sin x_3K\cos x_3(m_3d^2 + J_3 - J_1)x_5x_4 \\
&\quad -2m_3d^2\sin x_3\rho^4K\cos x_3(m_3d^2 + J_3 - J_1)x_4^2 \\
&\quad -4K^2m_b\rho^2d^2\sin x_3x_4x_6 + 4K^2\sin x_3\rho^2x_6x_5J_3d \\
&\quad +2J_3\rho^2\sin x_3Km_3gd - 2J_1\rho^2Km_3gd\sin x_3 \\
&\quad +4K^2\sin x_3\rho^2x_6x_4J_1 + 4K^2m_3\rho^2d^2\sin x_3x_5x_6 \\
&\quad -2J_3\rho^4\sin x_3K\cos x_3(m_3d^2 + J_3 - J_1)x_5^2 \\
&\quad -4K^2\sin x_3\rho^2x_6x_4J_3 + 4m_3d^2\sin x_3\rho^4K\cos x_3(m_3d^2
\end{aligned}
$$

$$+J_3 - J_1)x_5x_4$$

$$\begin{aligned}
Q_{42} &= m_3\rho^2 d\sin x_3 x_5^2 r K^2 - 2J_1\rho^2 J_2 K\sin x_3 x_6^2 - 2J_3\rho^4 \sin x_3 J_2 m_3 d x_4 x_5 r \\
&\quad +2J_1\rho^4 J_2 m_3 d\sin x_3 x_4 x_5 r + 2J_3\rho^2 \sin x_3 J_2 K x_6^2 - K^2 m_3\rho^2 d\sin x_3 x_4^2 r \\
&\quad +m_3^2\rho^4 d^3 \sin x_3 x_5^2 r J_2 - m_3\rho^4 d\sin x_3 x_5^2 r J_2 J_1 + 2m_3 d^2 \sin x_3 \rho^2 J_2 K x_6^2 \\
&\quad -2m_3^2 d^3 \sin x_3 \rho^4 J_2 x_4 x_5 r + mb^2 d^3 \sin x_3 \rho^4 J_2 x_4^2 r - J_1\rho^4 J_2 m_3 d\sin x_3 x_4^2 r \\
&\quad +m_3\rho^4 d\sin x_3 x_5^2 r J_2 J_3 + J_3\rho^4 \sin x_3 J_2 m_3 d x_4^2 r \\
Q_{41} &= K\rho^2 \sin x_3 \cos x_3 (m_3 d^2 + J_3 - J_1) x_4^2 B - 2m_3^2 d^3 \sin x_3 \rho^2 K g \\
&\quad +2m_3 d^2 \sin x_3 \rho^4 K\cos x_3 (m_3 d^2 + J_3 - J_1) x_5^2 \\
&\quad +2J_3\rho^4 \sin x_3 K\cos x_3 (m_3 d^2 + J_3 - J_1) x_4^2 - 4J_1\rho^4 \sin x_3 K\cos x_3 (m_3 d^2 \\
&\quad +J_3 - J_1) x_5 x_4 + 2m_3 d^2 \sin x_3 \rho^4 K\cos x_3 (m_3 d^2 + J_3 - J_1) x_4^2 \\
&\quad -2J_1\rho^2 \sin x_3 K m_3 g d + 2J_3\rho^4 \sin x_3 K\cos x_3 (m_3 d^2 + J_3 - J_1) x_5^2 \\
&\quad -4m_3 d^2 \sin x_3 \rho^4 K\cos x_3 (m_3 d^2 + J_3 - J_1) x_5 x_4 + K\rho^2 \sin x_3 \cos x_3 (m_3 d^2 \\
&\quad +J_3 - J_1) x_5^2 B + AK m_3 g d\sin x_3 - AK\rho^2 \sin x_3 \cos x_3 (J_3 + m_3 d^2 \\
&\quad -J_1) x_4^2 - AK\rho^2 \sin x_3 \cos x_3 (m_3 d^2 + J_3 - J_1) x_5^2 - K m_3 b g d\sin x_3 B \\
&\quad +2m_3\rho^2 d^2 \sin x_3 x_4 x_6 J_2 B - 2K\rho^2 \sin x_3 \cos x_3 (m_3 d^2 + J_3 - J_1) x_5 x_4 B \\
&\quad -2\sin x_3 \rho^2 x_6 x_4 J_1 J_2 B + 2\sin x_3 \rho^2 x_6 x_4 J_3 J_2 B + 2AJ_2 \sin x_3 \rho^2 x_6 x_4 J_3 \\
&\quad -2AJ_2 \sin x_3 \rho^2 x_6 x_4 J_1 - 2AJ_2 m_3 \rho^2 d^2 \sin x_3 x_5 x_6 \\
&\quad +2AK\rho^2 \sin x_3 \cos x_3 (m_3 d^2 + J_3 - J_1) x_5 x_4 + 2\sin x_3 \rho^2 x_6 x_5 J_1 J_2 B \\
&\quad -2\sin x_3 \rho^2 x_6 x_5 J_3 J_2 B + 2AJ_2 m_3 \rho^2 d^2 \sin x_3 x_4 x_6 \\
&\quad -2AJ_2 \sin x_3 \rho^2 x_6 x_5 J_3 - 2m_3\rho^2 d^2 \sin x_3 x_5 x_6 J_2 B + 2AJ_2 \sin x_3 \rho^2 x_6 x_5 J_1 \\
Q_{40} &= AJ_2 m_3 \rho^2 d\sin x_3 x_4^2 r + m_3\rho^2 d\sin x_3 x_4 x_5 r J_2 B - m_3\rho^2 d\sin x_3 x_5^2 r J_2 B \\
&\quad -m_3\rho^4 d\sin x_3 x_5^2 r J_2 J_3 + 2J_3\rho^4 \sin x_3 J_2 m_3 d x_4 x_5 r + AJ_2 K\sin x_3 x_6^2 \\
&\quad +2m_3^2 d^3 \sin x_3 \rho^4 J_2 x_4 x_5 r - 2J_3\rho^2 \sin x_3 J_2 K x_6^2 - J_3\rho^4 \sin x_3 J_2 m_3 d x_4^2 r \\
&\quad -m_3^2\rho^4 d^3 \sin x_3 x_5^2 r J_2 - 2m_3 d^2 \sin x_3 \rho^2 J_2 K x_6^2 + m_3^2 d^3 \sin x_3 \rho^4 J_2 x_4^2 r \\
&\quad -K\sin x_3 x_6^2 J_2 B - AJ_2 m_3 \rho^2 d\sin x_3 x_4 x_5 r \\
C_4 &= (-2J_1\rho^2 + 2m_3 d^2\rho^2 + 2J_3\rho^2)\cos x_3{}^2 + A - B \\
&\quad -2m_b d^2\rho^2 - 2J_3\rho^2)(-2K^2\cos x_3{}^2 + (A+B)J_2)
\end{aligned}$$

$$
\begin{aligned}
Q_{50} &= -4\sin x_3 \cos x_3 \rho^2 x_6 x_5 J_3 + 4\sin x_3 \cos x_3 \rho^2 x_6 x_4 J_3 + m_3 \rho^2 d \sin x_3 x_4^2 r \\
&\quad -d \sin x_3 m_3 \rho^2 x_5^2 r + 4\sin x_3 \cos x_3 \rho^2 x_6 x_5 J_1 + 4 m_3 \rho^2 d^2 \sin x_3 x_4 x_6 \cos x_3 \\
&\quad -4\sin x_3 \cos x_3 \rho^2 x_6 x_4 J_1 - 4 m_3 \rho^2 d^2 \sin x_3 x_5 x_6 \cos x_3 \\
C_5 &= A - 2J_1 \rho^2 \cos {x_3}^2 - B - 2m_3 d^2 \rho^2 - 2J_3 \rho^2 \\
&\quad +2\cos {x_3}^2 m_3 d^2 \rho^2 + 2\cos {x_3}^2 J_3 \rho^2 \\
D &= -(B + K\cos x_3 + A) \\
Q &= (d m_b g \sin x_3 + 2\sin x_3 \rho^2 \cos x_3 (m_3 d^2 + J_3 \\
&\quad -J_1) x_5 x_4 - \sin x_3 \rho^2 \cos x_3 (m_3 d^2 + J_3 \\
&\quad -J_1) x_5^2 - \sin x_3 \rho^2 \cos x_3 (m_3 d^2 + J_3 - J_1) x_4^2) A \\
&\quad +(d m_3 g \sin x_3 + 2\sin x_3 \rho^2 \cos x_3 (m_3 d^2 \\
&\quad +J_3 - J_1) x_5 x_4 - \sin x_3 \rho^2 \cos x_3 (m_3 d^2 + J_3 - J_1) x_5^2 \\
&\quad -\sin x_3 \rho^2 \cos x_3 (m_3 d^2 + J_3 - J_1) x_4^2) B \\
&\quad +d \sin x_3 m_3 K \cos x_3 \rho^2 x_4^2 r + d \sin x_3 m_3 K \cos x_3 \rho^2 x_5^2 r \\
&\quad -2d \sin x_3 m_3 K \cos x_3 \rho^2 x_4 x_5 r + 2K^2 \cos x_3 \sin(x3) x_6^2 \\
C &= -2K^2 \cos {x_3}^2 + (A + B) J_2
\end{aligned}
$$

A.2 Affine State-Space Form

$$
\begin{aligned}
P_i &\equiv \sum_{j=0}^{3} P_{ij} \cos {x_3}^j \quad \text{with } i = 1, 2, 3, \\
P_{13} &\equiv 2J_1 \rho^4 K \sin x_3 \cos x_3 (m_3 d^2 + J_3 - J_1) x_4^2 - 4K^2 \sin x_3 \rho^2 x_6 x_4 J_3 \\
&\quad -2J_1 \rho^2 K m_3 g d \sin x_3 + 2J_1 \rho^4 K \sin x_3 \cos x_3 (m_3 d^2 + J_3 - J_1) x_5^2 \\
&\quad -2m_3 d^2 \sin x_3 \rho^4 K \cos x_3 (m_3 d^2 + J_3 - J_1) x_5^2 \\
&\quad -4J_1 \rho^4 K \sin x_3 \cos x_3 (m_3 d^2 + J_3 - J_1) x_5 x_4 \\
&\quad -2J_3 \rho^4 \sin x_3 K \cos x_3 (m_3 d^2 + J_3 - J_1) x_4^2 \\
&\quad +4J_3 \rho^4 \sin x_3 K \cos x_3 (m_3 d^2 + J_3 - J_1) x_5 x_4
\end{aligned}
$$

$$
\begin{aligned}
& -2m_3d^2\sin x_3\rho^4K\cos x_3(m_3d^2+J_3-J_1)x_4^2 \\
& +4K^2\sin x_3\rho^2x_6x_5J_3-4K^2\sin x_3\rho^2x_6x_5J_1 \\
& +2J_3\rho^2\sin x_3Km_3gd-4K^2m_3\rho^2d^2\sin x_3x_4x_6 \\
& +4K^2m_3\rho^2d^2\sin x_3x_5x_6+2m_3^2d^3\sin x_3\rho^2Kg \\
& -2J_3\rho^4\sin x_3K\cos x_3(m_3d^2+J_3-J_1)x_5^2 \\
& +4K^2\sin x_3\rho^2x_6x_4J_1+4m_3d^2\sin x_3\rho^4K\cos x_3(m_3d^2 \\
& +J_3-J_1)x_5x_4
\end{aligned}
$$

$$
\begin{aligned}
P_{12} \equiv\; & m_3^2d^3\sin x_3\rho^4J_2x_4^2r+m_3\rho^4d\sin x_3x_5^2rJ_2J_3 \\
& +2J_3\rho^2\sin x_3J_2Kx_6^2-J_1\rho^4J_2m_3d\sin x_3x_4^2r+m_3^2\rho^4d^3\sin x_3x_5^2rJ_2 \\
& +2m_3d^2\sin x_3\rho^2J_2Kx_6^2-m_3\rho^4d\sin x_3x_5^2rJ_2J_1+J_3\rho^4\sin x_3J_2m_3dx_4^2r \\
& -K^2m_3\rho^2d\sin x_3x_4^2r-2J_1\rho^2J_2K\sin x_3x_6^2-2J_3\rho^4\sin x_3J_2m_3dx_4x_5r \\
& +2J_1\rho^4J_2m_3d\sin x_3x_4x_5r+m_3\rho^2d\sin x_3x_5^2rK^2-2m_3^2d^3\sin x_3\rho^4J_2x_4x_5r,
\end{aligned}
$$

$$
\begin{aligned}
P_{11} \equiv\; & 2m_3d^2\sin x_3\rho^4K\cos x_3(m_3d^2+J_3-J_1)x_5^2+2J_3\rho^4\sin x_3K\cos x_3(m_3d^2 \\
& +J_3-J_1)x_4^2-4J_3\rho^4\sin x_3K\cos x_3(m_3d^2+J_3-J_1)x_5x_4 \\
& +2m_3d^2\sin x_3\rho^4K\cos x_3(m_3d^2+J_3-J_1)x_4^2-2J_3\rho^2\sin x_3Km_3gd \\
& -2m_3^2d^3\sin x_3\rho^2Kg+2J_3\rho^4\sin x_3K\cos x_3(m_3d^2+J_3-J_1)x_5^2 \\
& -4m_3d^2\sin x_3\rho^4K\cos x_3(m_3d^2+J_3-J_1)x_5x_4+K\rho^2\sin x_3\cos x_3(m_3d^2 \\
& +J_3-J_1)x_5^2B+K\rho^2\sin x_3\cos x_3(m_3d^2+J_3-J_1)x_4^2B+AKm_3gd\sin x_3 \\
& -Km_3gd\sin x_3B-AK\rho^2\sin x_3\cos x_3(m_3d^2+J_3-J_1)x_4^2 \\
& -AK\rho^2\sin x_3\cos x_3(m_3d^2+J_3-J_1)x_5^2-2K\rho^2\sin x_3\cos x_3(m_3d^2 \\
& +J_3-J_1)x_5x_4B-2\sin x_3\rho^2x_6x_4J_1J_3B+2\sin x_3\rho^2x_6x_4J_3J_2B \\
& +2m_3\rho^2d^2\sin x_3x_4x_6J_2B+2AJ_2\sin x_3\rho^2x_6x_5J_1+2\sin x_3\rho^2x_6x_5J_1J_2B \\
& -2\sin x_3\rho^2x_6x_5J_3J_2B+2AJ_2m_3\rho^2d^2\sin x_3x_4x_6-2AJ_2\sin x_3\rho^2x_6x_5J_3 \\
& +2AJ_2\sin x_3\rho^2x_6x_4J_3-2m_3\rho^2d^2\sin x_3x_5x_6J_2B-2AJ_2\sin x_3\rho^2x_6x_4J_1 \\
& -2AJ_2m_3\rho^2d^2\sin x_3x_5x_6+2AK\rho^2\sin x_3\cos x_3(m_3d^2+J_3-J_1)x_5x_4,
\end{aligned}
$$

$$
\begin{aligned}
P_{10} \equiv\; & m_3\rho^2d\sin x_3x_4x_5rJ_2B+2m_3^2d^3\sin x_3\rho^4J_2x_4x_5r-m_3\rho^2d\sin x_3x_5^2rJ_2B \\
& -m_3\rho^4d\sin x_3x_5^2rJ_2J_3-m_3^2d^3\sin x_3\rho^4J_2x_4^2r-J_3\rho^4\sin x_3J_2m_3dx_4^2r \\
& -mb^2\rho^4d^3\sin x_3x_5^2rJ_2+AJ_2m_3\rho^2d\sin x_3x_4^2r+AJ_2K\sin x_3x_6^2
\end{aligned}
$$

$$
\begin{aligned}
& -AJ_2m_3\rho^2 d\sin x_3x_4x_5r + 2J_3\rho^4\sin x_3J_2m_3dx_4x_5r - K\sin x_3x_6^2J_2B \\
& -2m_3d^2\sin x_3\rho^2J_2Kx_6^2 - 2J_3\rho^2\sin x_3J_2Kx_6^2, \\
S_1 &\equiv S_2 \equiv ((-2J_1\rho^2 + 2m_3d^2\rho^2 + 2J_3\rho^2)\cos x_3{}^2 \\
& +A - B - 2m_3d^2\rho^2 - 2J_3\rho^2)(-2K^2\cos x_3{}^2 + BJ_2 + AJ_2a), \\
P_2 &\equiv -(-2K^2\cos x_3{}^2 + BJ_2 + AJ_2)(4\cos x_3x_6x_4J_3 - 4\cos x_3x_6x_4J_1 \\
& +4\cos x_3m_3d^2x_4x_6 - dm_3x_5^2r - 4\cos x_3x_6x_5J_3 - 4\cos x_3m_3d^2x_5x_6 \\
& +4\cos x_3x_6x_5J_1 + m_3dx_4^2r)\rho^2\sin x_3, \\
P_3 &\equiv (d\sin x_3m_3K\rho^2x_4^2r + d\sin x_3m_3K\rho^2x_5^2r - 2d\sin x_3m_3K\rho^2x_4x_5r \\
& +2K^2\sin x_3x_6^2)\cos x_3 + dAm_3g\sin x_3 - \sin x_3\rho^2\cos x_3(m_3d^2 + J_3 \\
& -J_1)x_5^2B - \sin x_3\rho^2\cos x_3(m_3d^2 + J_3 - J_1)x_5^2A + d\sin x_3Bm_3g \\
& +2\sin x_3\rho^2\cos x_3(m_3d^2 + J_3 - J_1)x_5x_4A + 2\sin x_3\rho^2\cos x_3(m_3d^2 \\
& +J_3 - J_1)x_5x_4B - \sin x_3\rho^2\cos x_3(m_3d^2 + J_3 - J_1)x_4^2B \\
& -\sin x_3\rho^2\cos x_3(m_3d^2 + J_3 - J_1)x_4^2A, \\
S_3 &\equiv -2K^2\cos x_3{}^2 + BJ_2 + AJ_2, \\
A_i &\equiv \sum_{j=0}^{3} A_{ij}\cos x_3{}^j \quad \text{with } i = 1, 2 \\
A_{13} &\equiv A_{23} \equiv -2J_1\rho^2K + 2m_3d^2\rho^2K + 2J_3\rho^2K, \\
A_{12} &\equiv -J_2J_1\rho^2 + K^2 + J_2J_3\rho^2 + J_2m_3d^2\rho^2, \\
A_{22} &\equiv A_{12} - K^2, \\
A_{11} &\equiv A_{21} \equiv -KB - 2J_3\rho^2K - 2m_3d^2\rho^2K + AK, \\
A_{10} &\equiv (-BJ_2 - J_2J_3\rho^2) - J_2m_3d^2\rho^2, \\
A_{20} &\equiv A_{10} + (A + B)J_2, \\
A_3 &\equiv -(K\cos x_3 + B + A), C_1 \equiv C_2 \equiv ((4J_1\rho^2K^2 - 4J_3\rho^2K^2 \\
& -4m_3d^2\rho^2K^2)\cos x_3{}^4 + (2m_3d^2\rho^2AJ_2 - 2J_1\rho^2BJ_2 - 2AK^2 \\
& +2BK^2 + 4J_3\rho^2K^2 + 4m_3d^2\rho^2K^2 - 2J_1\rho^2AJ_2 + 2J_3\rho^2BJ_2 \\
& +2m_3d^2\rho^2BJ_2 + 2J_3\rho^2AJ_2)\cos x_3{}^2 - 2m_3d^2\rho^2BJ_2 + A^2J_2 \\
& -B^2J_2 - 2J_3\rho^2BJ_2 - 2J_3\rho^2AJ_2 - 2m_3d^2\rho^2AJ_2), \\
C_3 &\equiv (BJ_2 + AJ_2 - 2K^2\cos(x3)^2).
\end{aligned}
$$

Appendix B

Assembly Drawings

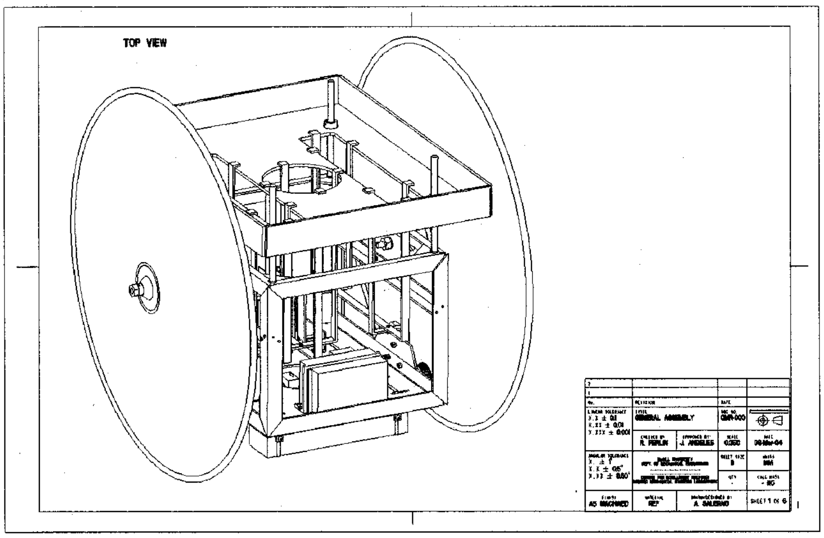

SCALE : 0.350 TYPE : ASSEM NAME : QUASIMORO_5 SIZE : B

Figure B.1: Isometric view of Quasimoro—$\theta_3 = 0\,\text{rad}$

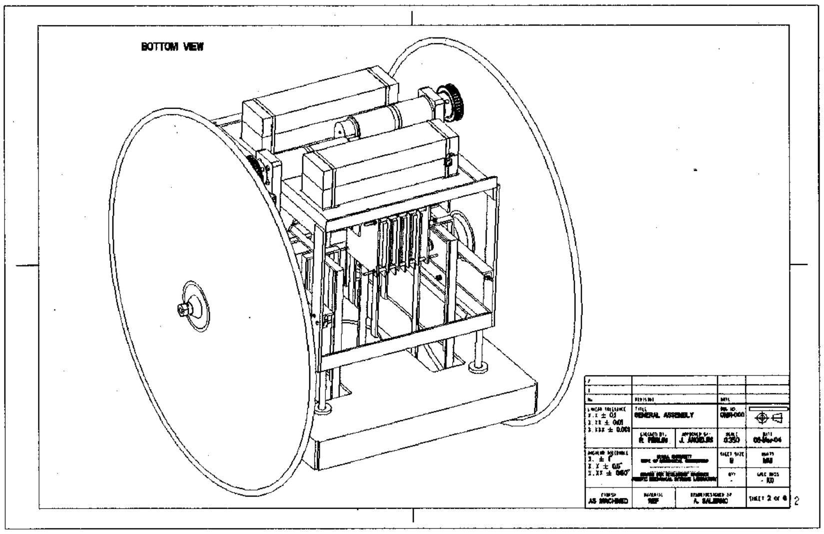

SCALE : 0.350 TYPE : ASSEM NAME : QUASIMORO_5 SIZE : B

Figure B.2: Isometric view of Quasimoro—$\theta_3 = \pm\pi\,\text{rad}$

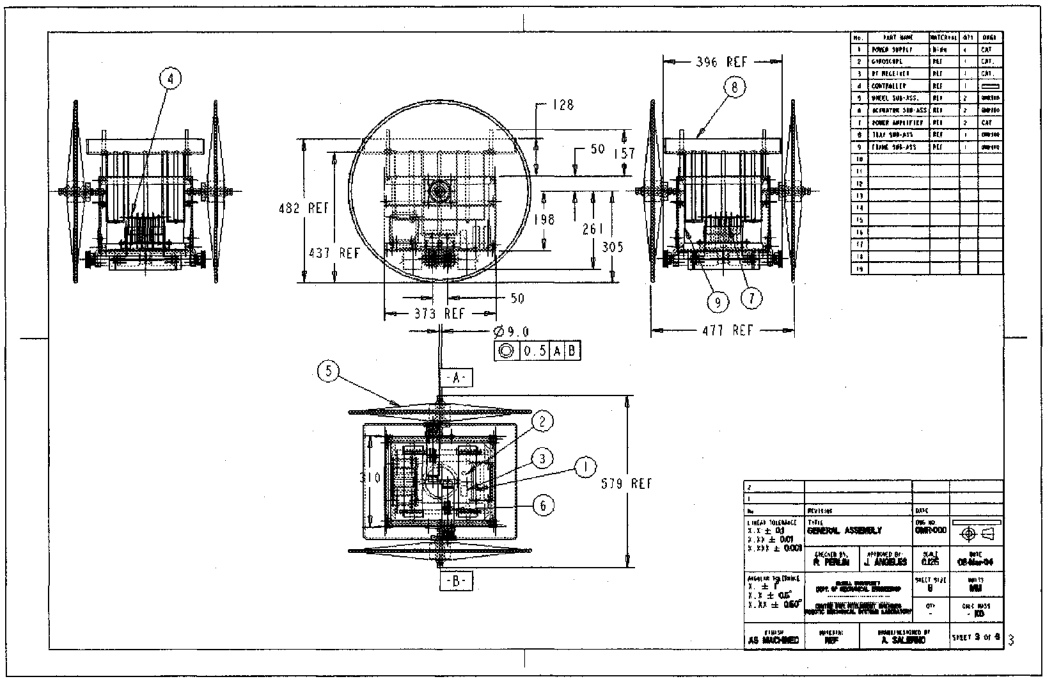

SCALE : 0.125 TYPE : ASSEM NAME : QUASIMORO_5 SIZE : B

Figure B.3: General assembly—multi-views

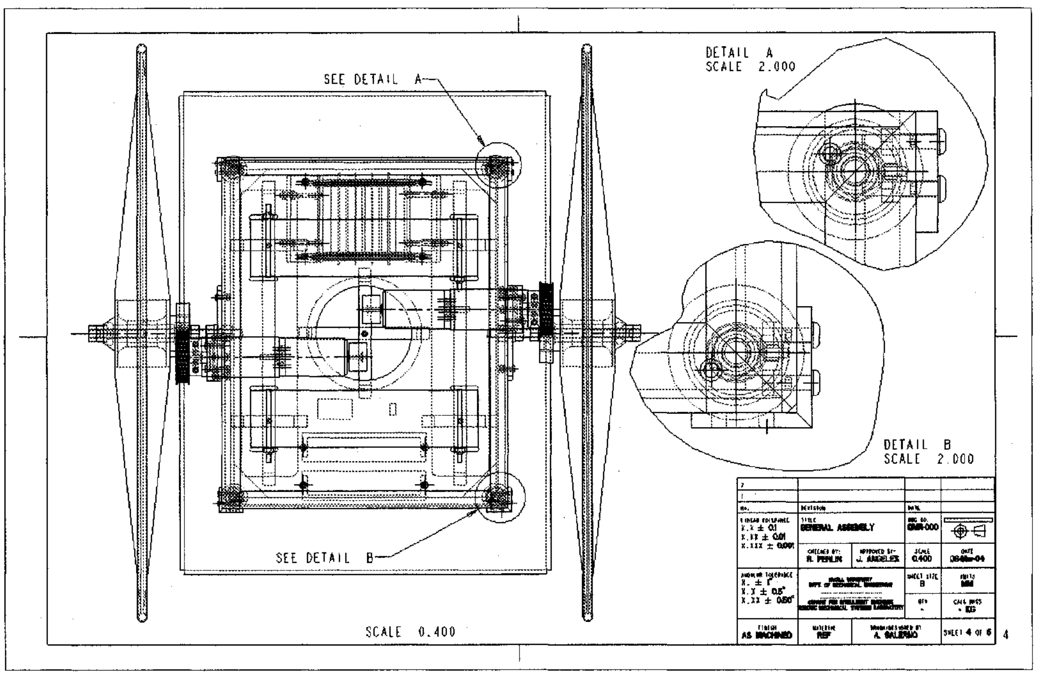

SCALE : 0.400 TYPE : ASSEM NAME : QUASIMORO_5 SIZE : B

Figure B.4: Bottom plate assembly details

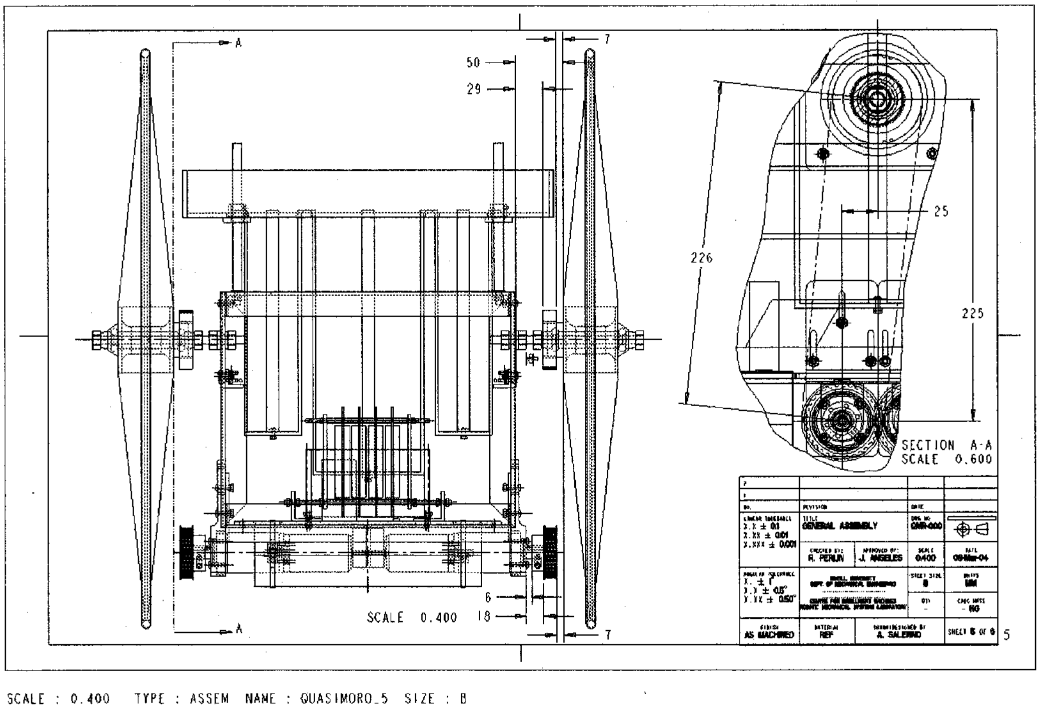

Figure B.5: Robot drive system assembly details

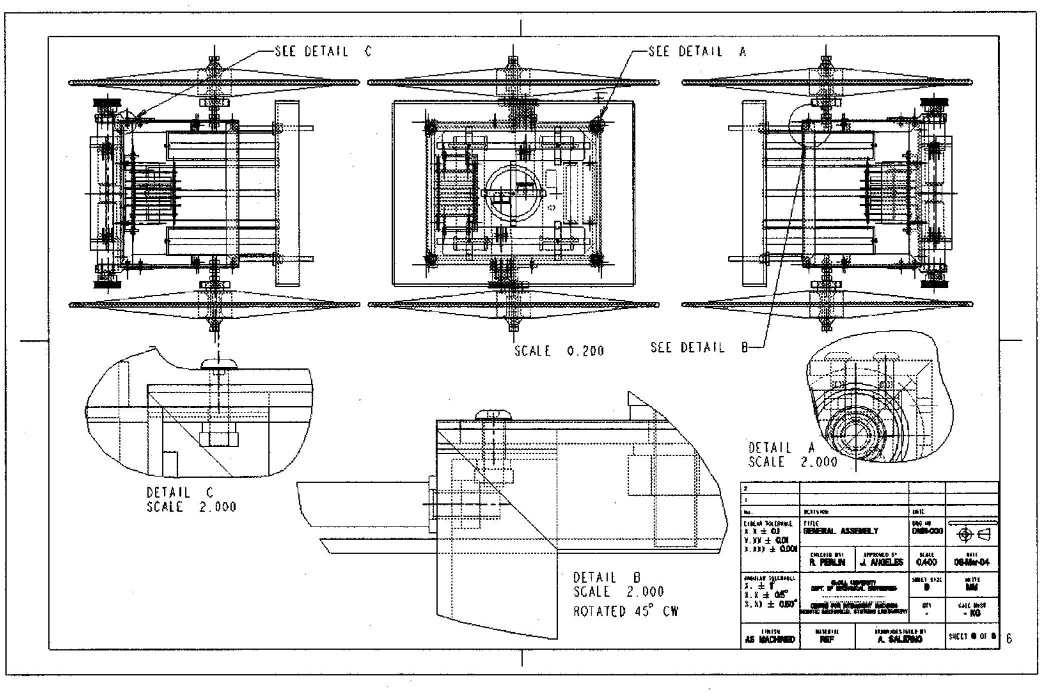

Figure B.6: Motor mount and payload holder assembly details

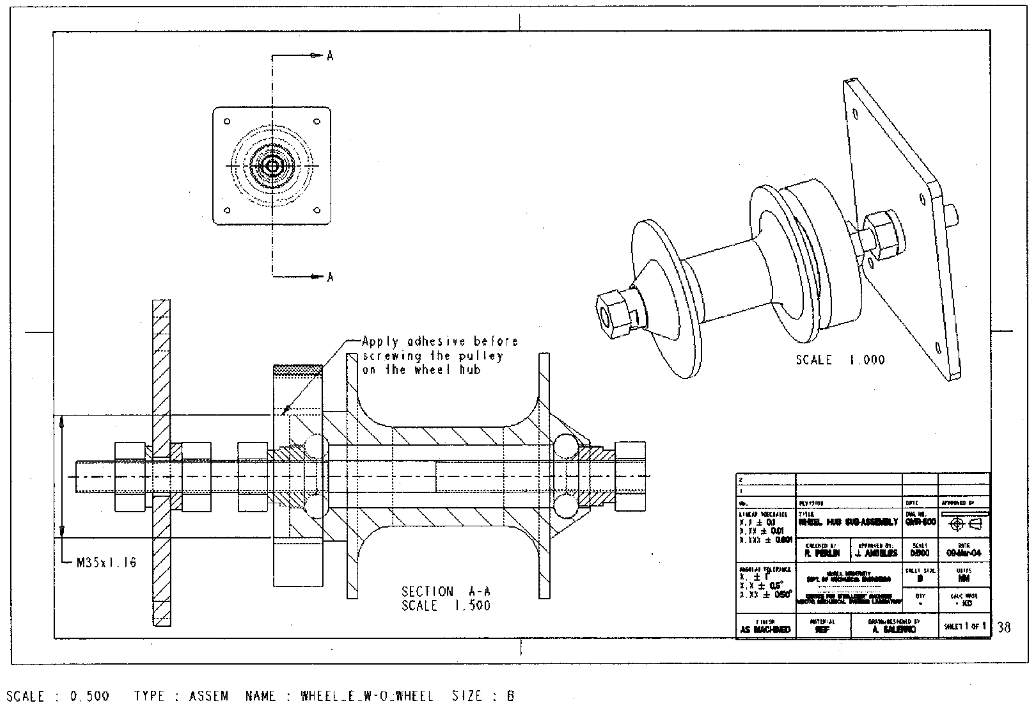

Figure B.7: Robot drive sytem—wheel side

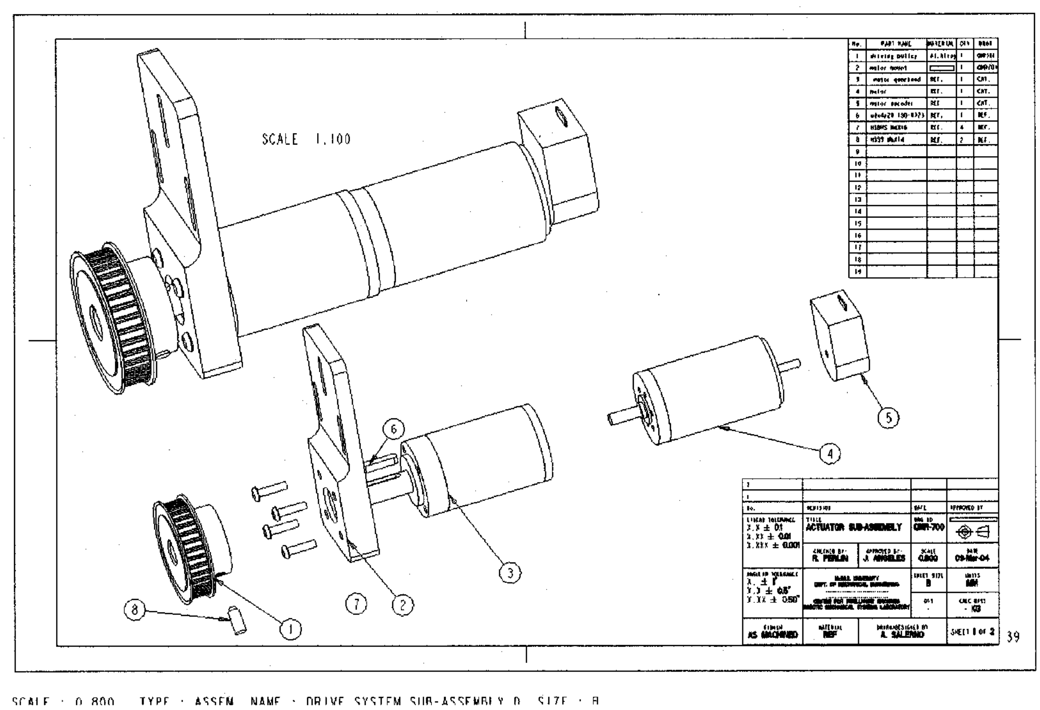

Figure B.8: Robot drive sytem—motor side

Appendix C

Custom-Made Harness Pin-Out

Pin #	Description
1	PA #1 analog ground (AGND)
2	PA #2 AGND
3	PA #1 positive reference (+REF)
4	PA #2 +REF
5	PA #1 negative reference ($-REF$)
6	PA #2 $-REF$
7-14	N/C

Table C.1: DA harness connector for the MPC550 DA converter—pin-out

Pin #	1	2	3
Description	PA #1 AGND	PA #1 +REF	PA #1 $-REF$

Table C.2: DA harness connector for the PA #1 signal harness—pin-out

Pin #	1	2	3
Description	PA #2 AGND	PA #2 +REF	PA #2 $-REF$

Table C.3: DA harness connector for the PA #2 signal harness—pin-out

Remarks:

- Heat-shrink tubing is installed on pins #1 of the DA harness connector for the MPC550 DA converter.

- The DIO harness connector for the 26-pin MPC550 DIO converter is a 30-pin connector, see Table C.4, whose female pins 27, 28, 29 and 30 should not mate with any of the male pins of the MPC550 DIO converter.

Pin #	1	2	from 3 to 26
Description	PA #1 enable line	PA #2 enable line	*N/C*

Table C.4: DIO harness connector for the MPC550 DIO converter—pin-out

Pin #	1	2
Description	PA #1 enable line	PA #2 enable line

Table C.5: DIO harness connector for PA signal harness—pin-out

- The inhibit lines changed into enable lines after being inverted.
- A black label, made of electrical tape, is installed on the white PVC cable cover of the DA harness connector for the PA #1.